

Department of  
Biotechnology and Bioscience

PhD program in Science  
Cycle XXIX  
Curriculum in Chemistry

# **INVESTIGATING THE FUNCTIONALIZATION OF COLLOIDAL NANOPARTICLES WITH SMALL MOLECULES OF BIOLOGICAL INTEREST**

Riva Benedetta

Registration number 787818

Supervisor: Prof. Davide Prosperi



**INVESTIGATING THE FUNCTIONALIZATION OF  
COLLOIDAL NANOPARTICLES WITH SMALL  
MOLECULES OF BIOLOGICAL INTEREST**

# TABLE OF CONTENTS

## EXTENDED ABSTRACT

## LIST OF PUBLICATIONS

## CHAPTER 1 – GENERAL INTRODUCTION

<b>1.1 - Nanotechnolgy and Biomedical Applications</b> .....	2
1.1.1 - Drug delivery.....	3
1.1.2 – Diagnosis.....	5
1.1.3 - Tissue engineering.....	8
1.1.4 – Theranostic.....	9
<b>1.2 - Nanoparticle functionalization for biomedical application</b> .....	10
1.2.1 - Surface modification for biocompatibility.....	11
1.2.2 - Bioconjugations for theranostic applications.....	12
<b>1.3 - Nanoparticle characterization</b> .....	15
1.3.1 – Size.....	15
1.3.2 - $\zeta$ -potential.....	15
1.3.3 – Morphology.....	17
<b>References</b> .....	18

## CHAPTER 2 – THERANOSTICS

<b>2.1 – Nonporous silica nanoparticles</b> .....	22
2.1.1 – Size, shape and surface properties.....	22
2.1.2 – Application in biomedical research.....	24
<b>2.2 – HER2 positive breast cancer: characteristics, diagnosis and therapy</b> .....	24
2.2.1 – Therapy.....	25
2.2.2 – Diagnosis.....	26
<b>2.3 – Design of a new theranostic agent for the targeted detection and therapy of HER2<sup>+</sup> breast cancer</b> .....	27

**(i) Development of radio-labelled SNPs for the targeted detection and treatment of Her2-positive breast cancer.**

<b>2.4 – Aim of the project</b> .....	29
<b>2.5 – Results and discussion</b> .....	29
2.5.1 – Synthesis and characterization of SNPs.....	29
2.5.2 – <i>In vitro</i> toxicity and cell viability.....	32
2.5.3 – <i>In vitro</i> binding efficiency and selectivity.....	33
2.5.4 – <i>Ex vivo</i> biodistribution and fluorescent imaging.....	36
<b>2.6 – Conclusion</b> .....	38
<b>2.7 – Experimental section</b> .....	40

**(ii) Development of doxorubicin-loaded nonporous silica nanoparticles**

<b>2.8 – Aim of the project</b> .....	48
<b>2.9 – Results and discussion</b> .....	50
2.9.1 – Synthesis of doxorubicin-loaded SNPs.....	50
2.9.2 – NP degradation and drug release kinetic studies.....	52
2.9.3 – <i>In vitro</i> studies of doxorubicin nanoformulation activity.....	56
2.9.4 – Cell uptake of doxorubicin nanoformulations.....	58
<b>2.10 – Conclusion</b> .....	59
<b>2.11 – Experimental section</b> .....	61

<b>References</b> .....	67
-------------------------	----

**CHAPTER 3 – ANALYTICAL TOOL**

<b>3.1 – Bioluminescence imaging</b> .....	72
3.1.1 – Bioluminescence imaging of tumors.....	73
<b>3.2 – Development of glutathione-sensitive apoferritin nanoparticles for the controlled delivery of luciferin</b> .....	74
<b>3.3 – Aim of the project</b> .....	75
<b>3.4 – Results and discussion</b> .....	75

3.4.1 – Synthesis of luciferin linker and conjugation to HF <sub>n</sub> nanoparticles .....	75
3.4.2 – Bioluminescence kinetic of Luc-linker@HF <sub>n</sub> <i>in vitro</i> .....	78
<b>3.5 – Conclusion</b> .....	82
<b>3.6 – Experimental section</b> .....	83
<b>References</b> .....	87
<b>APPENDED PAPERS</b> .....	90

# EXTENDED ABSTRACT

## Investigating the functionalization of colloidal nanoparticles with small molecules of biological interest

### INTRODUCTION:

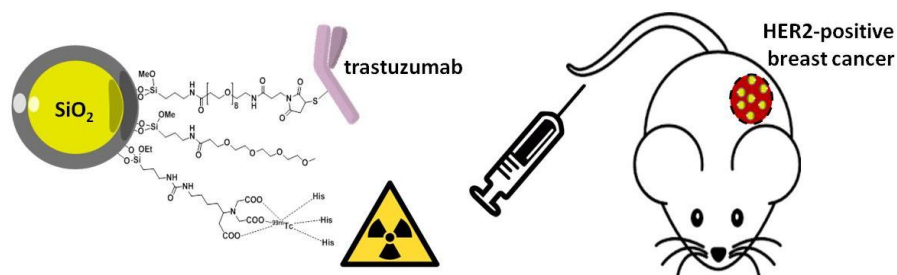
Nanoparticles (NPs) are generally defined as any particulate material for which at least one dimension lies in the range of 1–100 nm. NPs have several unique properties not found in their bulk counterparts, which include high surface-to-volume ratio, high surface energy, unique mechanical, thermal, electrical, magnetic, and optical behaviors, etc. The various chemical processes that guide the synthesis of materials in the nanometer scale can be defined as nanochemistry, which plays a critical role in tailoring the physical and chemical properties of NPs depending on the applicative destiny of the construct.<sup>1</sup> Nanomedicine is the application of NPs in medicine and seeks to address various medical challenges and shortcomings faced by conventional medicine, which include poor bioavailability, impaired target specificity, systemic and organ toxicity, etc.<sup>2</sup> Among all the advantages that NPs offer to this field, it is worth mentioning that a unique aspect of nanomedicine is multimodality, *i.e.* to perform several diagnostic and/or therapeutic functions in tandem. Nowadays, nanodiagnostics and nanoparticle-mediated drug delivery are being recognized as complementary technologies, with the popular term “theranostic” being used to describe their combination, that can bring about unprecedented advances in medicine.<sup>3</sup> Aim of this PhD thesis was to develop new nanoformulations for either diagnosis or therapy, focusing on the functionalization steps and the fine characterization of the nanoconstructs. In particular this was outlined in three different projects.

### RESULTS

(i) *Development of radiolabeled SNPs for the targeted detection of HER2-positive breast cancer.*

In this work we aimed at having targeted detection of a breast cancer (BC) subtype, characterized by a severe over-expression of HER2, often associated to highly aggressive and infiltrating tumors.<sup>4</sup> Thanks to their versatility and robust chemistry, monodisperse 50 nm

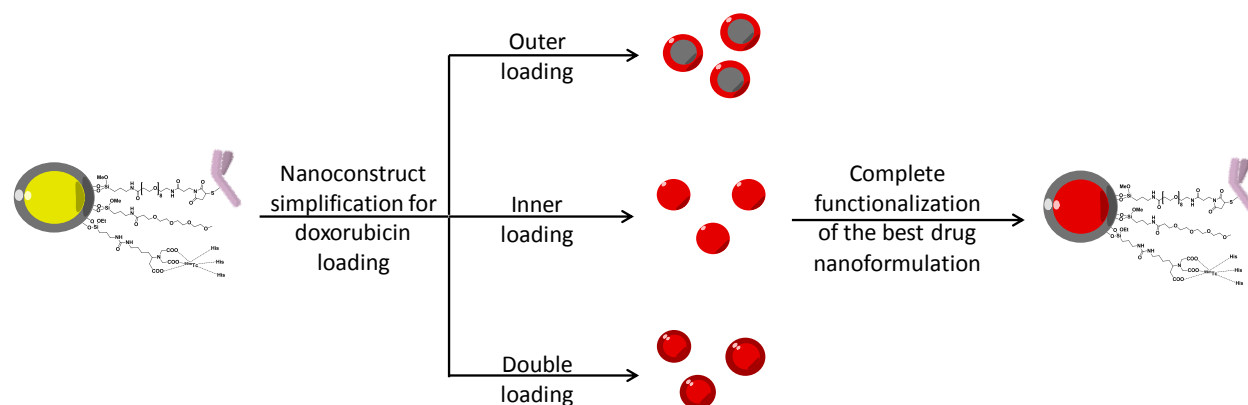
spherical silica nanoparticles (SNPs) were chosen to be the starting material to generate biocompatible multifunctional nanoconjugates.



Firstly, in order to have a fluorescent detectable carrier, the dense core of the SNPs, prepared by the Stöber method, was loaded with a fluorophore, which was protected by a denser silica shell, necessary to prevent the undesired cargo release and limit the dye bleaching that often leads to misleading optical artifacts.<sup>5</sup> After that, the functionalization steps were optimized with two goals in mind. First of all, we aimed to introduce a radionuclide,  $^{99m}\text{Tc}$ , useful for SPECT detection. In order to attach and retain the radionuclide, a silane derivative of the nitrilotriacetic acid chelating linker (IPTES-NTA complex) was synthesized and grafted on the silica. The NTA carboxylic moieties were then engaged in  $\text{Ni}^{2+}$  chelation before the radiolabeling steps. The second goal was to achieve an active targeting of the nanoconjugate toward  $\text{HER2}^+$  BC cells. In this case, the half chain of trastuzumab (Hc-TZ), a monoclonal antibody anti-HER2, was considered an ideal candidate, as it previously demonstrated to provide a longer period of accumulation of NPs in  $\text{HER2}^+$  breast tumors, compared to other molecular targeting agents, such as entire TZ.<sup>6</sup> These steps were accompanied by the introduction of different heterobifunctional PEGs, in order to have needed functional groups, together with biocompatibility and stealthness. The functionalization pathway was monitored both by size and  $\zeta$ -potential measurements and the impact of each chemical moiety on the SNP behaviour in cells was assessed in prelabeling *in vitro* experiments, comparing similar silica nanoconjugates differing from each other by the lack of one or more units. Targeting specificity of Hc-TZ-functionalized or Hc-TZ-free SNPs was studied in *in vitro*, *in vivo* and *ex vivo* experiments, both employing fluorescence and radionuclide techniques. Our results suggested that active targeting provided higher efficiency and selectivity in tumor detection compared to passive diffusion, confirming that our synthetic strategy provided stable nanoconjugates and did not affect their binding efficiency to HER2 expressing cells.

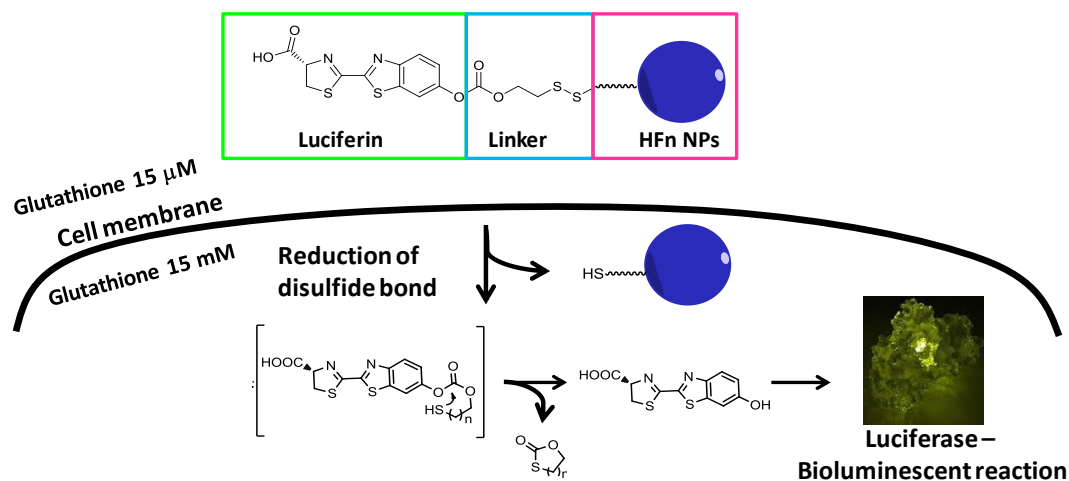


(ii) *Development of doxorubicin-loaded nonporous silica nanoparticles.*



Strongly correlated to the first project, in the second one we explored the possibility to use SNPs as drug delivery system, in order to develop a so-called theranostic agent for the simultaneous targeted detection and therapy of HER2<sup>+</sup> BC. Different silica nanoformulations containing the well-known anticancer drug doxorubicin were compared: OuterDox NPs, in which doxorubicin was covalently linked on the silica surface, InnerDox NPs, in which the chemotherapeutic was covalently immobilized in the core of the same particles and DoubleDox SNPs, in which the drug was grafted both internally and externally. OuterDox NPs were synthesized starting from naked Stöber SNPs. An IPTES-Dox complex was prepared and then condensed over SNPs in basic conditions (aqueous buffer, pH 9). In the case of InnerDox NPs, the IPTES-Dox complex was used as a co-condensating agent with TEOS, directly during the particle preparation. DoubleDox SNPs were prepared by covering InnerDox NPs with an external IPTES-Dox shell. The three doxorubicin nanoformulations were studied in terms of carrier degradation and payload release in physiological conditions: the first one was checked by a colorimetric quantification of soluble silicates, while the release was followed by fluorescence spectroscopy. In these experiments profound differences appeared: OuterDox NPs presented a long term degradation and sustained release up to 10 days; innerDox on the contrary showed a faster degradation and a consistent release in the earlier incubation time points (1-24 hours). DoubleDox, as expected, followed InnerDox trend at brief time points and OuterDox trend for longer incubation times. Other differences were found in cytotoxic experiments *in vitro*, which evidenced a pronounced cell viability reduction only for cells incubated with OuterDox SNPs. Taking into account all the data, OuterDox SNPs resulted the best candidates to be developed for the design of a theranostic agent, being colloiddally stable, reproducible and active on the tested tumor cell line.

(iii) *Development of glutathione-sensitive apoferritin nanoparticles for the controlled delivery of luciferin*



Although bioluminescence imaging has been successfully used in a variety of applications to obtain information regarding biological processes *in vivo*, the detection of photon emission is limited by the short half-life of luciferin (less than 30 minutes), its modest cell penetration and inhomogeneous diffusion into different tissues<sup>7</sup>. In this context, we developed a glutathione-sensitive NP for stimuli-responsive release of luciferin within cancer cells. The nanoconjugate bears luciferin by means of a disulfide containing linker (Luc-linker), which, in the presence of a reducing agent, undergoes an intramolecular cyclization reaction that results in the release of free luciferin. The correct luciferin release mechanism was checked in cell-free *in vitro* bioluminescence tests: an abundant photon production was detected when Luc-linker was preincubated with DTT (reducing environment) and then reacted with luciferase, while no light emission was seen without DTT pretreatment. Luc-linker was then attached to apoferritin (HFN) NP surface, exploiting the free thiol groups of cysteine residues, leading to Luc-linker@HFN NPs. Apoferritin (HFN) is a human protein composed of 24 subunits that self-assemble in a spherical NP and it was chosen as the pilot NP for its high biocompatibility and great cancer cell selectivity. After the conjugation, an HPLC method was developed for the quantification of conjugation efficiency and drug loading, requiring a preliminary separation of the linker from the hosting HFN NPs. The Luc-linker@HFN was then tested *in vitro* to initially elucidate the bioluminescent kinetics and compare the luminous signal to the one of nanoparticle-free luciferin.

## EXPERIMENTAL

Common methods exploited for the characterization of nanoparticles are dynamic light scattering (DLS),  $\zeta$ -potential and transmission electron microscopy (TEM). Nanoparticle concentration was obtained by drying a known volume of NP nanoparticles suspension in oven at 100 °C for several hours and weighing the resulting solid. Spectroscopic techniques, such as UV-visible and fluorescence spectroscopy, were exploited for FITC, doxorubicin, and Luciferin loading quantification and for molybdenum blue colorimetric assay. RP-HPLC, with a linear gradient from eluent A (0.1% TFA in water) to eluent B (0.1% TFA in acetonitrile) 100%, was used for D-luciferin linker purification and isolation during the synthetic pathway (semipreparative RP-HPLC) and for the quantification of D-luciferin loading on HF<sub>n</sub> nanoparticles (analytical RP-HPLC).

### *List of abbreviations*

DTT, 1,4-Dithiothreitol, FITC, fluorescein 5-isothiocyanate, HER2, human epidermal growth factor receptor 2, IPTES, (3-isocyanatopropyl)triethoxysilane, RP-HPLC, reverse phase high performance liquid chromatography, SPECT, single photon emission computed tomography, TEOS, tetraethyl orthosilicate, TFA, trifluoroacetic acid

### *References*

1. Chen, G., Roy, I., Yang, C. & Prasad, P. N. Nanochemistry and Nanomedicine for Nanoparticle-based Diagnostics and Therapy. *Chem. Rev.* **116**, 2826–2885 (2016).
2. Riehemann, K. *et al.* Nanomedicine--challenge and perspectives. *Angew. Chem. Int. Ed Engl.* **48**, 872–897 (2009).
3. Ma, X., Zhao, Y. & Liang, X.-J. Theranostic nanoparticles engineered for clinic and pharmaceuticals. *Acc. Chem. Res.* **44**, 1114–1122 (2011).
4. Slamon, D. J. *et al.* Human breast cancer: correlation of relapse and survival with amplification of the HER-2/neu oncogene. *Science* **235**, 177–182 (1987).
5. Mahon, E., Hristov, D. R. & Dawson, K. A. Stabilising fluorescent silica nanoparticles against dissolution effects for biological studies. *Chem. Commun.* **48**, 7970–7972 (2012).
6. Fiandra, L. *et al.* Assessing the In Vivo Targeting Efficiency of Multifunctional Nanoconstructs Bearing Antibody-Derived Ligands. *ACS Nano* **7**, 6092–6102 (2013).
7. Harwood, K. R., Mofford, D. M., Reddy, G. R. & Miller, S. C. Identification of Mutant Firefly Luciferases that Efficiently Utilize Aminoluciferins. *Chem. Biol.* **18**, 1649–1657 (2011).

# LIST OF PUBLICATIONS

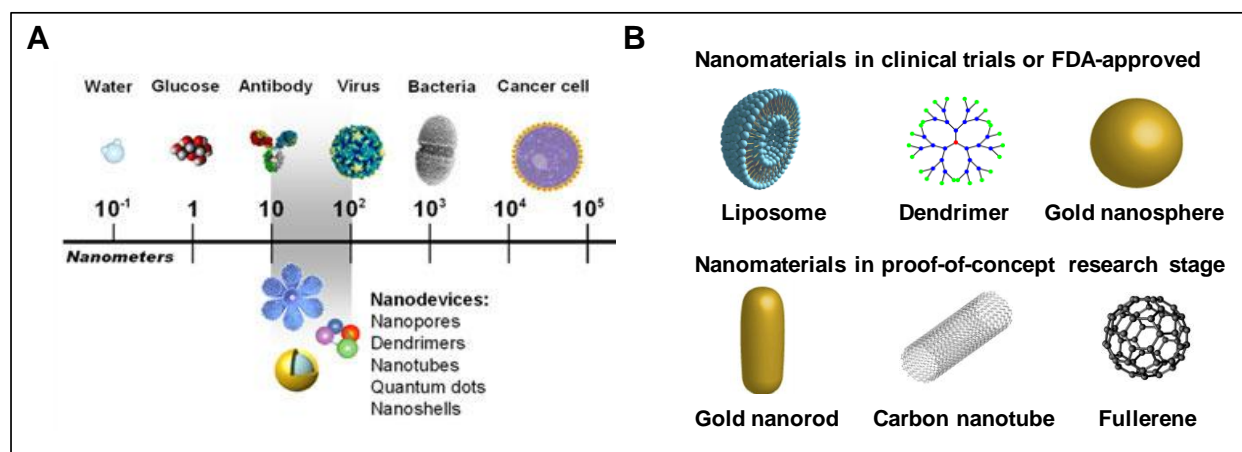
- **B. Riva**, P. Rainone S. Belloli, F. Sudati, M. Ripamonti, P. Verderio, M. Colombo, M. C. Gilardi, R. M. Moresco, D. Prospero, *Development of <sup>99m</sup>Tc-Radiolabeled Nanosilica for Targeted Detection of HER2-Positive Breast Cancer*, ***International Journal of Nanomedicine* (2017) in revision**
  
- G. Fumagalli, M. Christodoulou, **B. Riva**, I. Revuelta, C. Maurucci, V. Collico, D. Prospero, S. Riva, D. Perdicchia, I. Bassanini, A. García-Argáez, L. Dalla Via and D. Passarella, *Self-assembled 4-(1,2-diphenylbut-1-en-1-yl)aniline based Nanoparticles: Podophyllotoxin and Aloin as building blocks*, ***Organic & Biomolecular Chemistry* (2017)**, DOI: 10.1039/C6OB02591A
  
- C. Finetti, L. Sola, M. Pezzullo, D. Prospero, M. Colombo, **B. Riva**, S. Avvakumova, C. Morasso, S. Picciolini and M. Chiari, *Click chemistry immobilization of antibodies on polymer coated gold nanoparticles*, ***Langmuir* (2016)**, 32, 7435-7441
  
- **B. Riva**, R. Ferreira, L. Musso, R. Artali, L. Scaglioni, S. Mazzini, *Molecular recognition in naphthoquinone derivatives — G-quadruplex complexes by NMR*, ***Biochimica et Biophysica Acta* (2015)**, 1850, 673-680
  
- M. S. Christodoulou, A. Sacchetti, V. Ronchetti, S. Caufin, A. Silvani, G. Lesma, G. Fontana, F. Minicone, **B. Riva**, M. Ventura, M. Lahtela-Kakkonen, E. Jarho, V. Zuco, F. Zunino, N. Martinet, F. Dapiaggi, S. Pieraccini, M. Sironi, L. Dalla Via, O. M. Gia, D. Passarella, *Quinazolinecarboline Alkaloid Evodiamine as Scaffold for Targeting Topoisomerase and Sirtuins*, ***Bioorg.Med.Chem* (2013)**, 21, 6920-6928

**CHAPTER 1**

**GENERAL INTRODUCTION**

## 1.1 - Nanotechnology and Biomedical Applications

Nanotechnology refers to the specific design, production and manipulation of matter in the nanometric scale, ranging from 1 to 1000 nm. Nanomaterials possess several unique properties not found in the bulk counterpart, such as high surface-to-volume ratio, tailorable physical chemical properties, high surface energy, peculiar mechanical, thermal, electrical, optical behaviors etc. All these peculiarities make nanomaterials applicable in a wide range of fields, including electronics, renewable energies, textiles, food industry, healthcare and medicine [1]. It is worth noting that nanoscale devices are one hundred to ten thousand times smaller than human cells and similar in size to large biomolecules such as enzymes and receptors (Figure 1.1, A). Because of this characteristic, nanomaterials show great potential for biomedical applications; nanobiotechnology is the fusion of biotechnology and nanotechnology, combining the efficacy of biological materials and the rules and tools of basic sciences like physics, chemistry and genetics to fabricate minute synthetic structures [2]. Within this field nanomedicine is defined as the application of NPs in medicine and seeks to address various medical challenges and shortcomings faced by conventional medicine, which include poor bioavailability, impaired target specificity, systemic and organ toxicity, etc. In the last few decades many new products have been developed in the nanomedicine field, some of which are currently undergoing clinical trials or have been approved by the Food and Drug Administration (FDA) for use in humans, others are in the proof-of-concept stage in research laboratories (Figure 1.1, B) [3].



**Figure 1.1** A) Comparable dimension of nanodevices and biological elements, B) Nanomaterials commonly used in biomedicine [4]

Size is not the only characteristic that renders nanoparticles optimal candidates in biomedical applications, rather nanoparticulate carriers show several key advantages over molecular agents conventionally used in medicine. First, they enable stable aqueous dispersions of poorly water soluble active principal, a necessary prerequisite for administration in living organisms. Nevertheless they can easily host hydrophobic entities as well, thus representing almost universal carriers, whose composition, size, shape, and surface properties can be tailored to protect the payload from endogeneous defense mechanisms in the body. Moreover it's possible to control of their size, shape, and surface properties to target them not only to specific cells, organs or tissues, but even to subcellular components of interest [5]. Another major benefit is the possibility to design nanosystems for the controlled and sustained release of active entities, either by building a totally stimuli-responsive nanocarrier or introducing chemical moieties able to play their part in response to specific biological signals [6]. Among all this wonderful possibilities, the most important and unique aspect of nanomedicine is multimodality, i.e. the capacity to perform several diagnostic and/or therapeutic functions in tandem, thus paving the way to the construction of innovative theranostic agents [7].

The foremost biomedical applications of nanotechnology can be summarized in three main fields, namely drug delivery, diagnostic and tissue engineering. In the following paragraphs a brief overview will be made for each of these applications, trying to focus on nanotechnology precious contribution. Besides, a short description of theranostic will be made, as it will be helpful to understand the aim of this PhD thesis.

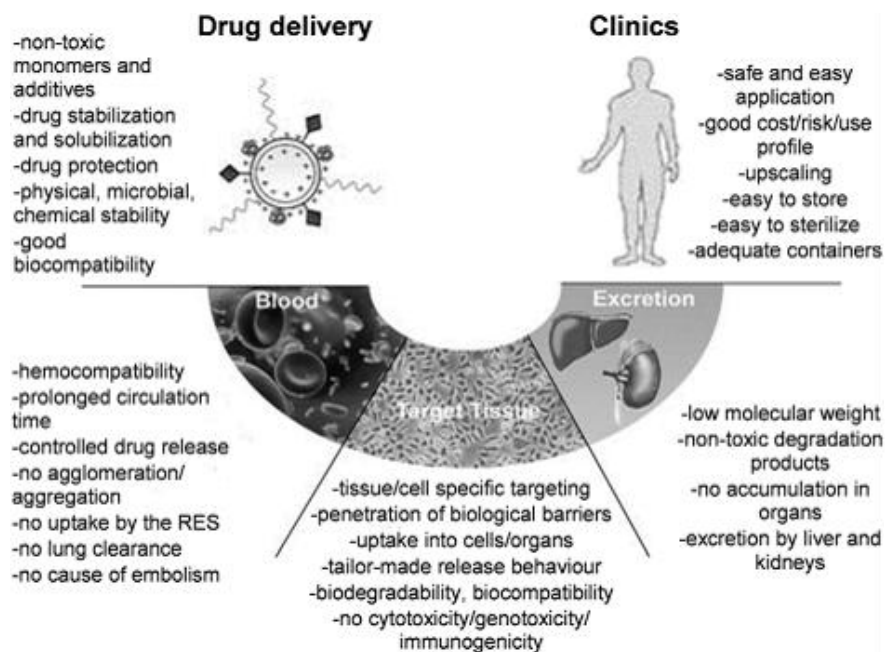
### 1.1.1 – Drug delivery

Drug delivery is defined as the strategy to transport therapeutics in the body as needed to safely and efficiently achieve their desired therapeutic effects; drug delivery systems (DDs) can be described as formulations or devices that enable the introduction of an active substance in the body and improve its efficacy and safety by controlling the rate, time and place of release process [8]. These technologies appear fundamental to overcome the limitations of active principles ad drugs themselves, such as water insolubility, poor bioavailability, insufficient target specificity, and significant side effects. Due to their unique nanoscale properties and synthetic versatility, nanomaterials provide intriguing benefits and new opportunities in realizing innovative DDs [9]. Major advantages of nano drug delivery systems (nano DDs) are:

- *Dispersability and protection*: nanoDDs permit stable aqueous dispersion of either hydrophilic or hydrophobic molecules, thus improving their bioavailability and reducing administered dosage; besides, nanoDDs can act as drug protector against enzymatic degradation, recognition by immune system and metabolism by reticuloendothelial system.
- *Targeted delivery*: nanoDDs can be modified to specifically transport the drug to the site of action, hence increasing its local concentration. This can be done by targeting particular tissues (first order targeting), cells (second order targeting) or intracellular organelles (third type targeting) and exploiting passive or active targeting mechanisms [10]. Passive targeting relies on the dimension of nanosystems and the consequent possibility to accumulate in tumor tissues because of the enhanced permeability and retention (EPR) effect. This mode of targeting is restricted to cancer and inflammatory sites, and it can reach a precision of second order targeting at most. On the contrary, active targeting can achieve the precision of third order targeting in all diseases as it relies on the introduction on nanoDDs surface of specific recognition molecules specific for receptors expressed on pathological tissue or cells.
- *Controlled release*: nanoDDs may exert control over the delivery of their payload and permit sustained, stimuli-responsive or externally activated release. Sustained release signifies time-dependent release of entrapped drugs from their nanocarriers into the surroundings. In particular, in the case of biodegradable DDs, the release increases over time with the degradation of the matrix; in the case of nonbiodegradable DDs, the time-dependent release depends on the drug diffusion rate outside from channels or pores. Stimuli-responsive DDs are constructed to release a drug in correspondence of a triggering signal, ideally specific for the pathological area, such as a change in pH and temperature, or the presence of a specific biological agent. Similarly, the release process can be activated by external sources able to destabilize the matrix of the carrier, such as light, magnetic or electric field, ultrasound, etc.
- *Multimodality*: strongly connected to nanomaterial properties and technology advancements, multimodal nanoDDs can be designed, such as devices that incorporate drug cocktail for complex diseases where a single drug is largely ineffective (combination therapy), systems that combine diagnostic and therapeutic activities (theranostic) or traceable DDs for image guided therapies.



Despite all these promising aspects, the realization of nanoDDs, including the design, synthesis and complete characterization, appears anything but easy, especially if we consider the poor clinical translation that has occurred up to date. Essential components and critical points in drug delivery development are outlined in Figure 1.2.

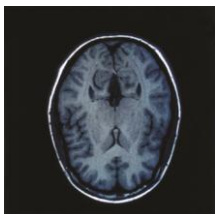

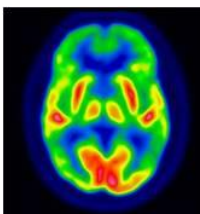
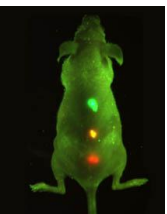
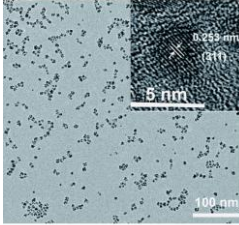
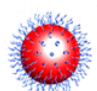
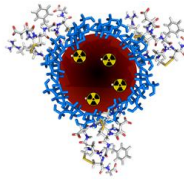
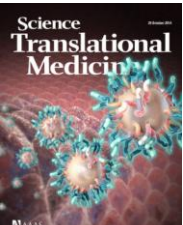


**Figure 1.2** Essential components in the development of nanoDDs, including essential properties for clinical translation [9].

### 1.1.2 – Diagnosis

Nanotechnology is becoming a leading science also for diagnostic methodologies, with particular relevance in diagnostic imaging techniques including magnetic resonance imaging (MRI), computed tomography (CT) and positron emission tomography (PET). Normally, these techniques involve the use of contrast agents, *id est* materials that can interact with the incident radiation to produce visible changes in the sensitivity of the detection and, consequently, in the quality of the resulting images. For their unique size-dependent properties, many nanometric contrast agents have been developed and not only demonstrated optimal sensitivity, biocompatibility and biodistribution profile in the current diagnostic methodologies, but they also open-up the possibility to use new imaging technologies, such as fluorescence imaging, and a combination of techniques with a unique contrast agent. Hereinafter a brief description

of nano-contrast agents will be given, depending on the implied imaging techniques (Figure 1.3) [11].

	MRI	CT	PET	Fluorescence imaging
Examples of resulting images				
Examples of exploited nanoparticles		 Bi NPs	 <sup>68</sup> Ga-C-IONP-RGD	
	<b>Superparamagnetic iron oxide nanoparticles</b>	<b>Bismuth nanoparticles</b>	<b><sup>68</sup>Ga-iron oxide nanotracer</b>	<b>Cornell dots</b>

**Figure 1.3** Graphical overview of imaging techniques discussed in the text. Examples of the resulting images are presented together with an example of the nanoparticles exploited for each technique. Corresponding references could be found in the main text.

- *Magnetic resonance imaging*: MRI works by applying external magnetic field to interact with the abundant protons present in soft tissues - such as cartilage, muscles and tumors – aligning their magnetic moment in the direction of the field. Meanwhile a radiofrequency pulse is sent: when the radiofrequency is on the protons change the direction of their magnetic moment direction depending on the specific type of tissue they reside in, when the pulse is switched off the proton magnetic moments realign with the external magnetic field with a process called relaxation. Through computer-aided reconstruction of the detected tissue-dependent relaxation signals, composite images are constructed with contrast differences between tissues. A greater difference in relaxation time between two tissues will give a greater contrast in the MRI image. In this case, contrast agents enhance tissues differences by altering the relaxation times of water protons around them. Within this field, nanomaterials are exploited to enhance contrast power either by transporting contrast agent functionalities and concentrating them in the

interested area – *e.g.* gadolinium(III)-functionalized nanoparticles [12] -, or by acting themselves as contrast agents, owing to their unique magnetic properties – *e.g.* superparamagnetic iron oxide nanoparticles [13].

- *Computed tomography*: CT is based on X-ray cross-sectional images and it is commonly used for diagnosis in pelvis, head, abdomen and chest. The sensitivity of CT tissue recognition depends on the difference in X-ray attenuation between neighboring tissues. Indeed, contrast agents for CT should improve visualization of a target tissue by increasing the X-ray attenuation difference between the target tissue and the surrounding tissue and fluids. Various nanomaterial-based contrast agent have been developed to overcome the common problems of traditional contrast agents, including nonspecific biodistribution, short circulation half-lives, occasional renal toxicity and poor contrast in large patients [14,15]. For example gold nanoparticles are excellent CT contrast agents due to their increased X-ray absorption and prolonged blood circulation time compared to traditional iodine-based contrast agents [16].
- *Positron emission tomography*: PET is characterized by high tissue penetration, while poor structural resolution, so that rather than providing structural information, it is able to monitor functional activities in the body, such as blood flow, glucose metabolism and oxygen uptake. In PET analysis a chemical moiety labeled with a short-lived positron-emitting radionuclide - including  $^{11}\text{C}$ ,  $^{13}\text{N}$ ,  $^{15}\text{O}$ ,  $^{18}\text{F}$ , to name a few - is injected in the body. As the radionuclide decays, positrons are annihilated by surrounding electrons, thus emitting  $\gamma$ -rays that can be detected and computationally reconstructed to produce images of the scanned organ. Commonly, PET is used in tandem with other imaging modalities, giving rise to hybrid imaging techniques, such as PET-CT or PET-MRI, which are able to provide both anatomical and functional information about an organ or tissue. For their multimodal potential, nanoparticles are ideal platforms to construct imaging tracers for above-mentioned hybrid techniques. For example a  $^{68}\text{Ga}$ -iron oxide nanotracer for dual PET-MRI imaging was recently reported in the literature, combining the magnetic properties of iron oxide nanoparticles for positive contrast in MRI with the positron emission capability of  $^{68}\text{Ga}$  [17].
- *Fluorescence imaging*: fluorescence-based techniques, such as confocal microscopy and flow cytometry, are commonly used for *in vitro* and *in vivo* analysis of various processes. For these practices, free organic fluorophores together with fluorescent-labeled proteins and macromolecules are largely employed, but still there are many

limitations: poor skin/tissue penetration, wide emission and absorption bands, poor signal strength, short imaging times *in vivo*, and high susceptibility to photobleaching. New advances in fluorescent nanomaterials are beginning to overcome many of the problems associated with traditional fluorophores and are starting to open up the possibility of utilizing fluorescence imaging techniques in clinical diagnosis. The most widely studied nanoparticles in this area are quantum dots, *id est* inorganic fluorescent semiconductor nanoparticles with high quantum yields, high molar extinction coefficients, strong resistance to photobleaching and chemical degradation, continuous absorption spectra spanning UV to near-infrared, long fluorescence lifetimes, and narrow emission spectra [18]. Interestingly, the so called Cornell dots, designed to light-up cancer cells, have been recently tested in the first human clinical trials and proved to be non-toxic [19].

### 1.1.3 – Tissue engineering

Tissue engineering is defined as an interdisciplinary field which applies the principles of engineering and the life sciences toward the development of biological substitutes that restore, maintain, or improve tissue functions [20]. The scope of this discipline is the combination of cells with biomaterials or biologically active molecules to generate new materials that can reproduce, repair or replace native tissues as realistic as possible. Typically cells are cultured until a specific degree of proliferation, when they are seeded on proper scaffolds that have been engineered to promote cellular interactions and new tissue generation, which will be then implanted in the patient. Ideally, stem cells represent ideal candidates owing to their ability to generate all types of tissues and their unlimited self-renewal capacity. In addition, the functionalization of the scaffolds with growth factors, drugs or genes, could greatly enhance the success of this strategy. Nevertheless, major drawbacks in this procedure are stem cell isolation from the patient and their proliferation, the inability of cells to properly vascularise, the culturing process in a bioreactor and the time delay before the engineered hybrid construct is implanted back into the patient *etc.* [21]. Concerning this issue, nanotechnology offers the possibility to improve the interactions between material surfaces and biological entities by means of the production of nanometric surfaces, structures and materials that can mimic the natural environment of cells, hence promoting fundamental functions, such as cell adhesion, cell mobility and cell differentiation [22]. Numerous *in vitro*

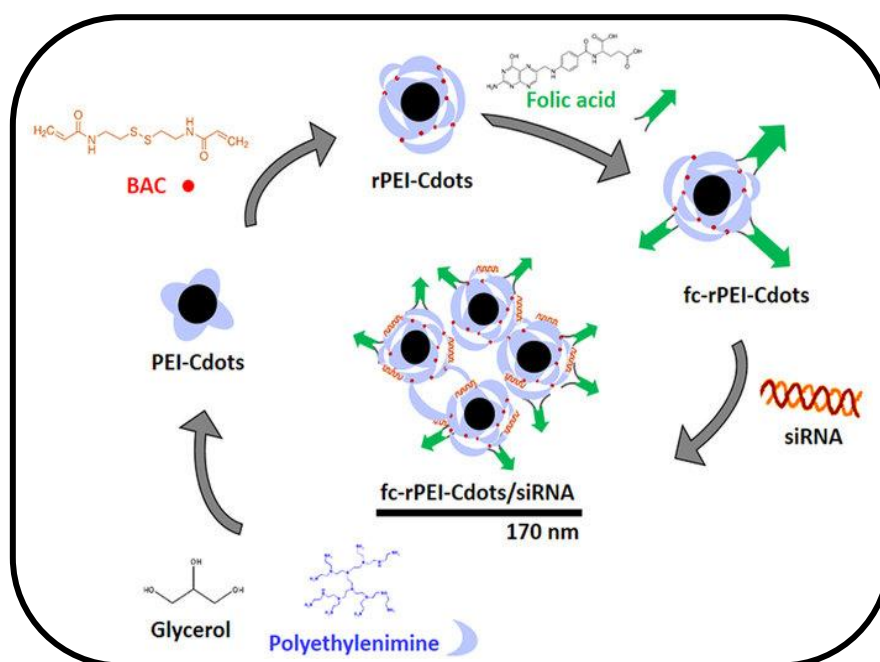
and *in vivo* studies, using nanostructured materials, confirmed the potential of nanostructures in regenerating different tissues (such as bone, cartilage, bladder, nerves and vessels) by enhancing the biological performance of proliferating cells. Examples of the most recent studies are reported in Table 1.1.

**Table 1.1** A summary of nanostructured biomaterials with potential applications in engineering different tissues.

<b>Application</b>	<b>Material</b>	<b>Results</b>	<b>Reference</b>
Bone	TiO <sub>2</sub> nanotube layer	Enhanced osteogenic potential of bone marrow stromal cells and reduced immune response	[23]
Nerves	Silicon nanowires	Differentiation of human mesenchymal stem cells into neuronal lineage without inducing agents	[24]
Teeth	Zinc-bioactive glass nanoparticles	Improvement of dental cell regeneration and angiogenesis	[25]
Tendon	Polymeric electrospun nanoscaffolds	Construction of tendon mimetic nanofibrous structure with appropriate mechanical performance	[26]

#### 1.1.4 – Theranostic

The term “theranostics” was coined to define the combination of diagnostic and therapeutic capabilities into a single agent, aiming at the development of more specific, individualized therapies for various diseases. Cutting-edge theranostic agents are designed to be single integrated system, capable of sensing the endogenous bio-markers of a host organism and accordingly exerting therapeutic functions with minimal delay [27]. Thanks to the notable multimodality of nanoparticles, theranostic appears the obvious culmination of bionanotechnology development. Typically, nanotheranostic agents are composed of four main moieties: a nanoparticle, a therapeutic molecule, a diagnostic imaging tool and a targeting ligand. For example, a recent research by Tzu-Wei Wang and coworkers presented a multifunctional theranostic nanoparticle for lung cancer treatment, built up as follow (Figure 1.4): the core of the nanoconjugate was made up of carbon quantum dots, that are nano-scaled carbon material with prolonged photoluminescence properties suitable for imaging detection; after the addition of a polyethylenimine shell, the carbon-dot core was functionalized by folic acid to actively target cancer cells and by siRNA entities in order to treat lung cancer by gene silencing approaches [28].



**Figure 1.4** Example of nanoparticle-based theranostic agent presented by Tzu-Wei Wang and co. [28].

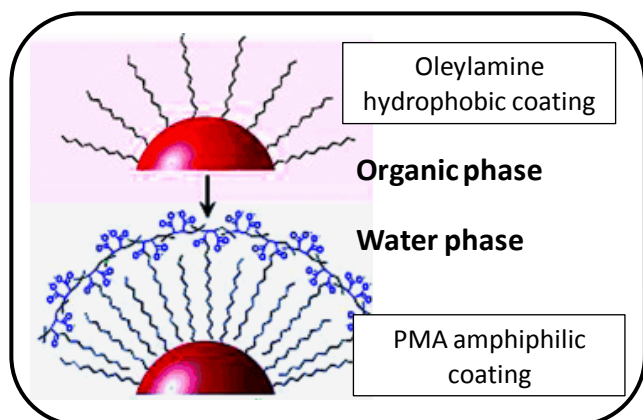
The as-prepared nanoconjugates proved to be optimal for bioimaging diagnostic, with a stronger photoluminescence emission when internalized in target cancer cells, and also demonstrated promising gene silencing efficiency.

Many other examples can be found in the literature, exploiting a variety of nanoparticles, drugs and imaging techniques. All of these systems can lead to an enhancement of treatment options, leading to truly personalized medicine, but still none of the developed nanotheranostic agents were successfully translated into clinical practices.

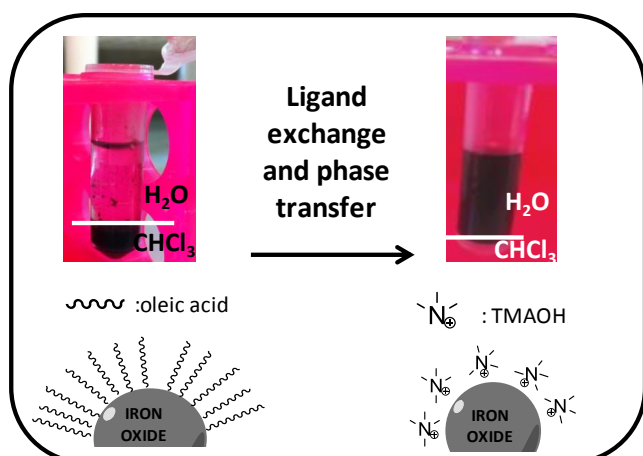
## 1.2 – Nanoparticle functionalization for biomedical applications

As we understood in previous sections, surface chemistry of NPs plays a pivotal role in defining the possibility of biomedical employment. Nanoparticle surface manipulation has a plethora of functions ranging from physiological stability, biocompatibility and biodegradability, to active targeting, therapeutic activity and diagnostic properties. Synthetically we can divide nanoparticle functionalizations into two main categories: the modifications addressed to nanoparticle biocompatibility and the ones fundamental to guarantee the desired activity [29].

### 1.2.1 – Surface modification for biocompatibility



**Figure 1.6** phase transfer for magnetite NPs using a micellar encapsulation strategy. PMA is the polymer resulting from the condensation between poly(isobutylene-*alt*-maleic anhydride) and dodecylamine



**Figure 1.5** Phase transfer for magnetite NPs using a ligand-exchange strategy.

In order to assure the required biocompatibility, nanoparticles need to expose appropriate moieties to the biological environment in which they will be sent. In some cases nanoparticles result biocompatible and stable in aqueous media as synthesized (e.g. chitosan and silica NPs), while in most of cases biocompatible functionalities have to be introduced in a second stage, meaning that the nanomaterial must be chemically modifiable. Even in this case, requested functional moieties can be present on the as-prepared nanoparticle core itself (e.g. polyethylenimine or PLGA NPs), or they need to be added on the surface after nanoparticle preparation (e.g. most of inorganic NPs). The first case is typical for polymeric nanoparticles that usually contain many reactive groups for facile modification; conversely the case of inorganic-based nanoparticles results more complicated. In fact the synthesis of inorganic NPs commonly requires organic solvents and, consequently, a surface reactive molecule that

will anchor the particle at one side, while exposing an appropriate functionality on the other end. For example, magnetite nanoparticles can be prepared by solvothermal decomposition in organic solvents, in which they result stable thanks to oleylamine hydrophobic chains coating their surface [30]. In order to be used in physiological environment, a transfer phase to water is mandatory. Amphiphilic polymers, such as PMA obtained from the condensation of poly(isobutylene-*alt*-maleic anhydride) and dodecylamine, can be exploited for this purpose: the hydrophobic tails will intercalate between the lipophilic stabilizer on nanoparticle surface, while the hydrophilic heads will protrude toward the external aqueous environment, usually

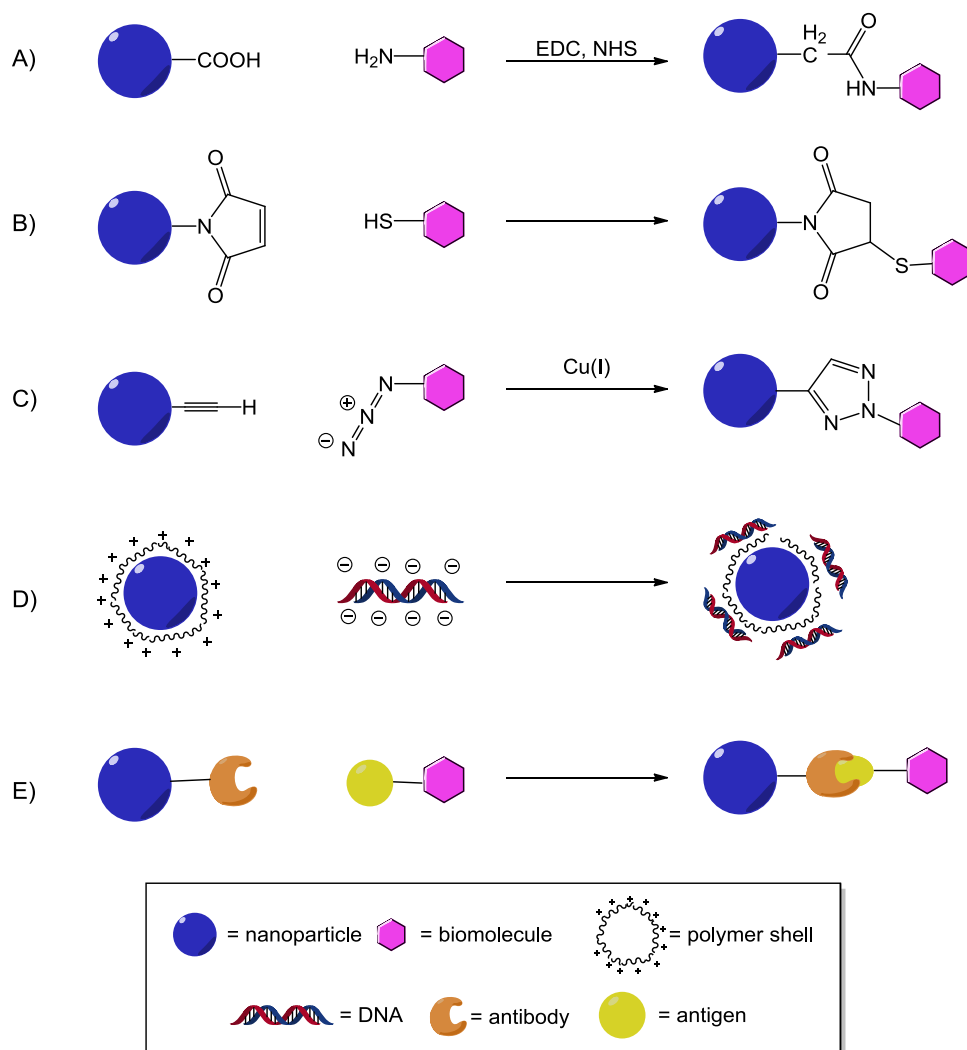
exposing further reactive groups for bioconjugation (Figure 1.5) [31]. In addition to this encapsulation within polymeric micellar network, other strategies can be used to transfer surfactant-coated inorganic NPs to an aqueous medium. The ligand-exchange methods imply the removal of the organic stabilizers from nanoparticle surface and then the replacement with an aqueous compatible ligand for their stable aqueous suspension. In figure 1.6 an example for the above-mentioned magnetite NPs is given: PMA-coated NPs are vigorously stirred overnight in presence of an excess of tetramethylammonium hydroxide (TMAOH), resulting in the replacement of PMA by TMAOH and thus in the nanoparticle phase transfer from chloroform to water [32]. Another well established method to make nanoparticles water-dispersible and biocompatible is the surface silanization, which means to introduce an hydrophilic silica shell around the hydrophobic core, moreover offering abundant functional groups (e.g.,  $-\text{COOH}$ ,  $-\text{NH}_2$ ,  $-\text{SH}$ ) for further conjugation with biological molecules [33]. Many protocols have been developed in this direction, ranging from Stöber synthesis and microemulsion methods, to gas phase methods [34]. Finally a layer-by-layer assembly can be built on the surface of NPs, by means of sequential adsorption of oppositely charged ions. The advantage of this method is that it permits the preparation of coated colloids of different shapes and sizes, with uniform layers of diverse composition and thickness. This also involve the possibility of manipulating the sign and the magnitude of the surface charge or incorporating functional groups [35].

### 1.2.2 – Bioconjugations for theranostic applications

Conjugation of NPs with various functional biomolecules is generally required for their biomedical applications, being that therapeutic, diagnostic or theranostic. A plethora of molecules could be attached on NP surface, among which the most widely utilized include: peptides, proteins, and antibodies; enzymes and ribozymes, oligonucleotides and aptamers; carbohydrates, lipids, drugs, or other biologically active small molecules; reporter molecules or contrast agents, including MRI labels, radiolabels, and fluorescent dyes. The surface reactivity of nanocarriers, which could be intrinsic or resulting from functional groups added post-synthesis, is used in various covalent and non covalent bioconjugation approaches. It is important to note that the effectiveness of the resulting nanoconjugates, will depend not only on the success of the conjugation, but also on the nanoparticle/biomolecule ratio, the spatial



orientation, the activity and density of biomolecules on the nanoparticle surface, and the nonspecific interactions with undesired biological species [36].



**Figure 1.7** Examples of bioconjugation strategies, including covalent linkages ( A) Peptide bond, B) Michael addition, C) click chemistry) and non covalent interactions ( D) electrostatic interactions, E) antibody-antigen recognition).

Among the bioconjugation strategies, covalent linkages mainly rely on traditional protein labeling chemistry, exploiting the formation of new chemical bonds between reactive functional groups on the molecule of interest and the nanoparticle. The most exploited strategies include:

- *Peptide bond*: carbodiimide-mediated reaction between amino and carboxyl groups to form amide bond (Figure 1.7, A). Typically the carboxylic acid is first activated by coupling agents, such as the well-known 1-ethyl-3-(3-(dimethylamino)propyl)

carbodiimide hydrochloride (EDC) and N-hydroxysulfosuccinimide sodium salt (sulfo-NHS), to produce an active O-acylisourea intermediate, which can then react with the  $-NH_2$  group contained in the biomolecule of interest [37].

- *Michael addition*: chemical reaction between a thiol and a maleimide group, which can produce a stable thio-ether bond at physiological pH (Figure 1.7, B). This is particularly useful for bioconjugation of proteins containing cysteine groups, either naturally present in the polypeptide sequence or intentionally introduced at specific positions by site-directed mutagenesis [38].
- *Copper-catalyzed azide-alkyne click chemistry*: 1,3-dipolar cycloaddition reaction between an azide and a terminal or internal alkyne group to give a 1,2,3-triazole under the catalyzing influence of copper(I) (Figure 1.7, C). This reaction has been extensively used for nanoparticle functionalization because it is fast, produces high yields, does not require temperature control, and does not produce any byproducts [39].
- *Chemisorptions*: this mode of binding usually involves sulfur-containing biomolecules and metal surfaces, as organosulfur groups strongly coordinate to various metals, such as Ag, Cu, Pt, Hg, Fe, or Au [40].

Many noncovalent strategies may also be exploited, such as electrostatic interactions - between positively charged biomolecules and negatively charged nanoparticles or vice versa (e.g DNA and polycationic polymers coating NPs, Figure 1.7, D) -, hydrophobic interactions (e.g. proteins and metallic NPs) and antibody-antigen molecular recognition. The latter is based on molecular recognition between a ligand and a receptor, each of which will be either attached to the NP surface or to the biomolecule of interest (Figure 1.7, E). The most common antibody-antigen system for nanoconjugate synthesis is the avidin-biotin system. The globular protein avidin is made up by four identical subunits, yielding four binding pockets that specifically recognize and bind to biotin with a dissociation constant of the order of  $10^{15}$  M. The strong bond and specificity of the biotin-avidin system has led to a commercial diffusion of various biomolecules readily modified with biotin or avidin for a large number of applications in bionanotechnology.

## 1.3 – Nanoparticle Characterization

In order to improve the translation of nanomedical device to clinics, it is imperative to employ adequate methodologies to characterize them, correlate their effects and biological consequences, and predict the therapeutic outcomes in clinical subjects. A rational characterization strategy for bioconstructed NPs contains three elements: physicochemical characterization, *in vitro* assays and *in vivo* studies. In order to facilitate the comprehension of this PhD thesis, the paragraph will be focused on the techniques commonly used to determine the physicochemical properties of NPs.

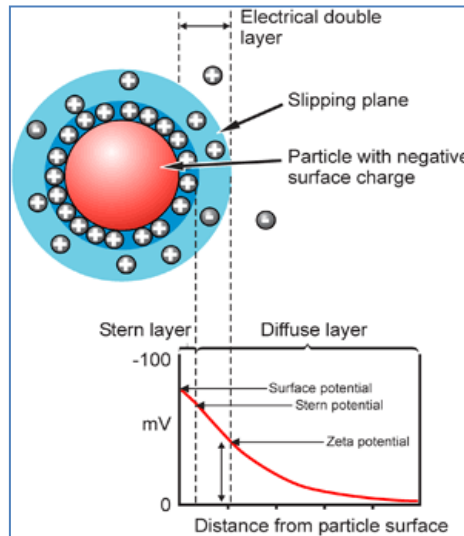
### 1.3.1 - Size

Dynamic light scattering (DLS) is routinely used in nanotechnological research to obtain the size and size distribution of nanomaterials. In DLS, NPs in solution are illuminated by a monochromatic laser and scatter the light with different intensities depending on their Brownian motion, which is defined as the particle movement due to the random collision with the molecules of the surrounding liquid. Analysis of these intensity fluctuations yields the velocity of the Brownian motion and hence the particle size using the Stokes-Einstein relationship. The diameter measured by DLS is defined as the size of the hypothetical hard sphere that diffuse at the same rate as the particle being analyzed [41]. As in practice particles in solution are non-spherical, dynamic, and solvated, the size calculated from the diffusional properties of the particle will be an hydrodynamic diameter ( $H_d$ ), *id est* the diameter of the particle surrounded by an hydration layer. Generally, nanoparticle samples contain a distribution of sizes which is also determined by DLS analysis and indicated by the dimensionless polydispersity index (PDI). In our studies, NP suspensions showing a PDI < 0.200 were considered to have a narrow size distribution, while PDI values > 0.200 indicated polydispersed preparations.

### 1.3.2 – $\zeta$ -potential

Surface charge, expressed as zeta potential, critically influences the interaction of NPs with the environment [42]. In an ionic solution, NPs with a net charge are surrounded by two liquid layers, namely electrical double layer: one full of oppositely charged ions strongly bound to their surface (Stern layer), and the other made of outer weakly associated ions. As the particle moves, a boundary, known as “slipping plane”, appears in the diffuse layer between

ions that moves with the particle and ions that remains in the bulk dispersant. The electrostatic potential at the slipping plane is the  $\zeta$ -potential and is related to the surface charge of the particle (Figure 1.8).



**Figure 1.8** schematic representation of  $\zeta$ -potential theory.

Usually, DLS instruments permit also  $\zeta$ -potential measurements by means of laser Doppler electrophoresis. NPs in suspension are loaded in electrodes bearing capillary cells, where an electric field is applied. As NPs moves by electrophoresis, the light of a laser is scattered and detected at a fixed angle: a fluctuating intensity signal is produced with the rate of fluctuation proportional to the speed of the particles.  $\zeta$ -potential is automatically derived from electrophoretic mobility based on the Helmholtz-Smoluchowski theory:

$$U_E = \frac{2\varepsilon\zeta f(Ka)}{3\eta}$$

where  $U_E$ : electrophoretic mobility,  $\varepsilon$ : dielectric constant,  $\eta$ : viscosity,  $\zeta$ : zeta potential,  $f(K_a)$ : Henry's function. Generally, particles with zeta potential more positive than +30 mV or more negative than -30 mV have colloidal stability maintained by electrostatic repulsion. The most important factor that affect z-potential is pH, so that a z-potential value without a quoted pH is a virtually meaningless value.

### 1.3.3 – Morphology

Transmission electron microscopy (TEM) is a high magnification measurement technique that images the transmission of a beam of electrons through a sample. Amplitude and phase variations in the transmitted beam provide imaging contrast that is a function of the sample thickness (the amount of material that the electron beam must pass through) and the sample material (heavier atoms scatter more electrons and therefore have a smaller electron mean free path than lighter atoms). Because this technique uses electrons rather than light to illuminate the sample, TEM imaging has significantly higher resolution than light-based imaging techniques. Successful imaging of nanoparticles using TEM depends on the contrast of the sample relative to the background. Samples are prepared for imaging by drying nanoparticles on a copper grid that is coated with a thin layer of carbon. Materials with electron densities that are significantly higher than amorphous carbon are easily imaged. These materials include most metals (e.g., silver, gold, copper, aluminum), most oxides (e.g., silica, aluminum oxide, titanium oxide), and other particles such as polymer nanoparticles, carbon nanotubes, quantum dots, and magnetic nanoparticles. TEM imaging is the preferred method to directly measure the particle size, grain size, size distribution, and morphology of nanoparticles. Sizing accuracy is typically within 3% of the actual value.

## References

1. Wiley: Introduction to Nanomedicine and Nanobioengineering - Paras N. Prasad (accessed Jun 15, 2016).
2. Fakruddin, M.; Hossain, Z.; Afroz, H. Prospects and applications of nanobiotechnology: a medical perspective. *J. Nanobiotechnology* **2012**, *10*, 31.
3. Bobo, D.; Robinson, K. J.; Islam, J.; Thurecht, K. J.; Corrie, S. R. Nanoparticle-Based Medicines: A Review of FDA-Approved Materials and Clinical Trials to Date. *Pharm. Res.* **2016**, 1–15.
4. Kim, B. Y. S.; Rutka, J. T.; Chan, W. C. W. Nanomedicine. *N. Engl. J. Med.* **2010**, *363*, 2434–2443.
5. Ma, X.; Gong, N.; Zhong, L.; Sun, J.; Liang, X.-J. Future of nanotherapeutics: Targeting the cellular sub-organelles. *Biomaterials* **2016**, *97*, 10–21.
6. Karimi, M.; Ghasemi, A.; Zangabad, P. S.; Rahighi, R.; Basri, S. M. M.; Mirshekari, H.; Amiri, M.; Pishabad, Z. S.; Aslani, A.; Bozorgomid, M.; Ghosh, D.; Beyzavi, A.; Vaseghi, A.; Aref, A. R.; Haghani, L.; Bahrami, S.; Hamblin, M. R. Smart micro/nanoparticles in stimulus-responsive drug/gene delivery systems. *Chem. Soc. Rev.* **2016**, *45*, 1457–1501.
7. Ma, X.; Zhao, Y.; Liang, X.-J. Theranostic nanoparticles engineered for clinic and pharmaceuticals. *Acc. Chem. Res.* **2011**, *44*, 1114–1122.
8. Jain, K. Drug Delivery Systems - An Overview. In *Drug Delivery Systems*; Jain, K., Ed.; Methods in Molecular Biology<sup>TM</sup>; Humana Press, 2008; pp. 1–50.
9. Liu, D.; Yang, F.; Xiong, F.; Gu, N. The Smart Drug Delivery System and Its Clinical Potential. *Theranostics* **2016**, *6*, 1306–1323.
10. Bertrand, N.; Wu, J.; Xu, X.; Kamaly, N.; Farokhzad, O. C. Cancer nanotechnology: the impact of passive and active targeting in the era of modern cancer biology. *Adv. Drug Deliv. Rev.* **2014**, *66*, 2–25.
11. E. Rosen, J.; Yoffe, S.; Meerasa, A. Nanotechnology and Diagnostic Imaging: New Advances in Contrast Agent Technology. *J. Nanomedicine Nanotechnol.* **2011**, *02*.
12. Yang, C.-T.; Padmanabhan, P.; Gulyás, B. Z. Gadolinium(III) based nanoparticles for T1-weighted magnetic resonance imaging probes. *RSC Adv.* **2016**, *6*, 60945–60966.
13. Rui, Y.-P.; Liang, B.; Hu, F.; Xu, J.; Peng, Y.-F.; Yin, P.-H.; Duan, Y.; Zhang, C.; Gu, H. Ultra-large-scale production of ultrasmall superparamagnetic iron oxide nanoparticles for T1-weighted MRI. *RSC Adv.* **2016**, *6*, 22575–22585.
14. Wei, B.; Zhang, X.; Zhang, C.; Jiang, Y.; Fu, Y.-Y.; Yu, C.; Sun, S.-K.; Yan, X.-P. Facile Synthesis of Uniform-Sized Bismuth Nanoparticles for CT Visualization of Gastrointestinal Tract in Vivo. *ACS Appl. Mater. Interfaces* **2016**, *8*, 12720–12726.
15. You, S.; Jung, H.; Lee, C.; Choe, Y. H.; Heo, J. Y.; Gang, G.-T.; Byun, S.-K.; Kim, W. K.; Lee, C.-H.; Kim, D.-E.; Kim, Y. I.; Kim, Y. High-performance dendritic contrast agents for X-ray computed tomography imaging using potent tetraiodobenzene derivatives. *J. Controlled Release* **2016**, *226*, 258–267.
16. Hainfeld, J. F.; Slatkin, D. N.; Focella, T. M.; Smilowitz, H. M. Gold nanoparticles: a new X-ray contrast agent. *Br. J. Radiol.* **2006**, *79*, 248–253.

17. Pellico, J.; Ruiz-Cabello, J.; Saiz-Alía, M.; del Rosario, G.; Caja, S.; Montoya, M.; Fernández de Manuel, L.; Morales, M. P.; Gutiérrez, L.; Galiana, B.; Enríquez, J. A.; Herranz, F. Fast synthesis and bioconjugation of <sup>68</sup>Ga core-doped extremely small iron oxide nanoparticles for PET/MR imaging. *Contrast Media Mol. Imaging* **2016**, *11*, 203–210.
18. Cai, W.; Chen, X. Nanoplatfoms for Targeted Molecular Imaging in Living Subjects. *Small* **2007**, *3*, 1840–1854.
19. Phillips, E.; Penate-Medina, O.; Zanzonico, P. B.; Carvajal, R. D.; Mohan, P.; Ye, Y.; Humm, J.; Gönen, M.; Kalaigian, H.; Schöder, H.; Strauss, H. W.; Larson, S. M.; Wiesner, U.; Bradbury, M. S. Clinical translation of an ultrasmall inorganic optical-PET imaging nanoparticle probe. *Sci. Transl. Med.* **2014**, *6*, 260ra149–260ra149.
20. Vacanti, J. P.; Langer, R. Tissue engineering: the design and fabrication of living replacement devices for surgical reconstruction and transplantation. *Lancet Lond. Engl.* **1999**, *354 Suppl 1*, SI32–34.
21. Danie Kingsley, J.; Ranjan, S.; Dasgupta, N.; Saha, P. Nanotechnology for tissue engineering: Need, techniques and applications. *J. Pharm. Res.* **2013**, *7*, 200–204.
22. Engel, E.; Michiardi, A.; Navarro, M.; Lacroix, D.; Planell, J. A. Nanotechnology in regenerative medicine: the materials side. *Trends Biotechnol.* **2008**, *26*, 39–47.
23. Zhao, J.; Zhang, Z.; Shen, G.; Zhang, X. Enhanced osteogenic activity and anti-inflammatory properties of Lenti-BMP-2-loaded TiO<sub>2</sub> nanotube layers fabricated by lyophilization following trehalose addition. *Int. J. Nanomedicine* **2016**, 429.
24. Kim, H.; Kim, I.; Choi, H.-J.; Kim, S. Y.; Yang, E. G. Neuron-like differentiation of mesenchymal stem cells on silicon nanowires. *Nanoscale* **2015**, *7*, 17131–17138.
25. Taeho Kongbo Calcium phosphate cement composition comprising zinc-bioglass nanoparticles and a kit for preparing the same 2016.
26. Domingues, R. M. A.; Chiera, S.; Gershovich, P.; Motta, A.; Reis, R. L.; Gomes, M. E. Enhancing the Biomechanical Performance of Anisotropic Nanofibrous Scaffolds in Tendon Tissue Engineering: Reinforcement with Cellulose Nanocrystals. *Adv. Healthc. Mater.* **2016**, *5*, 1364–1375.
27. Kojima, R.; Aubel, D.; Fussenegger, M. Novel theranostic agents for next-generation personalized medicine: small molecules, nanoparticles, and engineered mammalian cells. *Curr. Opin. Chem. Biol.* **2015**, *28*, 29–38.
28. Wu, Y.-F.; Wu, H.-C.; Kuan, C.-H.; Lin, C.-J.; Wang, L.-W.; Chang, C.-W.; Wang, T.-W. Multi-functionalized carbon dots as theranostic nanoagent for gene delivery in lung cancer therapy. *Sci. Rep.* **2016**, *6*, 21170.
29. Chen, G.; Roy, I.; Yang, C.; Prasad, P. N. Nanochemistry and Nanomedicine for Nanoparticle-based Diagnostics and Therapy. *Chem. Rev.* **2016**, *116*, 2826–2885.
30. Xu, Z.; Shen, C.; Hou, Y.; Gao, H.; Sun, S. Oleylamine as Both Reducing Agent and Stabilizer in a Facile Synthesis of Magnetite Nanoparticles. *Chem. Mater.* **2009**, *21*, 1778–1780.
31. Colombo, M.; Sommaruga, S.; Mazzucchelli, S.; Polito, L.; Verderio, P.; Galeffi, P.; Corsi, F.; Tortora, P.; Prospero, D. Site-Specific Conjugation of ScFvs Antibodies to Nanoparticles by Bioorthogonal Strain-Promoted Alkyne–Nitrene Cycloaddition. *Angew. Chem. Int. Ed.* **2012**, *51*, 496–499.

32. Corsi, F.; Fiandra, L.; De Palma, C.; Colombo, M.; Mazzucchelli, S.; Verderio, P.; Allevi, R.; Tosoni, A.; Nebuloni, M.; Clementi, E.; Prospero, D. HER2 Expression in Breast Cancer Cells Is Downregulated Upon Active Targeting by Antibody-Engineered Multifunctional Nanoparticles in Mice. *ACS Nano* **2011**, *5*, 6383–6393.
33. Cichos, J.; Karbowiak, M. A general and versatile procedure for coating of hydrophobic nanocrystals with a thin silica layer enabling facile biofunctionalization and dye incorporation. *J. Mater. Chem. B* **2014**, *2*, 556–568.
34. Sodipo, B. K.; Aziz, A. A. Recent advances in synthesis and surface modification of superparamagnetic iron oxide nanoparticles with silica. *J. Magn. Magn. Mater.* **2016**, *416*, 275–291.
35. Li, Z.; Yuan, D.; Jin, G.; Tan, B. H.; He, C. Facile Layer-by-Layer Self-Assembly toward Enantiomeric Poly(lactide) Stereocomplex Coated Magnetite Nanocarrier for Highly Tunable Drug Deliveries. *ACS Appl. Mater. Interfaces* **2016**, *8*, 1842–1853.
36. Avvakumova, S.; Colombo, M.; Tortora, P.; Prospero, D. Biotechnological approaches toward nanoparticle biofunctionalization. *Trends Biotechnol.* **2014**, *32*, 11–20.
37. Hermanson, G. T. Chapter 4 - Zero-Length Crosslinkers. In *Bioconjugate Techniques (Third edition)*; Academic Press: Boston, 2013; pp. 259–273.
38. Northrop, B. H.; Frayne, S. H.; Choudhary, U. Thiol–maleimide “click” chemistry: evaluating the influence of solvent, initiator, and thiol on the reaction mechanism, kinetics, and selectivity. *Polym. Chem.* **2015**, *6*, 3415–3430.
39. Finetti, C.; Sola, L.; Pezzullo, M.; Prospero, D.; Colombo, M.; Riva, B.; Avvakumova, S.; Morasso, C.; Picciolini, S.; Chiari, M. Click Chemistry Immobilization of Antibodies on Polymer Coated Gold Nanoparticles. *Langmuir* **2016**, *32*, 7435–7441.
40. Neouze, M.-A.; Schubert, U. Surface Modification and Functionalization of Metal and Metal Oxide Nanoparticles by Organic Ligands. *Monatshfte Für Chem. - Chem. Mon.* **2008**, *139*, 183–195.
41. Dynamic light scattering - common terms defined <http://www.malvern.com/en/support/resource-center/Whitepapers/WP111214DLSTermsDefined.aspx> (accessed Sep 13, 2016).
42. Blanco, E.; Shen, H.; Ferrari, M. Principles of nanoparticle design for overcoming biological barriers to drug delivery. *Nat. Biotechnol.* **2015**, *33*, 941–951.



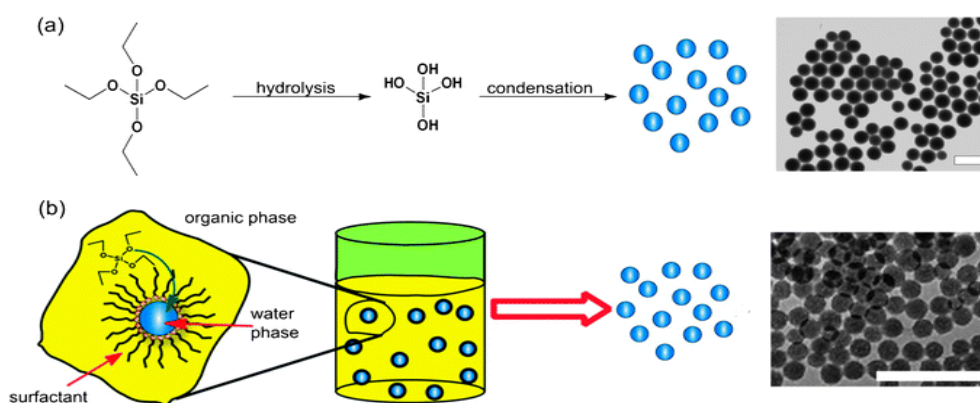
**CHAPTER 2**  
**THERANOSTIC AGENT**

## 2.1- Nonporous silica nanoparticles

Silica nanoparticles (SNPs) are counted in the inorganic nanomedicines that have emerged as promising alternatives to organic systems for a wide range of biomedical applications. In fact they possess distinctive characteristics such as size (generally from 5 to 1000 nm), unique optical properties, low density, adsorption capacity, hydrophilic surface favoring protracted blood circulation, versatile chemistry for functionalization, excellent biocompatibility, low toxicity, and the possibility of a large scale production with low cost procedures and reactants [1]. Consequently, intensive research has been performed to use SNPs in diverse cutting edge biomedical applications such as biosensors, controlled drug release and cellular uptake. SNPs are splitted into two categories, namely mesoporous and nonporous SNPs, both of which bearing amorphous silica structure. Mesoporous SNPs are mainly used as drug delivery systems as they can be produced with fine control over pore size and structures and loaded by physical or chemical adsorption with various payloads, whose release can be controlled using gatekeepers or modifying the inner surface to control the binding affinity [2]. In contrast, nonporous SNPs, which can be prepared with excellent control over size and shape, deliver their cargo through encapsulation or conjugation and release them by means of chemical linkers or by matrix degradation. For the purpose of this thesis, a brief overview about nonporous SNPs will be given in the next paragraphs.

### 2.1.1 – Size, shape and surface properties

Several synthesis techniques have been developed to produce particles with narrow size distribution and nearly uniform shape. The most common method to prepare size-controlled nonporous SNPs was firstly described by Stöber in 1968 [3] and consists in hydrolysis/condensation of TEOS or other silicates in a mixture of water, alcohol and ammonia (Figure 2.1, a). The particle nucleation proceeds through a siloxane substructure aggregation that is strongly influenced by the surface potential of SNPs and the ionic strength of the reaction medium [4]. Thus, many investigations on the kinetics and parameters guiding Stöber synthesis have been conducted to precisely control size, shape and uniformity of the resulting SNPs. First of all, it was found a strong dependence of the final particle size and morphology on the concentration of ammonia and water, making it possible to tune the particle size range from 20 to 100 nm by simply adjusting the reagent content [4,5]. Other studies demonstrated a correlation between the rate of addition of TEOS and the resulting SNP diameter, obtaining smaller particles with faster silicate addition [6].



**Figure 2.1** Methods for preparing nonporous SNPs and corresponding TEM images. (a) The Stober method; (b) the reverse microemulsion method [7].

An alternative method for the production of uniform silica spheres is the reverse microemulsion method (Figure 2.1, b) in which particles nucleate inside inverse micelles compartmentalized by a suitable surfactant in a non-polar organic solvent [8]. This approach is particularly successful for SNPs smaller than 100 nm in diameter, eventually allowing for the encapsulation of active molecules by introducing them into the micelles together with silicates [9], and it is also widely used for coating other NPs to produce core-shell structures [10]. Although there are many methods to produce various-sized spherical SNPs, much lesser studies report the production of differently shaped SNPs. Nevertheless, the shape control of SNPs, as well as for all other NPs, is of fundamental importance to understand shape effect in biological systems for improved biomedical application of nanotechnologies. Usually the methods for shape control of SNPs include the participation of various templates or polymer adsorption that guide the growth of nanorods [11], nanorattles [12] or hollow SNPs [13]. Another important feature in SNPs synthesis is the tuning of surface properties, as they are known to play an important role in determining the interactions with biological systems [14]. Surface modification of SNPs is most easily achieved by reaction with one of the many commercially available alkoxy silanes/halosilanes that can be condensed with the silanol groups on the NP surface. For example, the surface charge can be modified with the addition of aminosiloxanes or zwitterionic silanes, while various PEG-silanes are frequently exploited to improve the stability in biological fluids, the biocompatibility and circulating time *in vivo*. Many other functional groups can be introduced either by covalent grafting or physical adsorption to facilitate the immobilization of linkers suitable for the conjugation with drugs, fluorophores or targeting moieties, such as antibodies or aptamers.

### 2.1.2 – Application in biomedical research

As mentioned before, SNPs find various applications in biomedical field due to their numerous advantages over other organic and inorganic NPs: they are biocompatible and “generally recognized as safe” by the U.S. FDA (GRAS number 321 and 554) [15], they can be tailored in size and shape, and they can be easily functionalized or loaded with active molecules or contrast agents. Once internalized in the nanostructure, the loaded species obtain increased chemical stability, a protection from enzymatic degradation and an almost constant chemical environment. Moreover, SNPs are transparent in the ultraviolet, visible and near infrared regions and they do not interfere with the magnetic radiation. The ability to combine these properties makes SNPs an ideal platform for biomedical imaging, assaying, therapeutic delivery, monitoring, and ablative therapies. It is worth mentioning that the first clinical trial for the so-called Cornell-dots (C-dots) was approved by FDA in 2011 [16,17]. C-dots are fluorescent core-shell nonporous SNPs with a diameter of 7-10 nm which covalently incorporate organic dyes to prevent dye leaching, while being coated by PEG to prevent opsonization and enhance particle clearance [18]. Moreover, these particles are labeled with  $^{124}\text{I}$  for PET imaging and modified with specific peptides for molecular targeting of metastatic melanoma. The results of the first-in-human trial demonstrated C-dot *in vivo* stability, reproducible pharmacokinetic profile defined by renal excretion, no toxic or adverse events, together with preferential and localized uptake in the site of interest, thus suggesting a safe use of C-dots in human cancer diagnosis [19]. In addition to this, hundreds of studies can be find in the literature, presenting proof-of-concept usage of SNPs for cell-surface receptor targeting, intracellular sensing and controlled drug delivery, confirming the high interest for this nanostructure [1]. However, before SNPs can be used routinely in clinic, some major challenges must be overcome, including improved drug incorporation efficiency, spatial and temporal control of drug release, highly efficient targeting of disease sites, long-term stability and potential size-related toxicity.

## **2.2 – HER2 positive breast cancer: characteristics, diagnosis and therapy**

Breast cancer (BC) is the most common tumor in women, being the second cause of death due to cancer [20]. It is a very heterogeneous disease, having many subtypes that can be classified from histological point of view in *in situ* or invasive carcinomas, or classified basing on expressed molecular markers (Table 2.1). The latter classification appears particularly important to search for appropriate addressed therapies. Statistically, BCs overexpressing

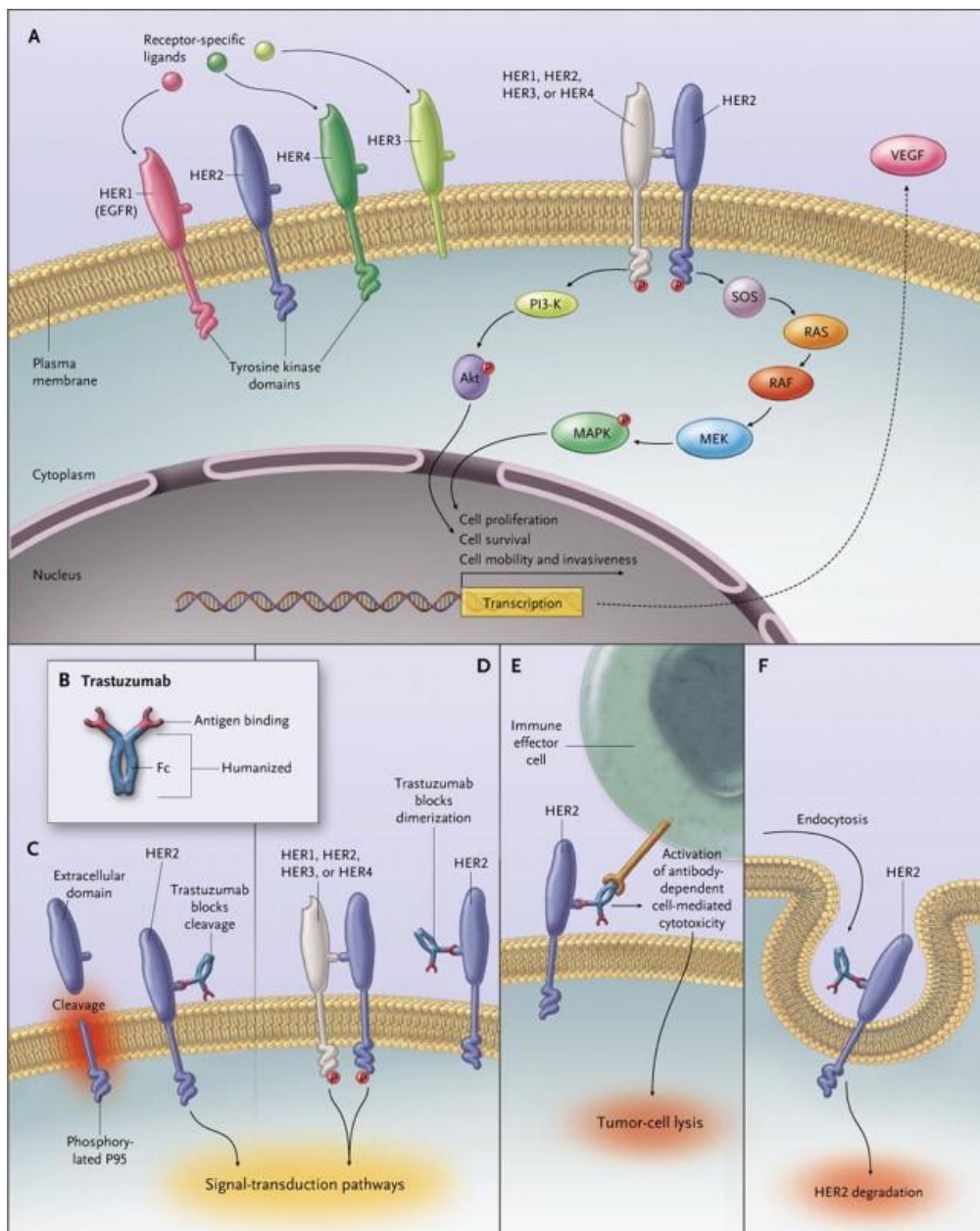
HER2, namely HER2 positive (HER2<sup>+</sup>) BCs, account for 30% of invasive breast tumors and are associated with an aggressive behavior, great probability of lymph node involvement and increased resistance to endocrine therapy [21]. HER2 is a member of the epidermal growth factor receptor family and include a cysteine-rich extracellular ligand binding site, a transmembrane lipophilic segment, and an intracellular domain with tyrosine kinase catalytic activity. An essential requirement for its function is the dimerization that occurs after ligand binding to the extracellular domain; once HER2 has formed homodimers or heterodimers with other growth factor receptors, a key intracellular pathway is activated, governing cellular processes such as proliferation and cell survival (Figure 2.2, A). In cancer cells, this pathway is overactivated resulting in a stimulation of cell proliferation and survival, together with tumor migration, differentiation and angiogenesis [22].

**Table 2. 1** Molecular classification of breast cancer subtypes

<b>BC SUBTYPES</b>	<b>SPECIFIC BIOMARKERS</b>	<b>PERCENTAGE OF BC</b>
<b>Basal-like Triple Negative</b>	ER <sup>-</sup> PR <sup>-</sup> HER2 <sup>-</sup> EGFR <sup>+</sup>	15-20 %
<b>HER2<sup>+</sup></b>	HER2 <sup>+</sup> ER <sup>-</sup> PR <sup>-</sup>	10-15 %
<b>Luminal subtypes A</b>	ER <sup>+</sup> HER2 <sup>-</sup> PR <sup>low</sup>	25-30 %
<b>Luminal subtypes B</b>	ER <sup>+</sup> HER2 <sup>+</sup> PR <sup>low</sup>	20%

### 2.2.1 – Therapy

The extracellular domain of HER2 has been the target of several monoclonal antibodies projected to inhibit the proliferation of tumor cells. So far, the humanized murine monoclonal antibody Trastuzumab (Herceptin ®, Genetech-Roche) is the only anti-HER2 agent that is approved for adjuvant therapy in patients who have HER2<sup>+</sup> disease, either in combination with chemotherapy or alone after chemotherapy [23]. Trastuzumab (TZ) consists in two antigen-specific sites that bind the extracellular domain of HER2, exerting antitumor activity through several molecular mechanisms (Figure 2.2, B-F) [24]. It was firstly introduced in addition to chemotherapy for patients with metastatic HER2<sup>+</sup> BC, leading to a significant survival prolongation and 20% reduction in the risk of death [25]; afterwards it was also shown to exert significant benefits in disease-free and overall survival for patients with early stage HER2<sup>+</sup> BC [26]. Despite this success, approximately 35% of patient with HER2 overexpression responds to TZ therapy and around 10-15% of those patients experiences disease recurrence and TZ resistance [27].



**Figure 2.2** Signal transduction by the HER family and mechanism of action of trastuzumab. A) The four members of the HER family: HER1, HER2, HER3, HER4; B-F) the most well-documented mechanisms of action of trastuzumab.

### 2.2.2 – Diagnosis

In order to have a benefit from TZ or other treatment options, the detection of HER2 expression remains a fundamental issue. Nowadays, HER2 expression is evaluated in post-surgery or bioptic specimen by immunohistochemistry (IHC), that evaluates the intensity and distribution of cell membrane HER2 expression, or by fluorescence in-situ hybridization (FISH), which quantifies HER2 gene amplification. FISH test is presently considered the “gold

standard”, but it is costly and time-consuming compared to IHC. In practice, most laboratories firstly employ IHC to classify HER2 expression using a four-point scale and utilize a confirmatory FISH technique for a definitive assessment of HER2 status in tumors with borderline scores [28]. In 2007, the American Society of Clinical Oncology (ASCO) and the College of American Pathologist (CAP) developed guidelines for the employment and interpretation of HER2 testing to reduce variability between laboratories and uncertainty of oncologists when determining patient eligibility for treatment [29]. An update in the ASCO/CAP guideline was made in 2013 to further reduce the incidence of false negative results [30]. IHC and FISH techniques are daily employed in HER2<sup>+</sup> BC detection, but still represent invasive methods.

### **2.3 – Design of a new theranostic agent for the targeted detection and therapy of HER2<sup>+</sup> breast cancer**

In the effort to improve life conditions and survivals of women with HER2<sup>+</sup> BC, the possibility to imagine non-invasive detection and targeted delivery of cytotoxic agent, avoiding or decreasing side effects, appears an ideal point of landing. Our project fits into this field, aiming at having a targeted detection combined with localized drug delivery thanks to a multifunctional silica-based nanoconjugate. The development of our theranostic nanoplatform is based on three principal concepts:

- a) the usage of **TZ** as a targeting ligand to guide the nanodevice selectively and with high affinity to HER2-overexpressing BC cells;
- b) the introduction of a suitable radionuclide, namely the <sup>99m</sup>Tc, to be detected *in vivo* by nuclear medicine imaging techniques, such as Positron Emission Tomography (PET) or Single Photon Emission Computed Tomography (SPECT);
- c) the loading of the anthracycline antitumor drug **doxorubicin** as a therapeutic agent.

In addition to the well documented therapeutic potential, **TZ** has also been investigated as conjugate for its effectiveness in guiding various targeted systems to HER2<sup>+</sup> cells. A single antibody molecule bears two epitope-binding sites with high binding affinity toward HER2, while the surface contains free functional groups that allow for the conjugation. Indeed, TZ has been linked to a variety of nanocarriers for imaging, drug delivery and gene therapy, in order to selectively transport active agents into HER2<sup>+</sup> cells by means of a receptor-mediated endocytosis [31]. Recently, in order to determine the best for of antibody conjugate in terms of targeting performance, HER2-directed colloidal NPs engineered with three different TZ

derivatives were investigated both *in vitro* and in a HER2<sup>+</sup> BC murine model. When the half chain of the antibody (Hc-TZ) was linked to the surface, the NPs experienced a higher and long lasting accumulation at the tumor [32]. Considering the preservation of the targeting activity and the advantages in conjugating a smaller moiety, Hc-TZ was chosen to be the targeting agent for our SNPs.

Molecular imaging techniques as PET and SPECT allow the *in vivo* detection of molecular targets during tumor progression and diffusion; in particular they can be exploited to visualize and quantify the presence/absence of biological markers by means of specific radiolabeled probes, administered at tracer doses [33]. Hence, these techniques may allow the assessment of HER2 expression both in primary and secondary lesions not amenable to biopsy [34]. Among the radionuclides currently used in nuclear medicine, <sup>99m</sup>Tc was the elected radioisotope for our purposes: it offers the advantage of easy availability thanks to the presence of clinical grade generators and its short half-life (*ca.* 6 h) makes it suitable for administration in mCi amounts without significant radiation dose to the patient. In addition, due to its chemical properties, it can be coordinated in a stable oxidation state by bi- and tridentate ligands represented either by small functional linkers, such as hydrazinonicotinic acid [35] and nitrilotriacetic acid [36], or by aminoacidic residues, such as histidine and cysteine [37].

**Doxorubicin** represents one of the most commonly used chemotherapeutic anthracyclines in clinical practice. Its cytotoxicity is primarily due to DNA intercalation which inhibits the action of Topoisomerase II, leading to an interruption of the DNA transcription. Other proposed mechanisms for its antitumor activity involve lipid peroxidation, direct membrane effects and free radical formation. Nevertheless, doxorubicin is often accompanied by severe side effects, the most significant being the cardiotoxicity of the metabolites like the secondary alcohol doxorubicinol or the production of reactive oxygen species (ROS) [38]. It is therefore desirable to carry it at the right site of action and release it in a controlled fashion, to improve its efficacy and reduce adverse effects.

Our work was organized in two steps: first we developed a silica-based nanocarrier for the targeted detection of HER2<sup>+</sup> cells and in the second part the possibility to formulate doxorubicin in the same nanoconstruct was investigated.



## **(i) Development of radiolabeled SNPs for the targeted detection of HER2-positive breast cancer.**

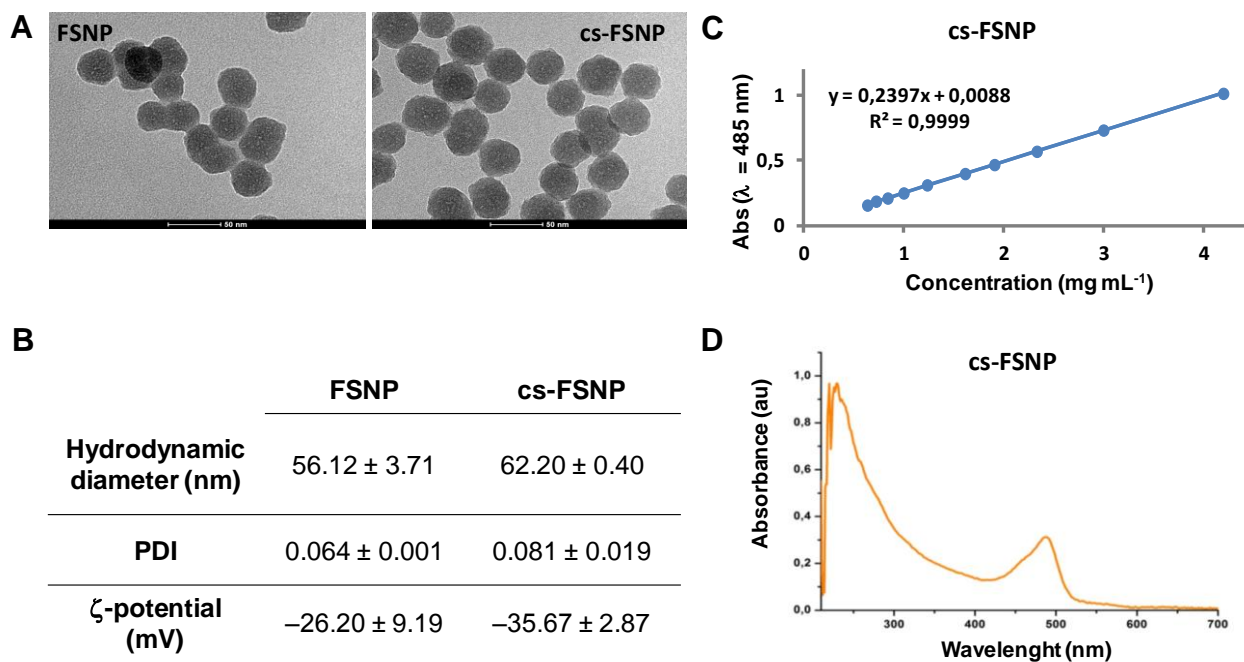
### **2.4 – Aim of the project**

In the first part of the development of a silica based theranostic agent, we explored the use of multifunctional radiolabeled SNPs for early detection of HER2<sup>+</sup> BC lesions. SNPs were engineered to be easy to detect by fluorescence microscopy, to actively target HER2<sup>+</sup> cancer cells and to be used as radiotracer for SPECT imaging. Once the synthetic protocol was set up, we investigated the contribution offered by active targeting to the distribution of NPs in solid BC lesion and in cell internalization, in comparison to nonspecifically targeted SNPs. Moreover, we checked out the possibility to follow the *in vitro* uptake and *ex vivo/in vivo* biodistribution of SNPs through nuclear medicine techniques.

### **2.5 – Results and discussion**

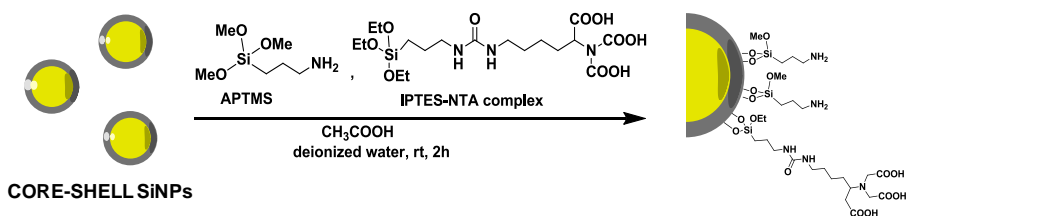
#### 2.5.1 – Synthesis and characterization of SNPs

Monodisperse spherical SNPs were chosen as starting material to generate biocompatible multifunctional nanoconjugates. Firstly, in order to have a fluorescent detectable carrier, the dense core of the SNPs was loaded with a fluorophore (FSNP), following a modified Stöber synthesis [5] consisting in a hydrolysis-condensation reaction of a mixture of TEOS and previously prepared APTMS-FITC complex in ethanolic ammonia solution. The fluorescent core was then protected by a denser silica shell (cs-FSNP), necessary to prevent the undesired cargo release and limit the dye bleaching that often leads to misleading optical artifacts. This was obtained by a biosilicification reaction catalyzed by L-arginine leading to a uniform 5 nm-thick shell [39]. The as-prepared core-shell SNPs exhibited narrow size distribution and good colloidal stability as evidenced by TEM images and DLS measurements (Fig 2.3, A and B). Moreover, the presence of FITC was exploited to derive a relation between its absorption and NP concentration; during the subsequent synthetic steps the as-built calibration curve made it possible to determine NP concentration in suspension (Figure 2.3, C and D). After the NP fabrication, we optimized the functionalization steps in order to introduce two main functionalities: Hc-TZ as targeting moiety for the recognition of the HER2 receptor in HER2<sup>+</sup> cancer and <sup>99m</sup>Tc as a radioisotope for SPECT imaging. First of all, in order to attach and retain the radionuclide, we decided to exploit the nitrilotriacetic acid linker, whose application as radiotracer chelating agent is widely described in the literature [36].

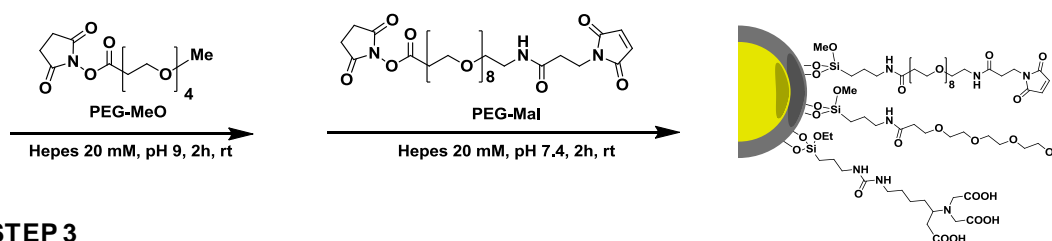


**Figure 2.3** Characterization of fluorescent SNPs (FSNP) and core-shell FSNP (cs-FSNP). A) TEM images, B) size, polydispersity index (PDI) and  $\zeta$ -potential values obtained by DLS measurements, C) calibration curve correlating FITC absorbance and cs-FSNP concentrations, D) example of a UV absorption spectrum of cs-FSNP evidencing the FITC absorbance peak at  $\lambda=485$  nm.

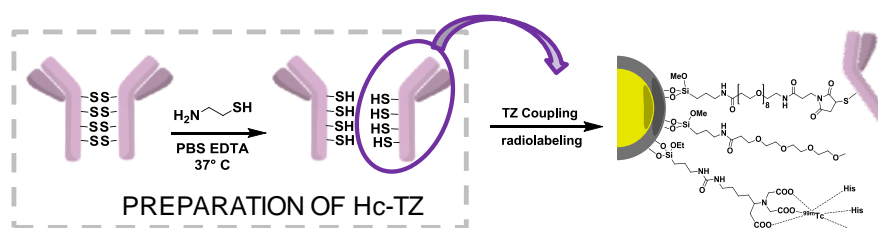
### STEP 1



### STEP 2



### STEP 3



**Scheme 2.1** Schematic representation of the synthetic steps for the preparation of SiNP-NTA-TZ.

Hence, a silane derivative (IPTES-NTA complex) was synthesized and grafted on the silica surface together with APTMS residues, thus introducing the chelating and amine functionalities in a one pot reaction (Scheme 2.1, step 1). After that, part of the amine residues was coupled to a short methoxy-terminating PEG for NP stabilization, while the remaining part was covalently linked with another heterobifunctional PEG containing a maleimido group (Scheme 2.1, step 2). After the reduction of disulfide bonds bridging the two chains of the antibody, the resulting thiol groups of the Hc-TZ were reacted with the maleimides, resulting in the immobilization of the antibody (Scheme 2.1, step 3). Finally, unreacted functional groups were saturated with a methoxyl terminating PEG and the NTA carboxylic moieties were engaged in Ni<sup>2+</sup> chelation before the radiolabeling step. As a result, the whole nanoconjugate consisted of a fluorescent core-shell structure modified with multiple functionalities, including a chelating group, a targeting moiety and a biocompatible PEG coating.

**Table 2.2** Chemical and physical properties of the silica nanoconjugates evaluated in the present study. Data are the mean  $\pm$  standard deviation of three different NP batches.

Nanoconjugate	Functionalization	Hydrodynamic diameter (nm)	PDI	$\zeta$ -potential (mV)
SiNP	Only PEG	85.59 $\pm$ 9.49	0.119 $\pm$ 0.091	-30.2 $\pm$ 0.3
SiNP-TZ	PEG + TZ	93.61 $\pm$ 6.22	0.095 $\pm$ 0.027	-31.6 $\pm$ 0.3
SiNP-NTA	PEG + NTA	123.9 $\pm$ 29.8	0.114 $\pm$ 0.024	-33.5 $\pm$ 6.6
SiNP-NTA-TZ	PEG + NTA + TZ	114.3 $\pm$ 0.7	0.084 $\pm$ 0.001	-33.6 $\pm$ 6.0

In order to evaluate the contribution of each functional moiety on the colloidal stability and on the fate of the resulting NPs, four types of silica nanoconjugates (SiNP, SiNP-TZ, SiNP-NTA and SiNP-NTA-TZ) were synthesized, differing from each other by the lack of one or more units. All the SNP conjugates were characterized in terms of hydrodynamic size and  $\zeta$ -potential (Table 2.2). SiNP and SiNP-TZ showed a hydrodynamic diameter (Hd) < 100 nm with good polydispersity indexes (PDI < 0.120). In contrast, the presence of the NTA linker, especially upon Ni<sup>2+</sup> ion chelation, led to a mild aggregation for SiNP-NTA and SiNP-NTA-TZ (Hd > 100 nm), which however was prevented after the radiolabeling procedure. The characteristic negative  $\zeta$ -potential of the SNPs was maintained for all kinds of nanoconjugates, which is an important prerequisite for low toxicity and systemic diffusion *in vivo* [40].

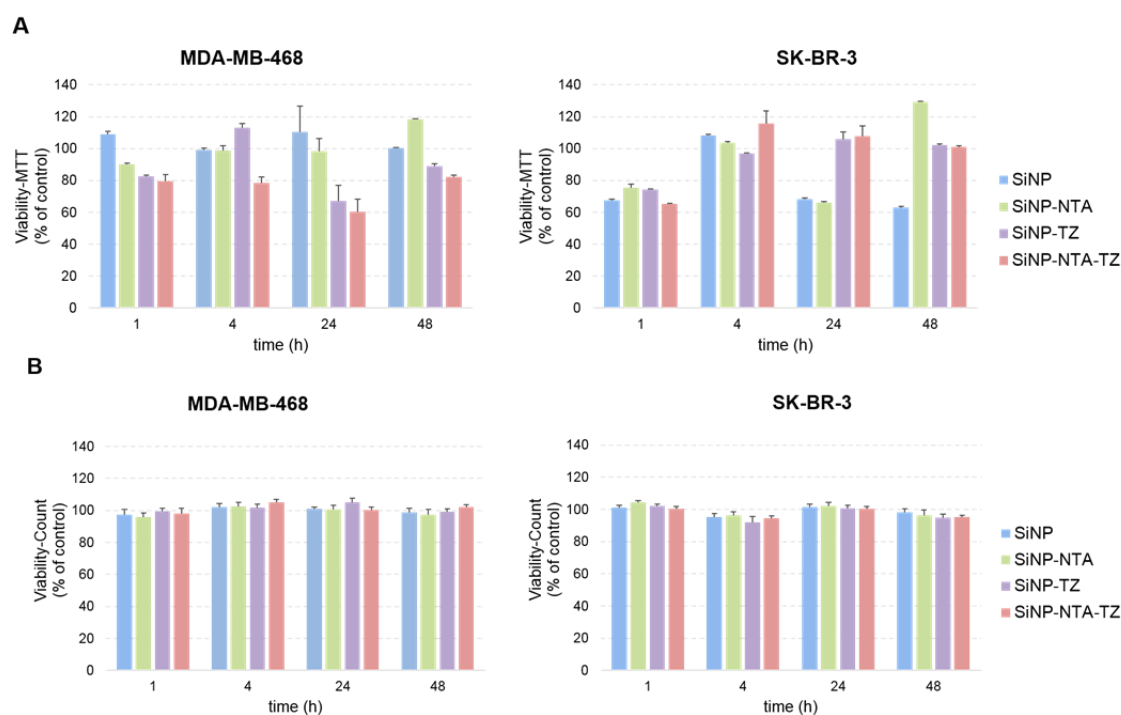
The radiolabeling protocol, developed at the department of Nuclear Medicine of San Raffaele Hospital (Milan), consisted in a three steps reaction (Scheme 2.2): I) prelabeling of a tricarbonyl

core with  $^{99m}\text{Tc}$ , according to the method published by Waibel et al. [41], resulting in the complex  $[\text{}^{99m}\text{Tc}(\text{CO})_3(\text{OH}_2)_3]^+$ , II) reaction with a hexa-histidine peptide (His-Tag), III) conjugation to NTA groups of SiNP-NTA and SiNP-NTA-TZ. The labeling yield was assessed by HPLC and resulted in a 25-35% range.



**Scheme 2.2** Schematic representation of the three-steps radiolabeling protocol for SiNP-NTA and SiNP-NTA-TZ preparation.

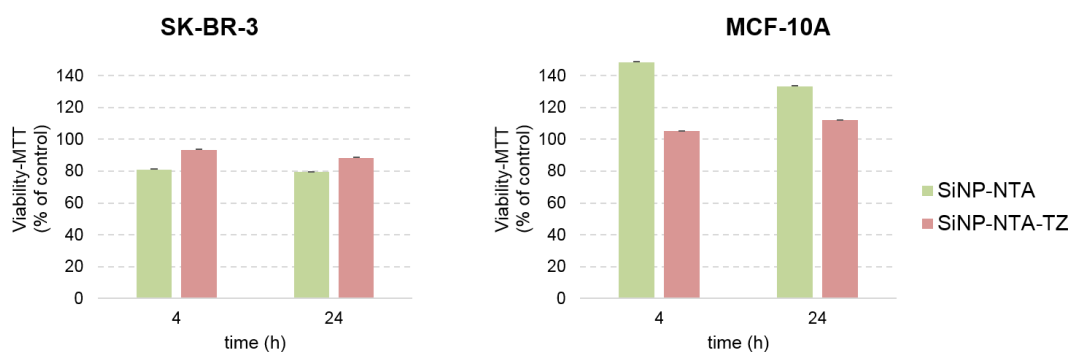
### 2.5.2 – *In vitro* toxicity and cell viability



**Figure 2.4** SNPs toxicity was investigated both by A) MTT and B) cell viability tests. SK-BR-3 and MDA-MB-468 cells were incubated with SNPs ( $100 \mu\text{g mL}^{-1}$ ) for 1, 4, 24 and 48 h.

After the preparation of the four nanoconjugates and before the labeling step, cell toxicity was assessed in  $\text{HER2}^+$  SK-BR-3 and  $\text{HER2}^-$  MDA-MB-468 BC cells using two types of test: the MTT test to check out the eventual change in mitochondrial metabolism and the cell viability. In both cases, all the engineered NPs did not affect the normal cell behavior up to 48 h, resulting in a maintained succinate dehydrogenase activity (MTT test, Figure 2.4, A) [42] and in a regular cell

proliferation (Figure 2.4, B) compared to untreated samples. In addition, MTT test was replicated in non-transformed mammary epithelial MCF-10A cell line (HER2<sup>-</sup> healthy cells) and confirmed the absence of cytotoxic effect caused by the NPs (Figure 2.5). Taken together, these results indicated a good profile of safety for all nanoconstructs in cultures of both tumor and healthy mammary cells.

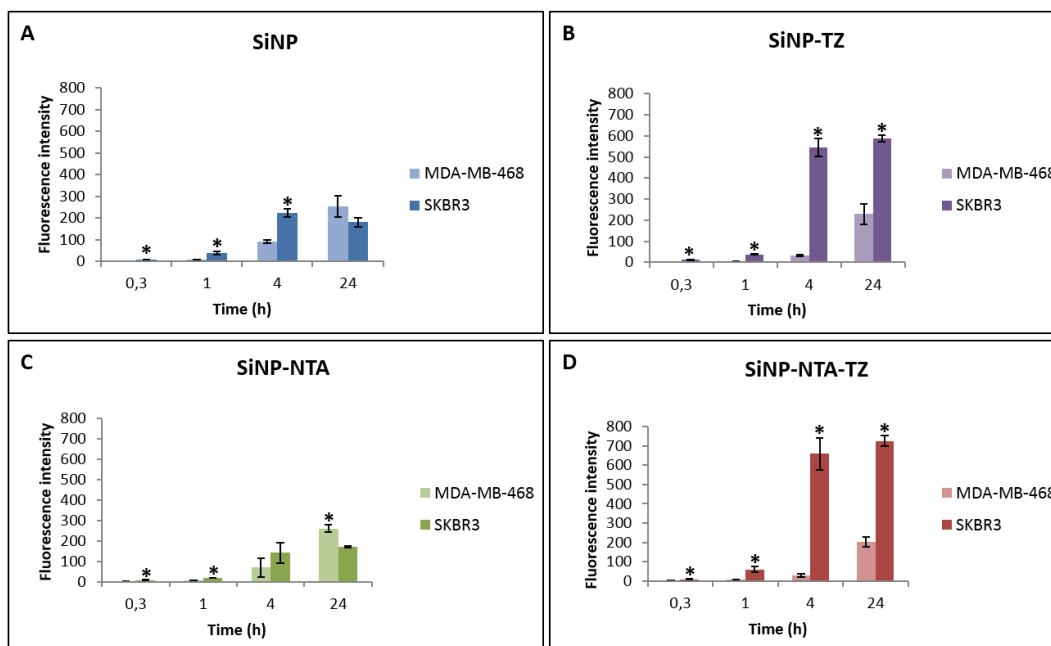


**Figure 2.5** MTT test was replicated at 4 and 24 h in non-transformed mammary epithelial MCF-10A cell line, (HER2<sup>-</sup>) in comparison to SK-BR-3 breast cancer cell line (HER2<sup>+</sup>), incubated with SiNP-NTA and SiNP-NTA-TZ.

### 2.5.3 – *In vitro* binding efficiency and selectivity

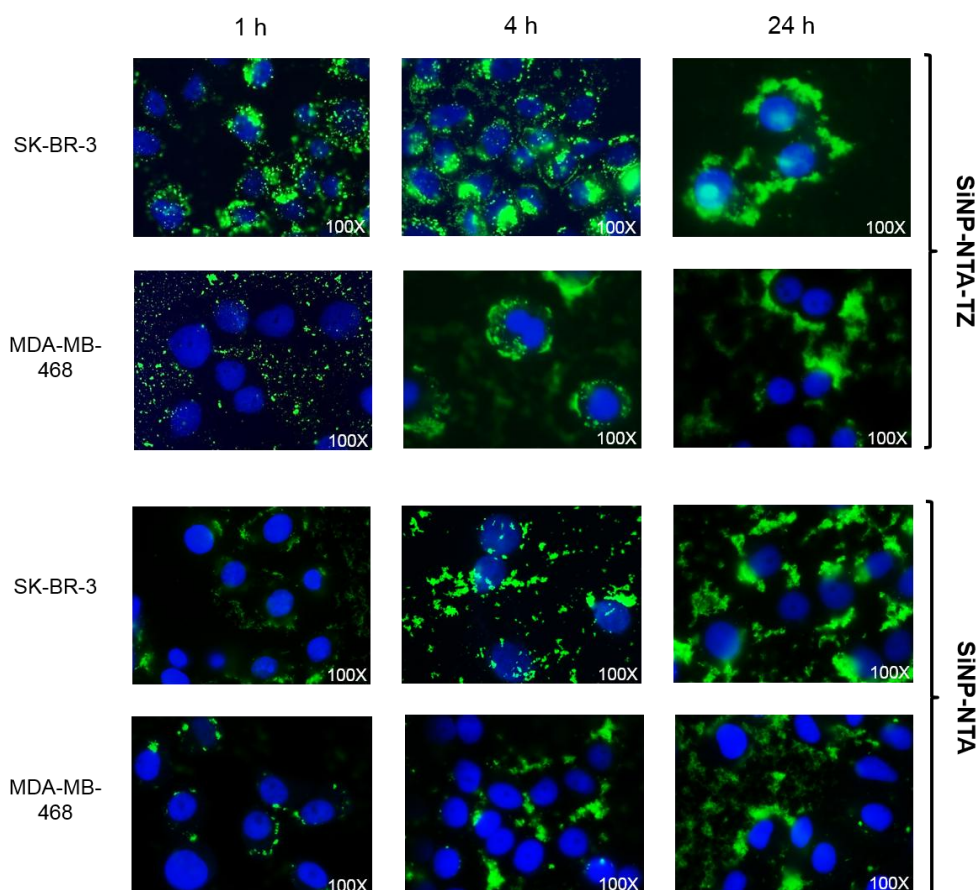
*In vitro* tests of the prepared NPs were performed both before and after the labeling step, aimed at assessing the binding efficiency and selectivity toward HER2<sup>+</sup> SK-BR-3 in comparison to HER2<sup>-</sup> MDA-MB-468 BC cells. For this purpose three different techniques were employed: flow cytometry and fluorescence imaging, both using the fluorescence of FITC loaded in the NPs, and  $\gamma$ -counter exploiting the presence of the radionuclide <sup>99m</sup>Tc.

Flow cytometry evidenced a remarkable time-dependent increase of fluorescence signal after incubation of SiNP-TZ/SiNP-NTA-TZ with SK-BR-3 cells (Figure 2.6, B and D), and a significant difference ( $p < 0.05$ ) compared to MDA-MB-468 cells. These data demonstrated the capability of targeted NPs to selectively recognize HER2 receptors in SK-BR-3 cells. SiNP/SiNP-NTA exhibited a remarkably lower uptake in SK-BR-3 cells compared to Hc-TZ-modified SNPs and no preferential affinity toward SK-BR-3 or MDA-MB-468 cell lines was recovered (Figure 2.6, A and C), suggesting that the interaction with cells was essentially attributable to nonspecific uptake in both HER2<sup>-</sup> or HER2<sup>+</sup> cells. However, nonspecific uptake was basically negligible within the first 4 h.

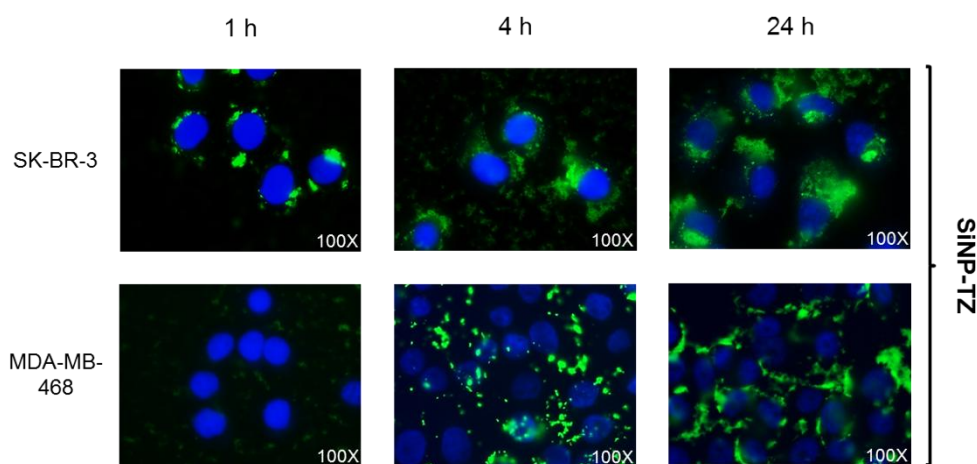


**Figure 2.6** Assessment of binding efficiency by flow cytometry. Panels A-D represent the distribution of cell fluorescence intensity, normalized over untreated cells (control), in MDA-MB-468 and SK-BR-3 cell lines after exposure to A) SiNP, B) SiNP-TZ, C) SiNP-NTA and D) SiNP-NTA-TZ at 20 min, 1 h, 4 h, 24 h, at a concentration of  $50 \mu\text{g mL}^{-1}$  (\* $p < 0.01$  vs. MDA-MB-468).

To validate these findings, the binding specificity of SiNP-NTA and SiNP-NTA-TZ for HER2<sup>+</sup> cells was assessed by fluorescence microscopy (Figure 2.7). Images of SNPs (green) overlaid on the corresponding images counterstained with DAPI (blue) show that in HER2<sup>+</sup> cells fluorescence intensity increased over time for SiNP-NTA-TZ and was considerably stronger than that shown in SiNP-NTA images. In contrast, we didn't observe any differences in the behavior of SiNP-TZ (Figure 2.8) and SiNP-NTA-TZ. In addition, SiNP-NTA fluorescence intensity showed no significant differences in both cell lines, confirming the loss of selectivity for SNPs in the absence of Hc-TZ conjugation. SK-BR-3 pictures acquired at 4 and 24 h exhibited a perinuclear localization of green fluorescence signals exclusively after incubation with SiNP-NTA-TZ, while the signal was not found in the cytoplasm of HER2<sup>-</sup> cells and remained localized outside the cells after 4 and 24 h of incubation. It was apparent that a large number of SiNP-TZ were internalized by HER2<sup>+</sup> SK-BR-3 cells, while they could be hardly taken up by HER2<sup>-</sup> MDA-MB-468 cells, confirming the specific targeting of Hc-TZ-functionalized SNPs for HER2<sup>+</sup> tumor cells.

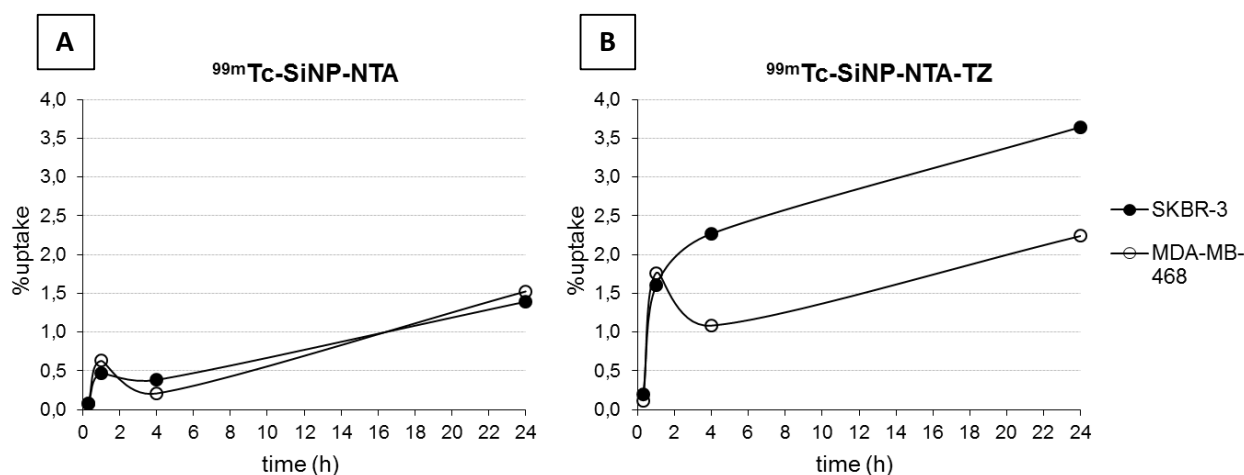


**Figure 2.7** Specificity binding by fluorescence microscopy. SK-BR-3 and MDA-MB-468 cells were grown on coverslips for 24 h and then exposed for 1, 4, 24 h to  $50 \mu\text{g mL}^{-1}$  of FITC-labeled (green) SNPs functionalized with (SiNP-NTA-TZ) or without (SiNP-NTA) Hc-TZ. Nuclei were stained with Hoechst (blue). Scale bar:  $50 \mu\text{m}$ .



**Figure 2.8** Specificity binding by fluorescence microscopy. SK-BR-3 and MDA-MB-468 cells were grown on coverslips for 24 h and then exposed for 1, 4, 24 h to  $50 \mu\text{g mL}^{-1}$  of FITC-labeled (green) SiNP-TZ. Nuclei were stained with Hoechst (blue). Scale bar:  $50 \mu\text{m}$ .

After the radiolabeling process, the binding capacity of SiNP-NTA and SiNP-NTA-TZ was corroborated by  $\gamma$ -counter: HER2<sup>+</sup> and HER2<sup>-</sup> cells (SK-BR-3 and MDA-MB-468 respectively) were incubated with each nanoconjugate and, at selected time points, <sup>99m</sup>Tc radioactivity was quantified both in the excluded media and inside the cells. NPs uptake was then presented as % of total radioactivity administered. SiNP-NTA were internalized weakly and nonspecifically both in MDA-MB-468 and SK-BR-3 cells, the maximum value of uptake being 1.4%, reached at 24 h after incubation (Figure 2.9, A). In contrast, SiNP-NTA-TZ showed an uptake value of 1.6% in SK-BR-3 cells already after 1 h of incubation, reaching 2.3% at 4 h, compared to 1.1% of uptake observed in MDA-MB-468 cells ( $p < 0.05$ ). It is apparent that the specific uptake ratio [SK-BR-3/MDA-MB-468] for SiNP-NTA-TZ was maximum at this time point. The uptake of SiNP-NTA-TZ continued to increase up to 24 h showing a slight increase in both cell lines, following a similar nonspecific trend, and reaching an uptake value of 3.7% in HER2<sup>+</sup> cells and 2.1% in HER2<sup>-</sup> cells (Figure 2.9, B).



**Figure 2.9** *In vitro* uptake of <sup>99m</sup>Tc-radiolabeled A) SiNP-NTA and B) SiNP-NTA-TZ NPs. SK-BR-3 and MDA-MB-468 cells were incubated with SNPs (1  $\mu$ Ci mL<sup>-1</sup>) for 1, 4, 24 h. Cell uptake was expressed as % of total radioactivity administered. (Student's *t*-test; \* $p < 0.05$  vs. MDA-MB-468).

#### 2.5.4 – *Ex vivo* biodistribution and fluorescent imaging

Biodistribution pattern of <sup>99m</sup>Tc-labeled NPs (SiNP-NTA and SiNP-NTA-TZ) was assessed in a SK-BR-3 tumor mouse model by detecting the radioactivity accumulation at different time points (Figure 2.10). At 4 h post injection (p.i.), radioactivity accumulation in tumor was higher for Hc-TZ-conjugated NPs compared to nontargeted NPs. At this time mean tumor uptake (expressed as % ID/g) was  $0.52 \pm 0.08$  for SiNP-NTA and  $0.67 \pm 0.03$  for SiNP-NTA-TZ, and tumor-to-muscle

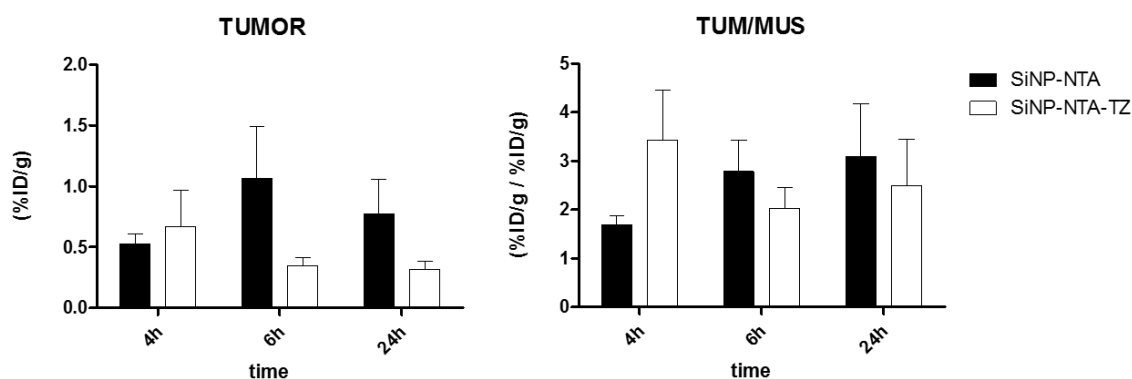


ratios (expressed as tumor/muscle ratio of % ID/g) for SiNP-NTA and SiNP-NTA-TZ were  $1.69 \pm 0.18$  and  $3.453 \pm 1.02$ , respectively. At longer times of exposure, we observed a reduction in tumor radioactivity concentration for animals injected with SiNP-NTA-TZ but not in those injected with SiNP-NTA. The decline of SiNP-NTA-TZ uptake value, observed from 6 h p.i., could be explained by an active targeting followed by lysosomal degradation and consequent clearance of NPs. The corresponding enhancement in the uptake of SiNP-NTA suggests passive targeting promoted by tumor enhanced permeability and retention (EPR) effect. Considering the other organs, high levels of radioactivity were observed in liver, kidney and spleen for both NPs (Table 2.3). For the whole experimental time course, the radioactivity concentration in kidney was significantly higher in mice injected with SiNP-NTA than in those injected with SiNP-NTA-TZ. Low and similar levels of radioactivity were detected in lungs.

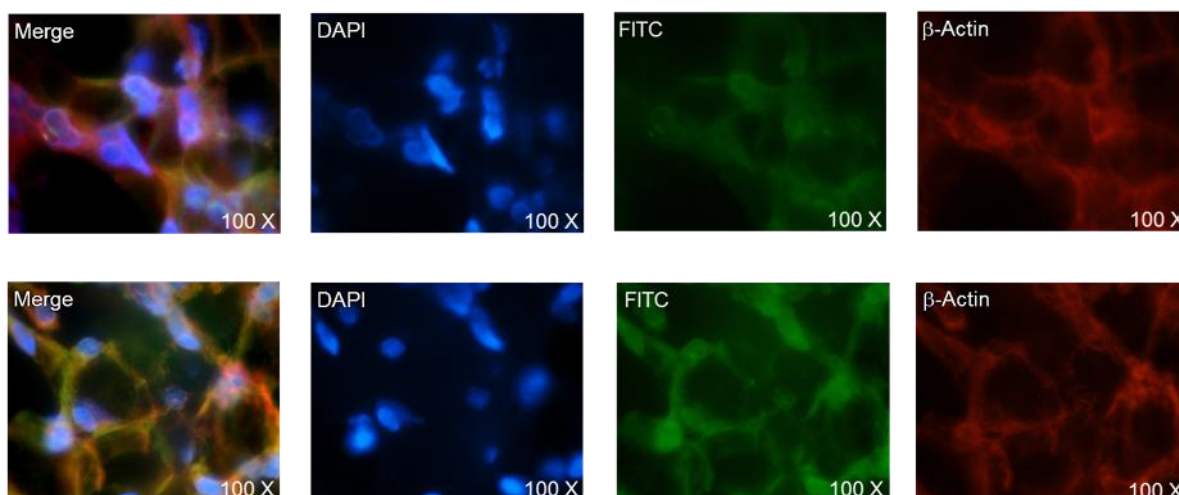
**Table 2.3** Radioactivity distribution after  $^{99m}\text{Tc}$ -labeled SiNP-NTA or SiNP-NTA-TZ injection. Radioactivity concentration is expressed as percentage of injected dose per gram of tissue (% ID/g). Values are expressed as mean  $\pm$  S.D. of three rats for each time point. (\*p < 0.05 vs. SiNP-NTA)

Tissue	%ID/g at 4 h p.i.		%ID/g at 6 h p.i.		%ID/g at 24 h p.i.	
	(n=3)		(n=3)		(n=4)	
	SiNP-NTA	SiNP-NTA-TZ	SiNP-NTA	SiNP-NTA-TZ	SiNP-NTA	SiNP-NTA-TZ
Blood	0.84 $\pm$ 0.14	1.27 $\pm$ 0.24	0.88 $\pm$ 0.21	1.05 $\pm$ 0.15	0.43 $\pm$ 0.06	0.52 $\pm$ 0.11
Heart	0.32 $\pm$ 0.07	0.44 $\pm$ 0.01	0.46 $\pm$ 0.13	0.33 $\pm$ 0.13	0.22 $\pm$ 0.02	0.99 $\pm$ 1.53
Lung	0.89 $\pm$ 0.13	2.31 $\pm$ 0.79	1.09 $\pm$ 0.12	1.38 $\pm$ 0.64	0.47 $\pm$ 0.07	0.35 $\pm$ 1.28
Liver	58.6 $\pm$ 10.9	36.3 $\pm$ 7.13*	44.6 $\pm$ 34.9	13.2 $\pm$ 11.7	7.83 $\pm$ 2.08	9.14 $\pm$ 5.34
Spleen	6.48 $\pm$ 0.49	6.96 $\pm$ 1.00	4.98 $\pm$ 4.68	2.62 $\pm$ 3.68	0.82 $\pm$ 0.20	2.42 $\pm$ 1.89
Stomach	0.44 $\pm$ 0.17	0.46 $\pm$ 0.28	0.52 $\pm$ 0.21	0.42 $\pm$ 0.16	0.33 $\pm$ 0.05	0.25 $\pm$ 0.12
Kidney	13.3 $\pm$ 1.55	5.52 $\pm$ 0.04*	51.6 $\pm$ 59.8	6.83 $\pm$ 1.36	14.3 $\pm$ 2.02	5.19 $\pm$ 1.57*
Intestine	0.72 $\pm$ 0.18	1.44 $\pm$ 0.88	1.99 $\pm$ 1.22	0.43 $\pm$ 0.17	0.35 $\pm$ 0.07	0.26 $\pm$ 0.06
Tumor	0.52 $\pm$ 0.08	0.67 $\pm$ 0.30	1.06 $\pm$ 0.43	0.35 $\pm$ 0.07	0.77 $\pm$ 0.28	0.32 $\pm$ 0.07
Tiroyd	0.53 $\pm$ 0.11	0.67 $\pm$ 0.19	0.54 $\pm$ 0.12	0.44 $\pm$ 0.08	0.40 $\pm$ 0.09	0.35 $\pm$ 0.11
Muscle	0.31 $\pm$ 0.02	0.19 $\pm$ 0.03*	0.38 $\pm$ 0.29	0.18 $\pm$ 0.05	0.26 $\pm$ 0.08	0.13 $\pm$ 0.03

The targeting specificity of  $^{99m}\text{Tc}$ -labeled NPs in SK-BR-3 lesions was also assessed by fluorescence microscopy. Immunofluorescence staining of tumor cryosections collected at 4 h p.i. allowed us to establish the distribution of the two nanotracers (Figure 2.11). Images of SNPs (green) and  $\beta$ -actin (red) were overlaid on the corresponding images reporting nuclei (blue). Fluorescence intensity in SiNP-NTA-TZ images was significantly higher than that from SiNP-NTA and it was highly colocalized in the perinuclear area. In contrast, green fluorescence distribution in SiNP-NTA images was barely detectable on the surface of SK-BR-3 tumor cell membrane.



**Figure 2.10** *Ex vivo* biodistribution of  $^{99m}\text{Tc}$ -labeled SiNP-NTA and SiNP-NTA-TZ NPs. SK-BR-3 tumor bearing mice were sacrificed at 4, 6, 24 h post-injection (n= 3). Samples were dissected and analyzed by  $\gamma$ -counter to obtain tumor-to-muscle ratio of % ID/g (on the right) and the tumor absolute values (on the left).



**Figure 2.11** *Ex vivo* immunofluorescence of SK-BR-3 tumor cryosections collected at 4 h post-injection of SiNP-NTA (top) and SiNP-NTA-TZ (bottom). Merge images represent the colocalization of SNPs (green),  $\beta$ -actin (red) and reporting nuclei (blue).

## 2.6 – Conclusions

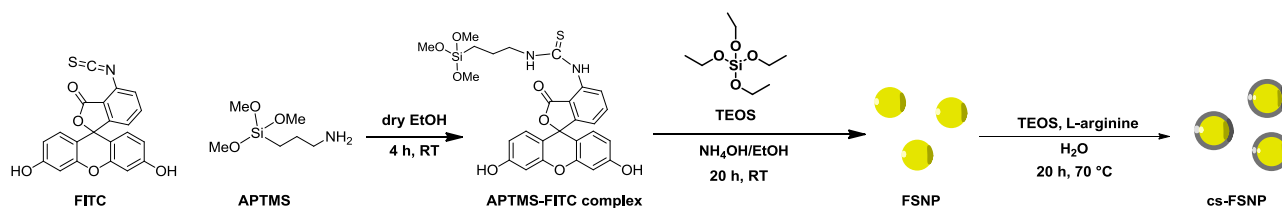
In the first part of the project, aimed at developing a theranostic agent for the targeted detection and treatment of HER2<sup>+</sup> breast cancer, we designed and tested  $^{99m}\text{Tc}$ -radiolabeled SNPs functionalized with Hc-TZ to be used as SPECT radiotracers. In our study, we compared the behavior and the targeting efficiency of SNPs functionalized or not with Hc-TZ in BCs models *in vitro* and *in vivo*, before and after radiolabeling. Although well established protocols to radiolabel antibodies are reported in the literature [43], we preferred to develop a new approach based on

direct immobilization of radioligand to the NP surface to obtain a radiolabeled scaffold common to the different nanoconstructs synthesized within this study, independent from the functionalization with the antibody chain. Radiolabeling of both SiNP-NTA and SiNP-NTA-TZ was achieved by formation of  $^{99m}\text{Tc}$ -NTA complex. Our results, both *in vitro* and *in vivo*, suggest that receptor-mediated active targeting provided the best efficiency in BC detection, compared to simple EPR passive accumulation. *In vitro* flow cytometry data showed a remarkable increase in uptake over time after incubation of SiNP-TZ/SiNP-NTA-TZ in HER2<sup>+</sup> SK-BR-3 cells, compared to SiNP/SiNP-NTA. As expected, the uptake of all SNPs tested remained low in HER2<sup>-</sup> MDA-MB-468 cells. These results were confirmed by fluorescence imaging experiments, which exhibited a considerable perinuclear localization in SK-BR-3 cells exclusively upon incubation with SiNP-TZ/SiNP-NTA-TZ, while an external localization of fluorescence signal was observed in MDA-MB-468 cells with both SiNP-TZ/SiNP-NTA-TZ and SiNP/SiNP-NTA. The same results were obtained for radiolabeled nanoconjugates, suggesting that our radiolabeling strategy did not affect the nanoconjugate binding capability. Next, the radiolabeled SNPs efficiency in detecting HER2<sup>+</sup> cells was evaluated in a SK-BR-3 xenograft animal model. *Ex vivo* biodistribution of  $^{99m}\text{Tc}$ -SiNP-NTA-TZ showed a preferential intracellular distribution at 4 h p.i. compared to  $^{99m}\text{Tc}$ -SiNP-NTA, confirming the involvement of Hc-TZ functionalization in the targeting efficiency of the nanoconstruct compared to EPR passive accumulation. In addition,  $^{99m}\text{Tc}$ -SiNP-NTA-TZ cell selectivity observed at 4 h was confirmed by fluorescence imaging of tumor cryosections, showing a specific intracellular localization compared to  $^{99m}\text{Tc}$ -SiNP-NTA.

In summary, our radiolabeled system not only exhibited an enhanced targeting for the tumor, compared to EPR passive diffusion, but also significantly increased the selective accumulation of SNPs within the HER2<sup>+</sup> SK-BR-3 cells, taking advantage of an optimized conjugation to the half-chain fragment of the humanized antibody trastuzumab, already in use in the clinical practice.

## 2.7 – Experimental section

### 2.7.1 – Synthesis of fluorescent core-shell silica nanoparticles



#### 2.7.1.1 – Synthesis of N-1-(3-trimethoxysilylpropyl)-N'-fluoresceyl thiourea (APTMS-FITC complex)

FITC (2 mg, 5.0  $\mu\text{mol}$ ) was dissolved in dry ethanol (2 mL) and APTMS (10.0  $\mu\text{L}$ , 55.0  $\mu\text{mol}$ ) was rapidly added to this solution. The reaction was left under stirring 4 h at room temperature (RT) in darkness. The reaction was monitored by <sup>1</sup>H-NMR (CD<sub>3</sub>OD) and the complex was used without further purifications.

#### 2.7.1.2 – Synthesis of fluorescent core silica nanoparticles (FSNP)

Monodisperse fluorescent silica nanospheres were obtained by a slightly modified Stöber synthesis. Briefly, to a NH<sub>4</sub>OH solution in water (1.827 g, 0.58 M) dry ethanol was added to reach a final volume of 50 mL and the mixture was equilibrated under magnetic stirring for 10 min. To the above solution, TEOS (1.990 mL, 0.17 M) and APTMS-FITC complex (1 mL) were rapidly added in sequence and the reaction was stirred for 20 h at RT in darkness. The solvent was then evaporated under reduced pressure by half of its volume (25 mL) and deionized water was added (40 mL). The remaining organic solvent was completely evaporated under reduced pressure to give an aqueous suspension of FSNP. Then the suspension was filtered on a cotton filter to remove big aggregates, while unreacted species were removed by high-speed centrifugation (20000 rcf, 20 min) and resuspension in ultrapure water (40 mL) three times. The final volume was then adjusted to give a NP concentration of 10 mg mL<sup>-1</sup> (concentration determined by drying 1 mL of NPs suspension at 100 °C, 3 h).

#### 2.7.1.3 – Synthesis of core-shell fluorescent silica nanoparticles (cs-FSNP)

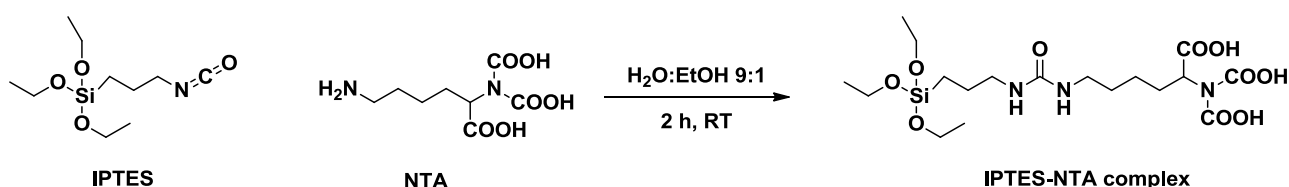
A silica shell of 5 nm thickness was added around FSNP according to biosilicification methods reported in the literature [39]. To a clean aqueous suspension of FSNP (10 mg mL<sup>-1</sup>) L-arginine (0.5 mg mL<sup>-1</sup>) was added and the solution was equilibrated to 70 °C for 10 min. Next, TEOS (quantity

estimated by equation 1) was slowly added and the reaction was left under mild stirring at 70 °C overnight in the darkness. The resulting cs-FSNP were washed thrice (20000 rcf, 20 min) and redispersed with ultrapure water to give a final concentration of 10 mg mL<sup>-1</sup>.

$$(1) \quad m_{TEOS} = d_{SiO_2} \cdot (V_{core-shell} - V_{core}) = \frac{4}{3} \pi d_{SiO_2} (r_{core-shell} - r_{core})^3$$

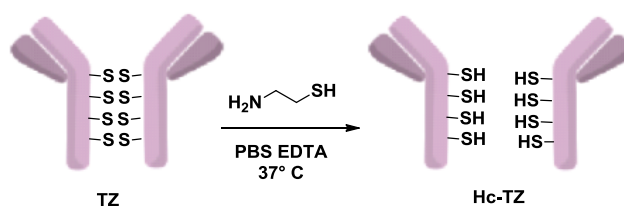
## 2.7.2 – Synthesis of SiNP, SiNP-TZ, SiNP-NTA and SiNP-NTA-TZ

### 2.7.2.1 – Synthesis of IPTES-NTA complex



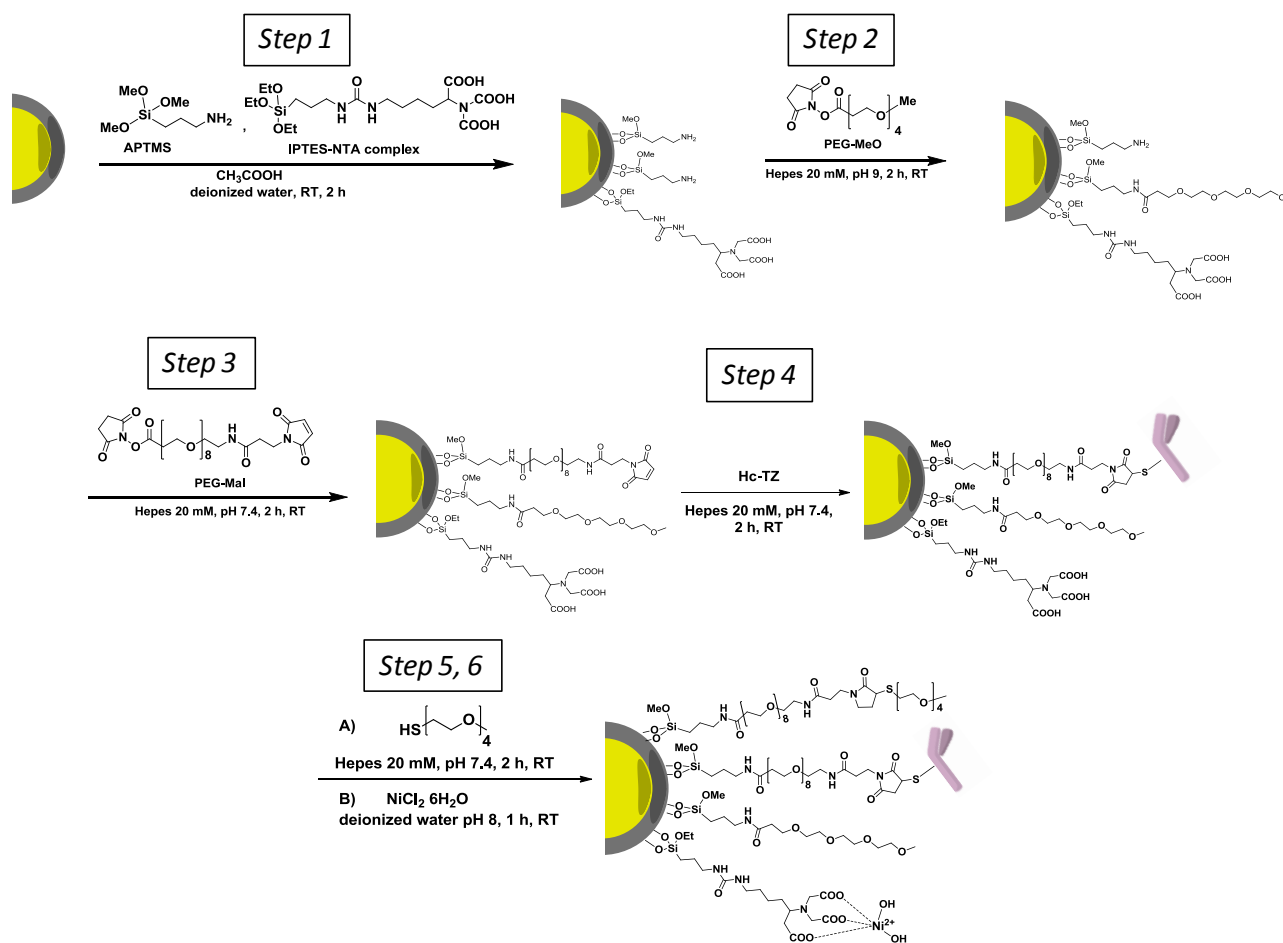
The complex between (3-isocyanatopropyl)triethoxysilane (IPTES, 2 μL) and *Nα,Nα*-Bis(carboxymethyl)-L-lysine (NTA, 2 mg) were mixed in 200 μL of a mixture of deionized water:ethanol 9:1. The reaction was left under stirring for 2 h, at RT and the complex was used immediately after preparation.

### 2.7.2.2 – Preparation of trastuzumab half-chain (Hc-TZ)



Cysteamine (28 mM) was dissolved in a reaction buffer (20 mM Hepes, 5 mM EDTA, pH 7.2, 1 mL) and dialyzed trastuzumab (1 mg) dissolved in PBS, pH 7.2, was added. The solution was incubated under gentle stirring at 37 °C for 90 min. The reaction was cooled to RT and purified using a Sephadex-containing PD10 column (GE Healthcare Life Science). Hc-TZ was collected (0.285 mg mL<sup>-1</sup>) in 20 mM Hepes buffer, pH 7.4 and used immediately after purification.

### 2.7.2.3 – Complete functionalization of cs-FSNP (SiNP-NTA-TZ)



*Step 1. Amination and IPTES-NTA conjugation to cs-FSNPs.* To a desired amount of cs-FSNPs, glacial acetic acid (5.25  $\mu\text{mol}$  per mg of NPs), IPTES-NTA complex (4 nmol per mg of NPs) and APTMS (1.72  $\mu\text{mol}$  per mg of NPs) were added in sequence. The mixture got turbid and was left in ultrasound bath until clearness. The reaction was then vigorously stirred for 2 h, after which the aminated NPs were washed thrice with ultrapure water and twice with 20 mM Hepes buffer, pH 9, and redispersed in the same buffer (10 mg mL<sup>-1</sup>) for further functionalization.

*Step 2. Introduction of PEG-OMe.* To the NPs suspension in Hepes, methyl-tetraethylenglycol-*N*-hydroxysuccinimide (MS(PEG)<sub>4</sub>, Thermo Fisher Scientific) was added in an equimolar amount with respect to the surface amine functionalities assessed by ninhydrin assay (view paragraph 2.7.3). The reaction was left under stirring 2 h, after which the NPs were washed (20000 rcf, 20 min) twice with ultrapure water and twice with 20 mM Hepes buffer, pH 7.4, and redispersed in the same buffer for next steps.

*Step 3. Introduction of PEG-Mal.* Maleimidopropionamido-octylethyleneglycol-*N*-hydroxysuccinimide (SM(PEG)<sub>8</sub>, Thermo Fisher Scientific) was added to the NPs suspension in a 5-fold molar excess with respect to the unreacted surface amine functionalities assessed by ninhydrin assay. The reaction was left under stirring 2 h, after which the NPs were washed once with ultrapure water and then redispersed in 20 mM Hepes buffer, pH 7.4.

*Step 4. Hc-TZ coupling.* To the NPs suspension, the previously prepared Hc-TZ was added (10 µg mg<sup>-1</sup> of NPs) and the reaction was left under gentle stirring for 2 h. After the reaction, the NPs were washed (16000 rcf, 20 min, 4 °C) once with 20 mM Hepes, pH 7.4 and resuspended in the same buffer.

*Step 5. Saturation of free maleimido-groups.* To the NPs suspension, Methyl-tetraethylenglycol-thiol (MT(PEG)<sub>4</sub>, Thermo Fisher Scientific, 0.5 µg per mg of NPs) was added and the reaction was left under stirring 1 h, after which the NPs were washed (16000 rcf, 20 min, 4 °C) thrice with 20 mM Hepes, pH 7.4 and resuspended in 1 mM NiCl<sub>2</sub>, pH 8.

*Step 6. Nickel chelation to NTA.* The NPs were incubated under stirring in the NiCl<sub>2</sub> buffer for 1 h, and then washed (16000 rcf, 20 min, 4 °C) twice with 20 mM Hepes pH 7.4 and resuspended in the same buffer.

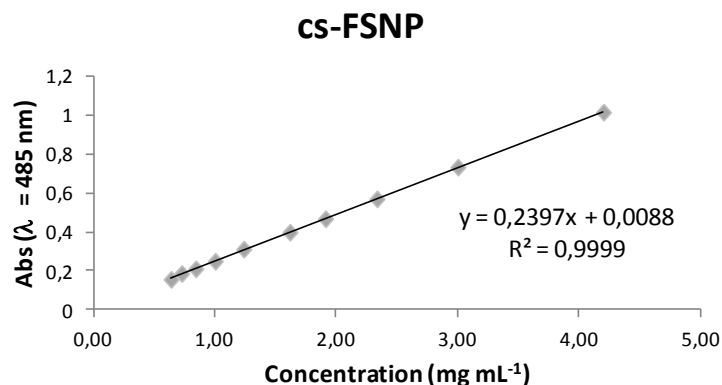
#### 2.7.2.4 – Partial functionalization of cs-FSNP (SiNP, SiNP-TZ, SiNP-NTA)

The other NPs used in this study were synthesized as described in the previous paragraph, avoiding some steps: in particular, the conjugation of IPTES-NTA, step 4 and step 6 for SiNP, the conjugation of IPTES-NTA and step 6 for SiNP-TZ, step 4 for SiNP-NTA.

#### **2.7.3 – Determination of amino groups: ninhydrin assay**

Our protocol was adapted from a standard method described in the literature [49]. Briefly, aminated SNPs (3 mg) were equilibrated twice in dry ethanol and then resuspended in 400 µL of the same solvent. Meanwhile a ninhydrin stock solution 4 mg mL<sup>-1</sup> was prepared in dry ethanol obtaining a clear pale green solution. 100 µL of ninhydrin stock solution was then added to the NPs suspension and the mixture was heated at 60 °C for 1 h. After cooling to RT, NPs were separated from the supernatant by centrifugation (20000 rcf, 20 min) and an aliquot of the particle-free blue supernatant read with UV-Vis spectrophotometer at 570 nm. A standard calibration curve was created using ethanolamine in a concentration range between 0–3 mM in dry ethanol.

#### 2.7.4 – Determination of functionalized NP concentration



At the end of each functionalization step NP concentration was checked by means of UV-visible analysis. A reference calibration curve was created as follow: 1 mL of cs-FSNP was dried in oven at 100 °C for 3 h and the resulting fine solid was weighted providing NP concentration in mg mL<sup>-1</sup>. This way stock solutions of cs-FSNP at different concentrations were prepared by appropriate dilutions and each sample was analyzed by UV-vis spectroscopy, correlating FITC absorption peak at  $\lambda = 485$  nm to NP concentration. A new calibration curve was prepared for each new batch of cs-FSNP synthesized. After each functionalization step, the concentration of SNP suspensions could be determined by UV-vis analysis and interpolation of the result in the calibration curve.

#### 2.7.5 – SNP characterization

DLS measurements were performed with Zetasizer Nano ZS ZEN3600 (Malvern Instruments Ltd, Worcestershire, UK), equipped with a He-Ne laser ( $\lambda = 632.8$  nm) working at 4 mW. A disposable cuvette with an optical length of 1 cm was used and scattered light was collected at 173°. The samples were prepared with an average concentration of 100  $\mu\text{g mL}^{-1}$  in ultrapure water, and they were allowed to equilibrate at 25 °C for 30 s before the analysis. The Hd was derived using Stokes-Einstein equation, considering a viscosity of the medium of 0.8872 cP.  $\zeta$ -potential measurements were performed with the same instrument.  $\zeta$ -potential values were calculated by the Zetasizer Software basing on electrophoretic mobility and considering a viscosity of 0.8872 cP, dielectric constant of 78.5 and a Henry's function of 1.5. Samples were prepared with an average concentration of 100  $\mu\text{g mL}^{-1}$  in 1 mM NaCl (pH 7) and they were allowed to equilibrate at 25 °C for 30 s before the analysis. TEM images of NPs were obtained on a "FEI Tecnai G" Spirit BioTWIN microscope (Hillsboro, OR) operating at 120 kV. The



samples were prepared by evaporating 2  $\mu\text{L}$  of NPs (generally 50  $\mu\text{g mL}^{-1}$ ) onto carbon-coated copper grid (200 mesh) and allowing it to dry on the air. The average particle diameter were obtained by measuring at least 100 particles by using imageJ software (National Institute of Health, USA).

## **2.7.6 – Radiolabeling of SiNP-NTA and SiNP-NTA-TZ**

### 2.7.6.1 – Preparation of $^{99\text{m}}\text{Tc}(\text{CO})_3]^+$

The labeling precursor ( $^{99\text{m}}\text{Tc}(\text{H}_2\text{O})_3(\text{CO})_3]^+$ ) was prepared using the Isolink kit (Paul Scherrer Institute-Switzerland) containing 8.5 mg sodium tartrate, 2.85 mg sodium tetraborate decahydrate, 7.15 mg of sodium carbonate and 4.5 mg sodium boranocarbonate. Freshly eluted  $^{99\text{m}}\text{TcO}_4^-$  from a commercial General Electric generator (approximately 2 GBq) in 1 mL saline buffer was added to the kit vial and incubated at 100  $^\circ\text{C}$  for 20 min. The vial was then cooled to RT and the solution neutralized by adding stepwise 1 M HCl. The radiochemical purity (RCP) of the product was analyzed by HPLC and was up 95%.

### 2.7.6.2 – $^{99\text{m}}\text{Tc}(\text{CO})_3]^+$ -His-Tag prelabeling

An hexa-His-Tag peptide was prelabeled with  $^{99\text{m}}\text{Tc}(\text{CO})_3]^+$  by mixing 38  $\mu\text{L}$  of peptide solution (5 mg  $\text{mL}^{-1}$  in Hepes buffer pH 7.4) with the  $^{99\text{m}}\text{Tc}(\text{CO})_3(\text{OH}_2)_3]^+$  precursor solution. The solution was left at RT under stirring for 60 min and then the % RCP was checked. The labeling yield was assessed by HPLC and the reaction resulted almost quantitative. Radiochemical purity was 95%.

### 2.7.6.3 – Conjugation of $^{99\text{m}}\text{Tc}(\text{CO})_3]^+$ -His-Tag to SiNP-NTA and SiNP-NTA-TZ

The  $^{99\text{m}}\text{Tc}(\text{CO})_3]^+$ -His-Tag solution was added to 500  $\mu\text{L}$  of NPs (4 nmol NTA per mg of SNPs). The solution mixture was left at RT under stirring for 2.5 h and then the % RCP was checked. The solution was shaken for about 1 min over a vortex mixer and then centrifuged for 15 min at 18000 rpm. Supernatant solution was withdrawn and the corresponding radioactivity was counted. The pellet was washed with Hepes buffer and centrifuged three times. After the measurement of radioactivity of total supernatant and pellet the %RCP was 42% for SiNP-NTA and 23.8% for SiNP-NTA-TZ.

### 2.7.6.4 – Quality control

The chemical and radiochemical purity of each reaction intermediate was performed using a HPLC Akta system equipped with radiochemical flow counter (Bioscan). For HPLC analysis of the

radiolabeled  $^{99m}\text{Tc}$ -tricarbonyl core and  $^{99m}\text{Tc}$ -tricarbonyl-hexa-His peptide a Thermo Scientific BDS reverse-phase column ( $250 \times 4.6$ ) was used with a flow of  $1.2 \text{ mL min}^{-1}$  and a linear triphasic gradient of 2% B (MeOH) with A (0.1% TFA) from 0 to 10', 2% C ( $\text{CH}_3\text{CN}$  50% + 0.1% TFA) with A from 10 to 18'. Absorbance was detected at 220 nm. The radiochemical purity of the [ $^{99m}\text{Tc}$ ]- $(\text{CO})_3$ -SNPs was determined by ascending instant thin-layer chromatography (ITLC) with silica gel-coated fiberglass sheets (Pall Life Sciences, Pall Corporation) using physiological saline as the mobile phase.

### **2.7.7 – Cell culture and animal models**

All reagents and solvents were purchased from Sigma-Aldrich (St. Louis, MO) and Invitrogen Corp (Carlsbad, CA). Cell lines were obtained from ICLC Animal Cell Lines Database - IST Genova (IT). MDA-MB-468 and SK-BR-3 cells were maintained in Dulbecco's Modified Eagles Medium (DMEM), high glucose, supplemented with 5% Pen/Strep, 10% heat-inactivated fetal bovine serum and 2 mM L-glutamine. MCF-10A cells were maintained in Ham's F-12:Dulbecco's Modified Eagles Medium (DMEM; 50:50), high glucose, supplemented with 5% Pen/Strep, 10% heat-inactivated horse serum and 2 mM L-glutamine. Female Balb/c nude mice were obtained from the ENVIGO RMS S.R.L. Italy. Animal experiments were carried out in compliance with the institutional guidelines for the care and use of experimental animals (IACUC), which have been notified to the Italian Ministry of Health and approved by the Ethics Committee of the San Raffaele Scientific Institute (Milan, Italy). Female Balb/c nude mice with the age of 7–8 weeks and weight of 24–26 g were maintained under specific pathogen free condition. To obtain SK-BR-3 tumor models, about  $5 \times 10^6$  cells in 200  $\mu\text{L}$  mixed solution (serum-free RMPI-1640 medium and matrigel at the volume ratio of 1:1) were injected under the right shoulder. Calipers were used to measure tumor volume ( $\text{mm}^3$ ) twice per week and mice weight was recorded. Mice were randomized when tumor volumes reached an average of 100  $\text{mm}^3$ .

### **2.7.8 – Cell uptake assays**

#### 2.7.8.1 – Flow cytometry of non-radiolabeled SNPs

SK-BR-3 cells ( $\text{HER2}^+$ ,  $3 \times 10^5$ ) were incubated with  $0.5 \mu\text{g mL}^{-1}$  of either SiNP, SiNP-TZ, SiNP-NTA or SiNP-NTA-TZ dispersed in serum free-DMEM. After different incubation times (20 min, 1 h, 4 h, 24 h), cells were washed twice with PBS and harvested in FACS tubes.  $10^5$  events were acquired for each analysis on FACS Calibur flow cytometer (Becton Dickinson) exploiting FITC emission (green fluorescence). Both the percentage of the fluorescent cells relative to the

control (untreated cells) and the mean fluorescent intensity of the fluorescence-positive cells were taken into account. The same experiment was performed with MDA-MB-468 cell line (HER2<sup>-</sup>) as a negative control. The results were analyzed using FlowJo software.

#### 2.7.8.2 – Fluorescence microscopy of non-radiolabeled SNPs

SK-BR-3 (HER2<sup>+</sup>,  $5 \times 10^4$ ) and MDA-MB-468 (HER2<sup>-</sup>,  $5 \times 10^4$ ) cells were incubated with 1 mg mL<sup>-1</sup> of either SiNP, SiNP-TZ, SiNP-NTA or SiNP-NTA-TZ dispersed in cell culture media. After 20 min, 1 h, 4 h and 24 h of incubation at 37 °C (humidified atmosphere, 5% CO<sub>2</sub> air), the medium was removed and cells were washed three times with PBS. The samples were fixed with methanol (at -20 °C for 30 min) before the acquisition. The specific uptake of SNPs in both cell lines was evaluated by fluorescence microscopy (Nikon Eclipse 80i).

#### 2.7.8.3 – *In vitro* uptake of radiolabeled SNPs

SK-BR-3 (HER2<sup>+</sup>,  $5 \times 10^4$ ) and MDA-MB-468 (HER2<sup>-</sup>,  $5 \times 10^4$ ) cells were incubated with 1 μCi mL<sup>-1</sup> of either <sup>99m</sup>Tc-labeled SiNP-NTA or SiNP-NTA-TZ dispersed in cell culture media. After 1 h, 4 h and 24 h of incubation at 37 °C (humidified atmosphere, 5% CO<sub>2</sub> air), the medium was removed and cells were washed three times with PBS. The cells were extracted with 200 μL of 0.05% Trypsin-EDTA (1×) solution for 10 minutes. The radioactivity of the cells and of each removed solution were then measured using a γ-counter (LKB Compugamma CS 1282). The percentage of radioactivity in cells over the total radioactivity for each plate was calculated.

#### **2.7.9 – *In vitro* cytotoxicity assay**

*In vitro* cytotoxicity of SNPs was tested on SK-BR-3 (HER2<sup>+</sup>), MDA-MB-468 (HER<sup>-</sup>) and MCF10A (non-transformed mammary epithelial) lines through MTT assay, and by viable cell counting on HER2<sup>+</sup> and HER<sup>-</sup> cell lines. For the MTT test, both cell lines were seeded in 96-well plates (Corning, USA) at a density of  $5 \times 10^3$  cells per well and incubated for 48 h. The suspensions of SiNP, SiNP-TZ, SiNP-NTA or SiNP-NTA-TZ were diluted in culture medium at 50 μg mL<sup>-1</sup>. The cell culture medium was then removed and replaced by 100 μL of fresh medium containing NPs. The cells were incubated for 1 h, 4 h, 24 h and 48 h at 37 °C in a humidified atmosphere, 5% CO<sub>2</sub> air. After the above times, medium was removed and 100 μL of MTT (5 mg mL<sup>-1</sup> in PBS) was added to each well. After 3 h, the culture medium containing MTT solution was removed. 100 μL of SDS in 0.01 M HCl solution was added to each well to dissolve the formazan crystals and then plates were analyzed using a microplate reader

(SPECTROstar Omega - BMG LABTECH) at 570 nm. For the viable cell counting experiments, NPs were incubated as described for MTT test. The medium was removed from the samples and the cells were suspended in PBS 0.1 M ( $5 \times 10^5$  cells/mL). 10  $\mu$ L of 0.4% Trypan blue was incubated for 3 min with the cell suspension (1:1), and then the mix was loaded on the Thoma chamber BLAUBRAND (Sigma-Aldrich, Italy) for the counting of the unstained (viable) and stained (nonviable) cells. Cell viability was expressed in both experiments by comparing the treated samples to cells incubated with normal culture medium considered as 100% survival rate [% viability = (treated cells / control cells)  $\times$  100].

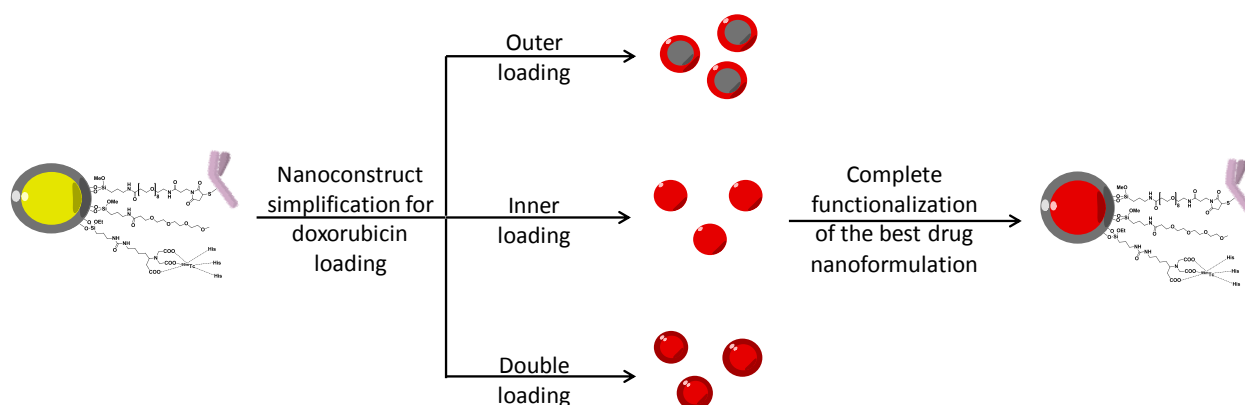
#### **2.7.10 – *Ex vivo* biodistribution and fluorescence imaging of $^{99m}\text{Tc}$ -radiolabeled SNPs in tumor**

$^{99m}\text{Tc}$ -radiolabeled SNPs were evaluated in two experimental groups of Balb/c nude mice. Mice in both groups were anesthetized with Zoletil (25 mg  $\text{kg}^{-1}$  of body weight) injected intraperitoneal, with additional supplemental anesthetic as needed. Two groups of 12 mice were injected in a tail vein with 100  $\mu$ L of a solution containing  $^{99m}\text{Tc}$ -labeled SiNP-NTA-TZ or  $^{99m}\text{Tc}$ -labeled SiNP-NTA (1 mCi  $\text{mL}^{-1}$ , pH~7.4). Additional aliquot (0.1 mL) of both radioactive solution was diluted 1:10, 1:100 and 1:1000 and used to calculate the standards curve. Four animals per experimental point were sacrificed (at 4 h, 6 h and 24 h, post-injection) under general anesthesia. Tumor and a sample of muscle were removed and placed in counting vials for counting and weighing. Tissue samples and standards were placed in a  $\gamma$ -counter (LKB Compugamma CS 1282) and counts corrected for physical decay. The radioactivity concentration in tumor was calculated as percentage of injected dose per gram of tissue (%ID/g) and expressed as tumor to muscle ratio. After counting, tumors were fixed with 4% paraformaldehyde for 4 h and embedded in OCT mounting medium (Sakura Finetek, Torrance, CA), to prepare frozen sections. For immunofluorescent staining, tumor sections (10  $\mu$ m) were rinsed with PBS and blocked with 5% BSA for 60 min followed by incubation with primary antibody (rabbit anti- $\beta$ -Actin, diluted 1:50; Sigma Aldrich) overnight at 4  $^{\circ}\text{C}$ . The day after, tumor sections were washed for 5 min three times with PBS. Sections were then incubated with secondary antibody (Alexa Fluor488-labeled goat anti-rabbit IgG, diluted 1:200; Sigma Aldrich) for 60 min at RT. After a rinse with PBS, they were incubated with 4-6-diamidino-2-phenylindole (DAPI) for 5 min. Finally, sections were sealed with anti-fluorescence quenching agent (Beyotime) and observed by fluorescence microscopy (Nikon Eclipse 80i).

## (ii) Development of Doxorubicin-Loaded Nonporous Silica Nanoparticles

### 2.8 – Aim of the project

The multifunctional SNPs decorated with Hc-TZ and the radionuclide  $^{99m}\text{Tc}$  appeared a promising contrast agent for the selective detection of HER2 positive breast cancer; for this reason, we explored the possibility to further introduce doxorubicin, for the therapy of the same malignancy. SNPs were used as drug carriers mainly in their mesoporous form [2], while nonporous SNPs still remain a more challenging strategy to adopt when designing a drug delivery system. Tang and coworkers developed a drug silica nanoconjugates with narrow size distributions having the drug covalently joined in the interior of the NPs [45]. Depending on the covalent link between the drug and the silica matrix, the release profile ranges between 2 and several days. In the subsequent work they also assessed the importance of the size of the particles in tumor penetration, concluding that 50 nm nanoconjugates were more effective than the bigger ones [46]. In another recent work, stimuli responsive linker were inserted into the silica matrix to release drug specifically inside the cells, in the presence of certain triggering factors, such as pH or glutathione concentration [47]. Although some interesting results were obtained, a systematic study on the correlation between silica NP degradation, cargo loading and delivery is still missing in the literature and thus the use of nonporous SNPs as drug delivery system remains almost unexplored. However, due to the great potential of this class of colloidal nanoprobe in diagnostics, the development of straightforward yet efficient and reliable synthetic strategies leading to their application as drug delivery system is highly expected by the scientific community.



**Figure 2.12** Graphical representation of the project evolution: the multifunctional silica nanovector presented in the first project was selected to be loaded with the anthracycline drug doxorubicin. Before building up the entire nanoconjugate, simpler doxorubicin silica nanoformulations were evaluated for their release capacity. Best nanoformulation will be then completely engineered.

Hence, we decided to divide our second project into two steps: first we simplified our nanoconstruct to first designate the best strategy to convert nonporous SNPs in efficient delivery systems; afterwards, the best nanoformulated drug will be decorated with all the functional moieties discussed in the first project. For the first purpose we evaluated three different doxorubicin nanoformulations, having in common a covalent link between the drug and the silica matrix (Figure 2.12). In one case, the drug was grafted only on the outer surface of SNPs (OuterDox SNPs), in a second one, it was encapsulated in the inner core (InnerDox SNPs) and in the last nanosystem, doxorubicin was both incorporated inside and grafted outside the nanocarrier (DoubleDox SNPs). After optimizing the synthetic procedures, all the SNPs were analyzed in terms of silica degradation and drug release and then the cytotoxic activity was assayed in cell cultures.

## 2.9 – Results and discussion

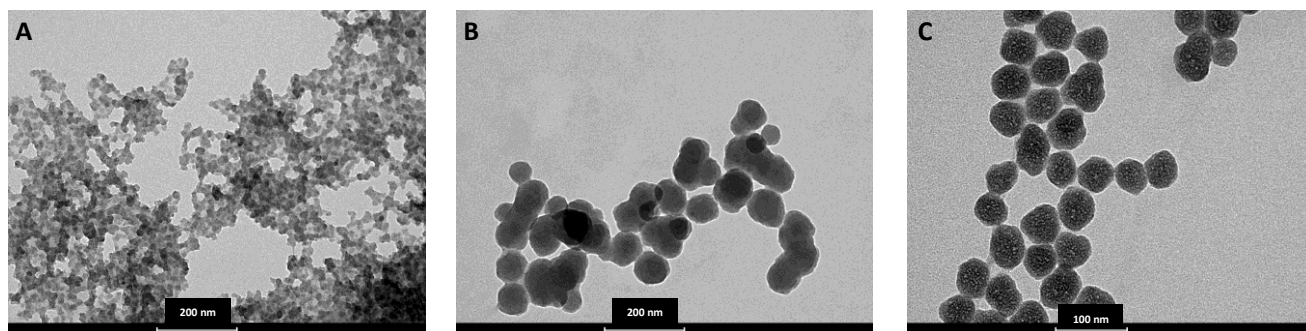
### 2.9.1 – Synthesis of doxorubicin-loaded SNPs

Although some works in the literature report the encapsulation of molecules inside the silica matrix of SNPs without derivatization of such molecules [48], the resulting NPs appeared to be too “soft” for our purpose, with the risk to dissolve fast, which would make it difficult to them to reach the desired site of action. Thus, in all of the nanoformulations developed in this work, doxorubicin was first reacted with IPTES forming an urea bond. For what concerns the synthesis of OuterDox, IPTES-Dox complex was prepared in aqueous environment and then grafted on already-prepared Stöber SNPs by means of a base-driven condensation reaction, leading to a red uniform suspension.

**Table 2.4** Characterization of the doxorubicin nanoformulations before and after the PEGylation step. Data are the mean  $\pm$  standard deviation of at least three different NP batches.

SNPs	Hydrodynamic diameter (nm)	PDI	$\zeta$ -potential (mV)
OuterDox	75.53 $\pm$ 29.91	0.155 $\pm$ 0.062	-25.02 $\pm$ 7.34
OuterDox-PEG	58.95 $\pm$ 5.34	0.129 $\pm$ 0.041	-21.30 $\pm$ 6.86
InnerDox	41.31 $\pm$ 4.19	0.160 $\pm$ 0.003	-31.50 $\pm$ 10.65
InnerDox-PEG	47.73 $\pm$ 5.67	0.130 $\pm$ 0.060	-34.33 $\pm$ 6.09
DoubleDox	753.4 $\pm$ 301.9	0.356 $\pm$ 0.221	+10.73 $\pm$ 3.07
DoubleDox-PEG	50.94 $\pm$ 1.37	0.121 $\pm$ 0.021	-25.20 $\pm$ 9.40

DLS measurements of the formulation evidenced a slight colloidal instability, as indicated by the great standard deviation of the hydrodynamic diameter (Table 2.4). This instability was recovered introducing amine functionalities, which were later conjugated to a short methoxyl-terminating PEG. In the case of InnerDox preparation greater attention was needed. In order to incorporate IPTES-Dox complex in the core of the particles, the payload of interest had to be introduced directly during the Stöber synthesis. As explained before, the crucial parameter for the Stöber procedure to be successful is reactant concentration, including TEOS, ammonia and water concentrations; when the little volume of water containing IPTES-Dox was added to the reaction, big and irregular aggregates were formed (Figure 2.13 A). The shape of the particles ameliorated when methanol was used (Figure 2.13 B), but only when hydrophilic doxorubicin was deprotonated with triethylamine, extracted in organic solvent and reacted in ethanol with IPTES, the uniform spherical shape of Stöber SNPs was observed (Figure 2.13 C). InnerDox suspension demonstrated a narrow size distribution, a negative  $\zeta$ -potential and a good colloidal stability; by the way we added the same external decoration as for the OuterDox SNPs for *in vitro* experiment purposes, as explained in the following paragraphs (Table 2.4).

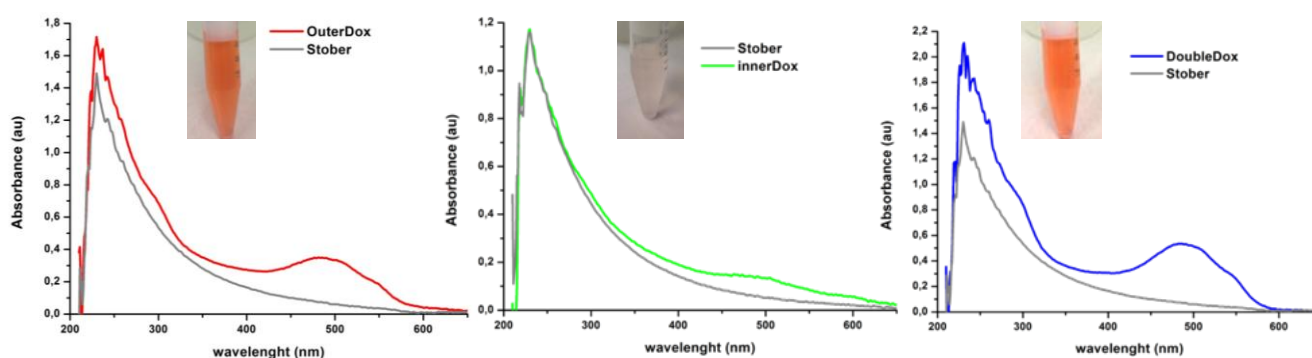


**Figure 2.13** TEM images of InnerDox SNPs during the protocol optimization. When IPTES-Dox complex was prepared in water (A) or methanol (B), SNPs appeared irregular and aggregated. When the complex was prepared in ethanol (C), SNPs showed the proper uniform spherical shape.

Finally, DoubleDox SNPs were prepared by grafting IPTES-Dox complex to the external surface of InnerDox. In this case, the hydrolysis/condensation of the silicate was promoted by an acidic environment: this choice was made in order to prevent the loss of doxorubicin during the reaction, as a rapid dissolution of the core of InnerDox was observed under basic pH (as discussed later). DoubleDox showed highly inconsistent results along the different DLS measurements, and an unusual positive  $\zeta$ -potential, possibly attributable to an acetic acid

adsorption on the silica surface. Nevertheless, the PEGylation step restored the stability and uniformity of SNPs suspension (Table 2.4).

After the preparation of doxorubicin-loaded SNPs, the drug content was determined by UV-Vis measurements directly on the NP suspensions; in fact, when the suspension concentration is kept below  $3 \text{ mg mL}^{-1}$ , the light diffusion of SNPs doesn't affect the absorption spectrum of doxorubicin (Figure 2.14). The measurements confirmed what was already apparent looking at the different SNPs: InnerDox NPs showed a reproducible drug loading in the range of 3-5 nmol of doxorubicin per mg of SNPs ( $\text{nmol}_{\text{DOX}} \text{ mg}_{\text{NPs}}^{-1}$ ), while OuterDox demonstrated a 5-fold higher loading capacity in the range of 25-30  $\text{nmol}_{\text{DOX}} \text{ mg}_{\text{NPs}}^{-1}$ , as indicated by the stronger red color of the sample. DoubleDox NP suspension appeared as red as the OuterDox one, suggesting a high dose of doxorubicin loaded; nevertheless, UV-Vis measurements of different batches resulted in a great variability, ranging from a minimum loading of 15  $\text{nmol}_{\text{DOX}} \text{ mg}_{\text{NPs}}^{-1}$  to a maximum of 70  $\text{nmol}_{\text{DOX}} \text{ mg}_{\text{NPs}}^{-1}$ . This suggested that the condensation of IPTES-DOX complex conducted in acidic environment was less reproducible than the reaction promoted by alkaline pH conditions.



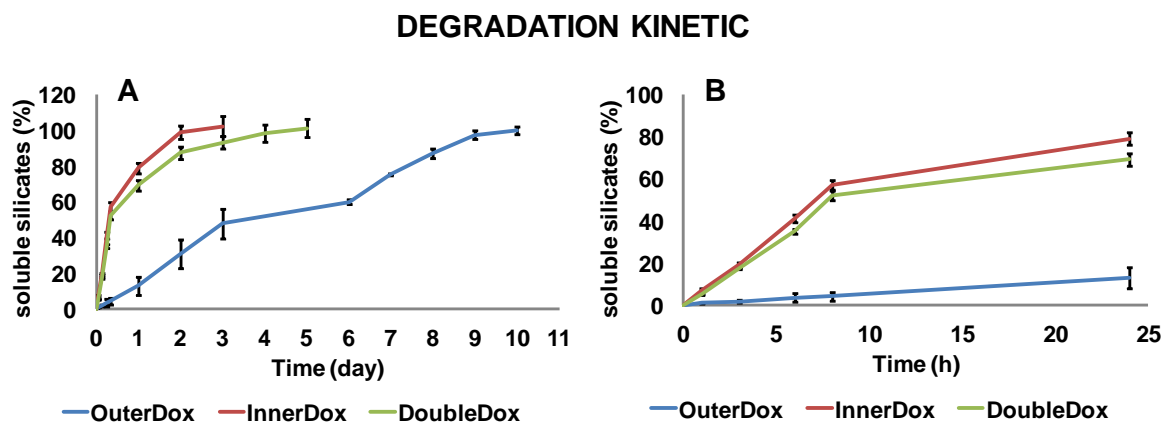
**Figure 2.14** UV-visible spectra of doxorubicin nanoformulations evidencing the presence of drug absorbance peak in comparison to unloaded Stöber SNPs. Images of  $10 \text{ mg mL}^{-1}$  nanosuspension are also reported, showing differences in red intensity.

### 2.9.2 – NP degradation and drug release kinetic studies

OuterDox, InnerDox and DoubleDox SNPs were assayed for their capacity to release the payload, taking into account that the process is strongly correlated to the degradation of the NPs. Thus, each kind of SNPs was incubated in a high saline buffer (20 mM HEPES, 1 mM  $\text{CaCl}_2$ , 150 mM NaCl, pH 7.4) – mimicking a physiological environment – for several hours and, at selected time points, the property of interest was monitored. In particular, the degradation kinetic was profiled by quantifying the soluble silicates released over time using



the silicomolybdic acid spectrophotometric method [49]: at desired time points, NPs were centrifuged and separated from the supernatants. The pellet was resuspended in fresh buffer whereas soluble silicates were titrated in the supernatants.

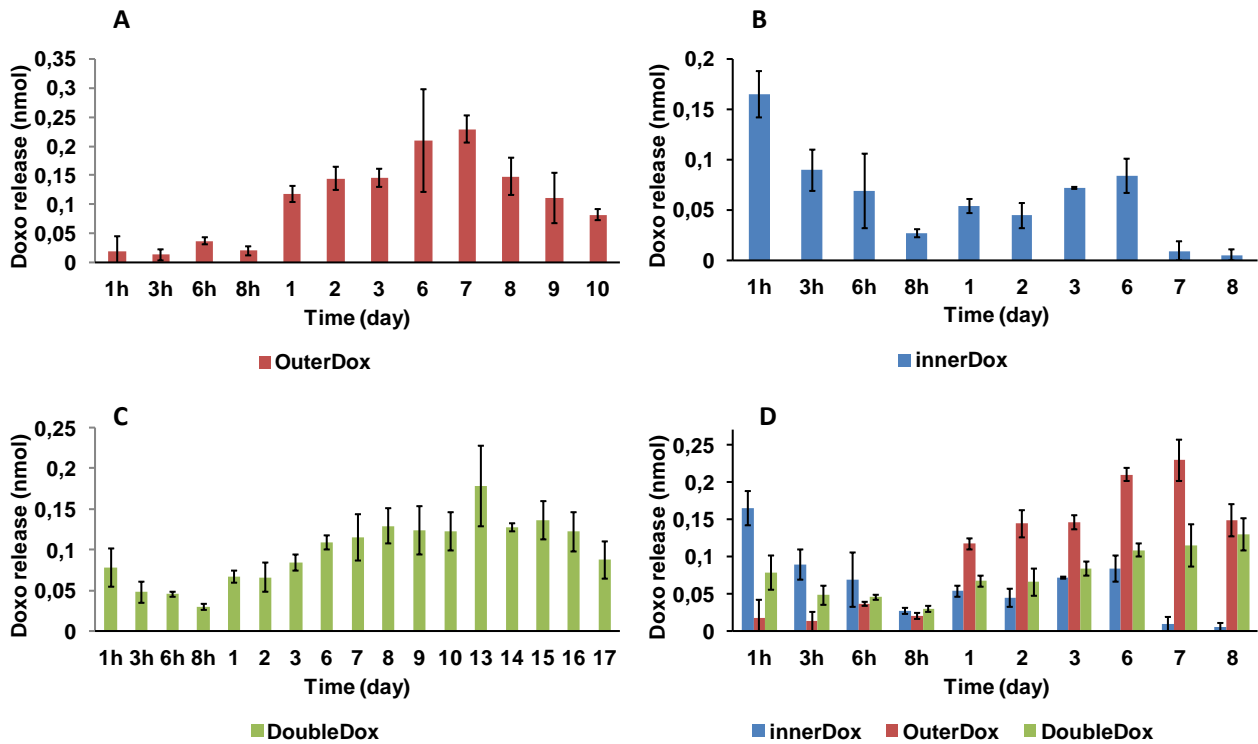


**Figure 2.15** Degradation profile of doxorubicin nanoformulations: SNPs ( $500 \mu\text{g mL}^{-1}$ ) were incubated in high saline buffer at  $37^\circ\text{C}$ ; at selected time points samples were centrifuged and supernatants analyzed by molybdenum colorimetric test. Soluble silicates are represented as percentage of the total amount of incubated SNPs. A) Complete dissolution kinetic; B) Magnification of the first 24 h.

Curves in Figure 2.15 showed a difference in the degradation behavior: InnerDox and DoubleDox NPs exhibited rapid release of soluble silicates during the first hours (0-8 h), while the degradation rate decreased in the subsequent few days, reaching the complete dissolution of NPs in 4 or 5 days. OuterDox NPs, instead, showed a reverse profile: the degradation rate remained low for the first day, leading only to the production of a 10% of soluble species; then the degradation gradually continued for several days, reaching 100% of dissolution at day 10.

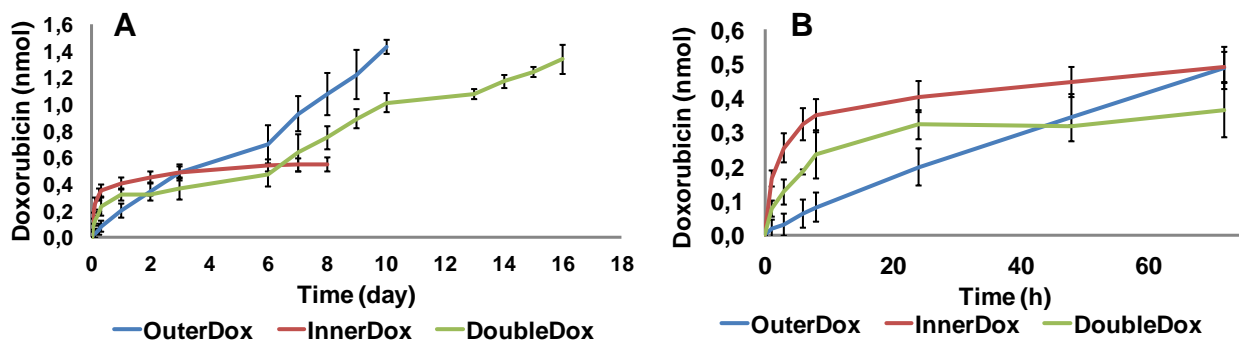
Doxorubicin release kinetic of SNPs reflected the differences observed in the degradation behavior. At the same established time points, the supernatants of pelleted NPs were analyzed by spectrofluorometer, allowing the determination of drug content released time-by-time (Figure 2.16) and, by sum, the cumulative amount (Figure 2.17). In Figure 2.16 the difference between OuterDox (Figure 2.16 A) and InnerDox (Figure 2.16 B) release profile appeared evident: at 1 h of incubation, InnerDox SNPs displayed a peak of release that slowly decreased until 8 h; on the contrary, within these time points, the drug was hardly detected in the supernatants of OuterDox SNPs. Starting from 24 h, InnerDox SNPs liberated an almost constant amount of cargo per day for no longer than a week, while OuterDox SNPs showed a linear increase, with a peak of doxorubicin detected at day 7. As expected, the profile shown by DoubleDox NPs enclosed both behaviors: a linear descending release from 1 to 8 h and then a continuous increment similar to the one of OuterDox SNPs, but with slight lower amounts of released drug, protracted for more days.

### TIME-BY-TIME RELEASE



**Figure 2.16** Drug release profile of doxorubicin nanoformulations: SNPs were incubated in high saline buffer at 37°C with a 12  $\mu$ M doxorubicin concentration; at selected time points samples were centrifuged and supernatants analyzed by spectrofluorometer ( $\lambda_{exc} = 485$ ,  $\lambda_{em} = 558$  nm). The release is represented as the time-by-time quantity detected for A) OuterDox, B) InnerDox and C) DoubleDox SNPs. Panel D) shows the merge of the three different profiles up to day 8.

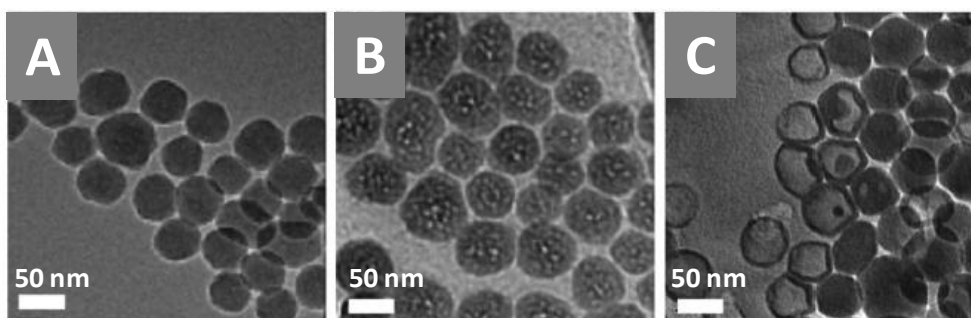
### CUMULATIVE RELEASE



**Figure 2.17** Drug release profile of doxorubicin nanoformulations represented as cumulative amount of doxorubicin. A) Complete release kinetic; B) Magnification of the first 72 h.

The cumulative release profile (Figure 2.17) evidenced the same phenomenon: InnerDox SNPs liberated their cargo mainly along the first 8 h, while reaching a plateau in the following days; the curve belonging to OuterDox SNPs did not reach 0.1 nmol before 24 h, whereas it significantly increased from 2 days onward. As expected, the DoubleDox NP release trend followed the InnerDox curve until 72 h (Figure 2.17 B) and afterwards rised up towards the OuterDox values.

Taken together, the carrier degradation and drug release patterns can be explained by an evolution mechanism of SNPs described in the literature [50]. Park and coworkers demonstrated that under mild basic conditions, such as the pH 7.4 of the high saline buffer used in our studies, SNPs synthesized by Stöber method spontaneously evolve from solid to hollow spheres, thus degrading from their interior to their exterior (Figure 2.18). The process seems to be governed by surface energy: first, small pores are created by the weakening of Si-O bonds due to  $\text{OH}^-$  ions (Figure 2.18 B), then these pores tend to collapse to reduce the surface energy and lastly merge to form a spherical cavity (Figure 2.18 C).



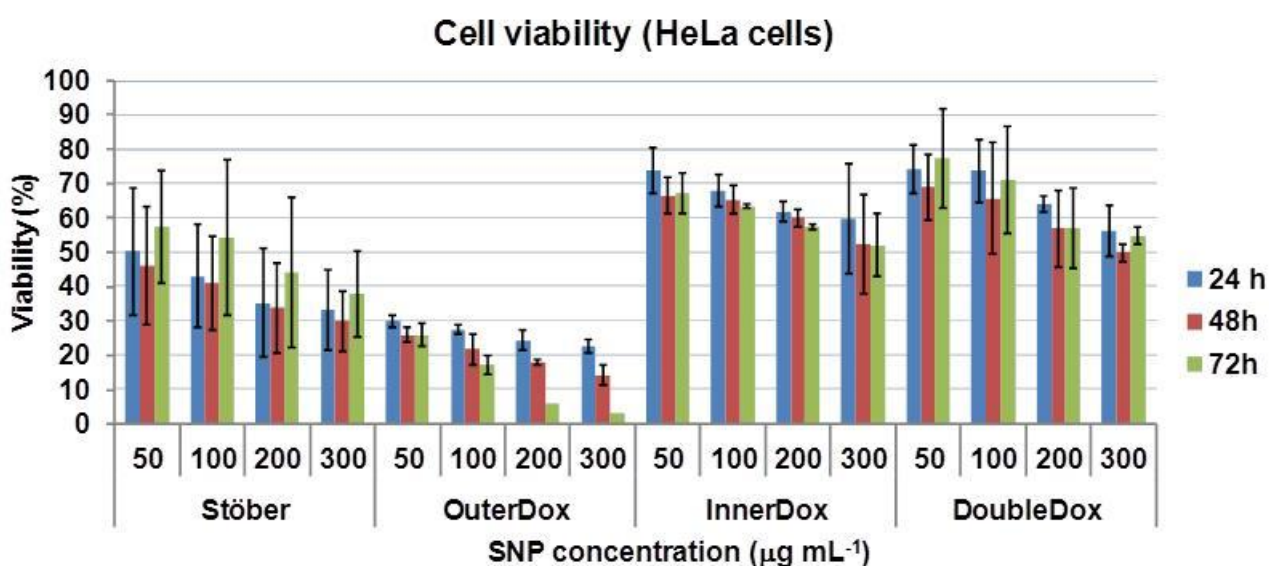
**Figure 2.18** Shape of Stöber SNPs stored in mild basic water (pH 7.5) was monitored by taking TEM images after A) 0, B) 15 and C) 30 days. Images taken form reference [50].

The surface energy is also responsible for the site-dependent dissolution, being lower at the exterior than that of the small pores of the internal core. Moreover, the interior of Stöber SNPs is known to be milder and more porous than the outer parts due to the NP formation mechanism that is based on the formation and aggregation of seeds [51]. Hence, the core is suggested to be composed by partially condensed nuclei that result more amenable to be hydrolyzed than the completely condensed exterior silicates. If we think about InnerDox SNP preparation, the internal part should be even softer, since the condensable species in the reaction are represented not only by TEOS, but also by IPTES-Dox complex, that itself can form only three Si-O bonds. Considering this, it is easier to understand the fast degradation of both InnerDox and DoubleDox SNPs and the consequent release of the cargo within the first hours. For OuterDox SNPs both processes are slowed down for the presence of IPTES-Dox

complex only on the outer surface, that leads to a denser core to solubilize and to a delayed release. After 24 h, DoubleDox SNPs should look more like the OuterDox NPs, with a dissolved core and a denser shell externally functionalized with the drug, hence demonstrating a similar release kinetic.

### 2.9.3 – *In vitro* studies of doxorubicin nanoformulation activity

Next, the cytotoxic effect of doxorubicin-loaded SNPs was verified. The viability of our NPs in HeLa cells – one of the most commonly used human cancer model cell line – was monitored by the 3-(4,5-Dimethylthiazol-2-yl)-2,5-diphenyltetrazolium bromide (MTT) assay [42]. MTT assay is a colorimetric enzyme-based method for determining mitochondrial dehydrogenase activity in living cells: when the enzymes work properly, the dye MTT is reduced to a purple-colored compound, indicating an appropriate cell proliferation. Viceversa, the less intense the color appears, the more the viability is decreasing. Hence, HeLa cells were incubated with various amounts of SNPs (from 50 to 300  $\mu\text{g mL}^{-1}$ ) and then analyzed spectrophotometrically. Doxorubicin-free Stöber SNPs were added as well in the experiment in order to check the possible cytotoxic contribution of the delivery vehicle.

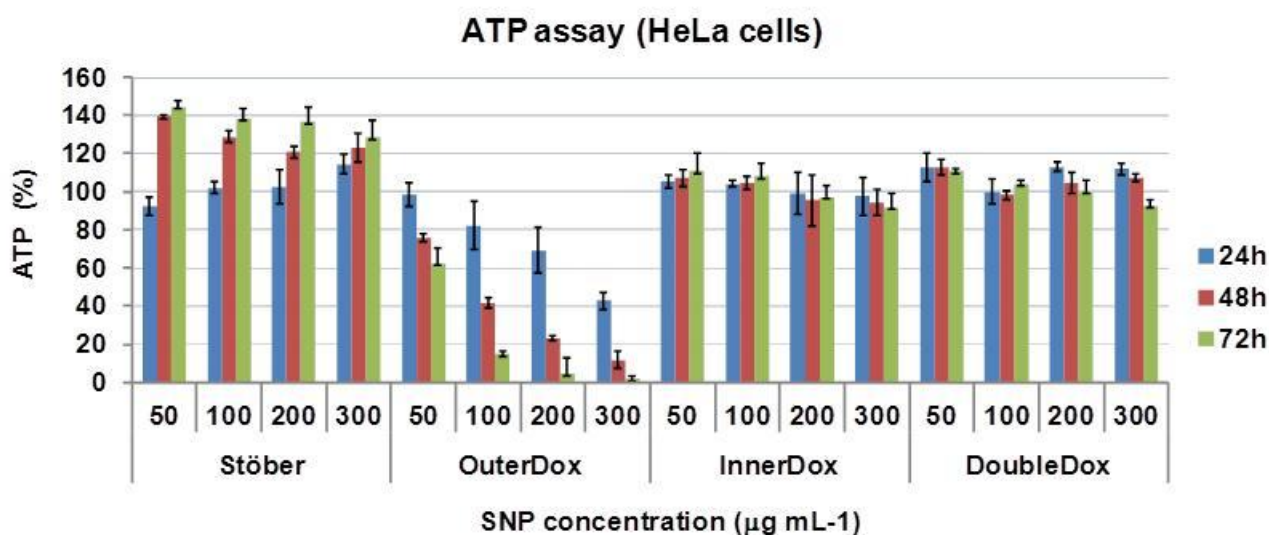


**Figure 2.19** SNPs toxicity was investigated by MTT test. HeLa cells were incubated with different concentrations of SNPs for 24, 48 and 72 h. Results are expressed as the percentage of viability versus untreated cells.

The results in Figure 2.19 show a concentration-dependent activity for all the nanoconjugates, with evident differences in the viability percentages. OuterDox SNPs led the cells to 30% of viability already at 24 h of incubation and at a concentration of 50  $\mu\text{g mL}^{-1}$ ; remarkably, a

complete vitality reduction was observed after 3 days of incubation with  $300 \mu\text{g mL}^{-1}$  of OuterDox SNPs. Considering an average doxorubicin loading of  $27 \text{ nmol}_{\text{DOX}} \text{ mg}_{\text{NPs}}^{-1}$ , OuterDox SNP doses corresponding to  $1 \mu\text{M}$  and  $8 \mu\text{M}$  of drug reduced the enzyme activity up to 30% and 3% respectively, in comparison to untreated cells. InnerDox SNPs displayed a distinctly lower cytotoxic effect, leading to a maximum of 50% of viability loss at the longest period of incubation and with the higher drug content, estimated to be around  $1.2 \mu\text{M}$ . The poor drug loading obtained in the synthesis of InnerDox SNPs thus resulted in a loss of activity, unless using a huge amount of silica. By the way, the most unexpected behavior was shown by DoubleDox SNPs that resulted even less toxic than InnerDox SNPs. The high standard deviation values can be attributed to the variability of drug loading obtained in DoubleDox synthesis, while it is hard to explain the reason of such cytotoxic behavior, basing only on this experiment. Also in the case of Stöber SNPs a singular profile was outlined: the MTT test revealed a considerable concentration-dependent antiproliferative effect towards cells at 24 and 48 h of incubation, while a recovery was observed at 72 h, suggesting a reverse phenomenon in action. Moreover, the huge standard deviations indicated a strong irreproducibility of the results, making the interpretation even more difficult. For this reason, we decided to deeper explore the anticancer activity of the nanodevices under investigation. Thus, the same cells were incubated in the same conditions of the previous test, and after 24, 48 and 72 h, the adenosine triphosphate (ATP) level was quantified by a bioluminescence assay (Figure 2.20) [52]. ATP, in fact, is considered a cell viability marker thanks to its presence in metabolically active cells, which declines rapidly whether cells undergo necrosis or apoptosis. The test appeared particularly suitable in case of doxorubicin-containing samples, as the anthracycline drug expresses its own anticancer activity inducing tumor cell apoptosis. The obtained data for doxorubicin-loaded SNPs confirmed the high antitumor effect of OuterDox SNPs, with a concentration and time-dependent trend and, on the contrary, the safe character of both InnerDox and DoubleDox SNPs. As explained before, InnerDox behavior could be attributed to the low quantity of carried doxorubicin, that probably results insufficiently released to be effective. Furthermore, we hypothesize that the poor dose of doxorubicin deriving from the core of DoubleDox SNPs could induce mild resistance in cancer cells, providing partial explanation to the reduced activity detected even at 72 h of incubation. In fact, the most reliable mechanism of resistance towards doxorubicin is the drug efflux *via* the P-glycoprotein 1 or the drug capture by lysosomes, both leading to a limited nuclear doxorubicin availability [53]. This means that, even though the theoretical cumulative release of the payload should be quite high in the case of DoubleDox at 72 h, probably the small time-

by-time quantity released before that time was able to trigger the efflux mechanism. Nevertheless, the hypothesis needs to be validated by strong experimental data. Interestingly, cells incubated with Stöber SNPs did not exhibit apoptosis signals, rather they seem to overproliferate during the experimental time. This evidence suggests that the cytotoxic effect observed in the MTT test was not due to an apoptotic event, but to others metabolic processes that probably don't lead to cell death.

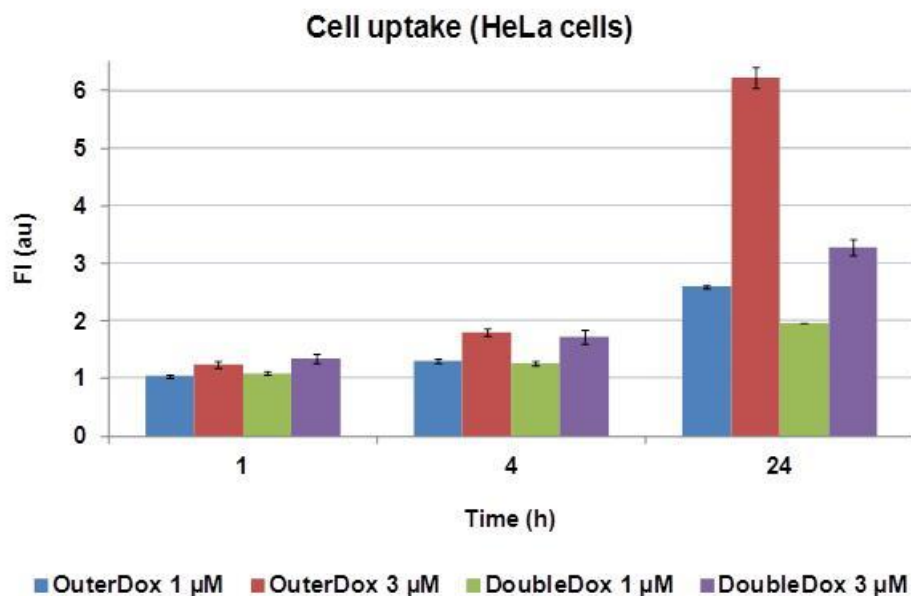


**Figure 2.20** SNP toxicity was investigated by ATP assay. HeLa cells were incubated with different concentrations of SNPs for 24, 48 and 72 h. Results are expressed as the percentage of ATP level versus untreated cells.

#### 2.9.4 – Cell uptake of doxorubicin nanoformulations

Figure 2.20 unexpectedly showed a strongly reduced activity in DoubleDox SNPs when compared to OuterDox SNPs. In order to investigate the cause for such an inconsistent behavior, we firstly check whether it could be due to a different pathway of internalization of SNPs inside the cells. HeLa cells were thus incubated with either OuterDox or DoubleDox SNPs and after 1, 4 and 24 h, cell uptake was assessed by flow cytometry, exploiting doxorubicin fluorescence. In order to have a quantitative comparison, we chose OuterDox and DoubleDox SNP batches with similar drug loading ( $25.0 \pm 1.0 \text{ nmol}_{\text{DOX}} \text{ mg}_{\text{NPs}}^{-1}$ ); in this way, the incubation of cells with 50 and 150  $\mu\text{g mL}^{-1}$  of SNPs resulted in a doxorubicin concentration of 1 and 3  $\mu\text{M}$  respectively. As we can see in Figure 2.21, both kinds of SNPs are internalized in cells in a concentration and time dependent-manner; interestingly, at 1 and 4 h of incubation, cell uptake was basically the same for OuterDox and DoubleDox SNPs, while a difference appears at 24 h: cells show a normalized fluorescence intensity of 2.6 when incubated with OuterDox SNPs 1  $\mu\text{M}$ , while the value is only 2.0 in presence of the same

quantity of DoubleDox SNPs. The discrepancy between SNPs is even higher when using a 3  $\mu\text{M}$  concentration, with a 2-fold higher fluorescence intensity of cells internalizing OuterDox SNPs compared to DoubleDox SNPs.



**Figure 2.21** *In vitro* uptake of SNPs. HeLa cells were incubated with different quantities of SiNPs (1 or 3  $\mu\text{M}$ ) for 1, 4 and 24 h. Cell uptake is expressed as fluorescence intensity (FI) normalized over the autofluorescence of untreated cells.

Flow cytometry experiments gave us a first explanation for the diverse cytotoxic activity of DoubleDox SNPs compared to OuterDox SNPs, observed both in the MTT and in the ATP assays. Nevertheless, further confirmation is needed to justify the safety of DoubleDox SNPs towards HeLa cancer cells.

## 2.10 – Conclusion

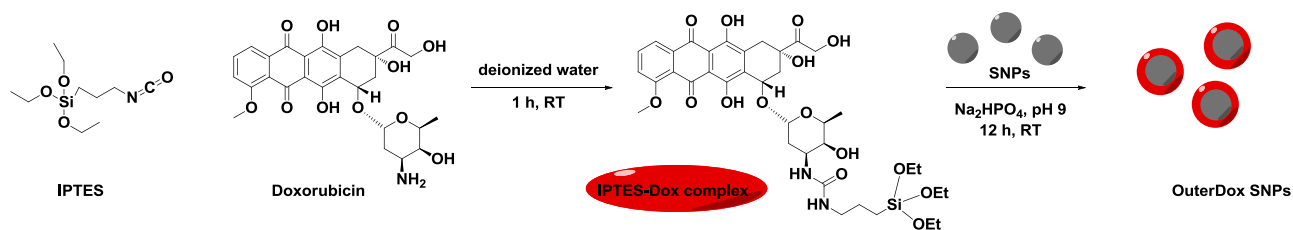
In the second part of the project aimed at developing a silica-based theranostic agent, we explored the possibility of using nonporous SNPs as delivery systems for the delivery of a cytotoxic agent. In our study, three different SNPs were designed and compared: OuterDox SNPs, where doxorubicin was grafted on the external surface of Stöber SNPs; InnerDox SNPs, where the cytotoxic molecule was covalently attached to a trialkoxysilane moiety and incorporated inside the silica core; and DoubleDox SNPs, where both loading strategies were employed at the same time, resulting in a double functionalized system. After the addition of a short and inert PEG shell, all the nanoconjugates were characterized in terms of size distribution and  $\zeta$ -potential, proving to be monodisperse and negatively charged. The determination of the drug content by UV-Vis analyses

directly on NP suspensions revealed the first difference between the nanoformulations: OuterDox SNPs were reproducibly loaded with a considerable quantity of doxorubicin ( $25\text{-}30 \text{ nmol}_{\text{DOX}} \text{ mg}_{\text{NPs}}^{-1}$ ); the reproducibility was recognized also in the drug incorporation of InnerDox SNPs, but only a small content was detected ( $3\text{-}5 \text{ nmol}_{\text{DOX}} \text{ mg}_{\text{NPs}}^{-1}$ ); DoubleDox SNPs could not be prepared with control over the functionalization yield, thus showing a drug loading range between 15 and 70  $\text{nmol}_{\text{DOX}} \text{ mg}_{\text{NPs}}^{-1}$ . Other differences were found in the cytotoxic effect *in vitro*. If OuterDox SNPs demonstrated high capability in reducing cell viability and inducing apoptosis events in HeLa cells, InnerDox SNPs resulted basically harmless, probably because of the low amount of drug. Surprisingly, DoubleDox SNPs showed neither cytotoxicity nor apoptotic activity, being more similar to InnerDox SNPs. Cell uptake experiments showed a time and concentration dependent internalization of both OuterDox and DoubleDox SNPs; nevertheless, at 24 h of incubation, OuterDox SNPs resulted 2-fold more internalized than the double-loaded particles, giving a first explanation for their poor cytotoxic activity. Taking into account all these data, we concluded that OuterDox SNPs are the best candidates to be developed for the design of a theranostic agent, being colloidally stable, reproducible and active on the tested tumor cell line. In the continuation of the project, OuterDox SNPs will be further functionalized with both the NTA linker to host  $^{99\text{m}}\text{Tc}$  and with the Hc-TZ targeting moiety, in order to be tested *in vitro* and *in vivo* for their therapeutic and diagnostic properties.



## 2.11 – Experimental section

### 2.11.1 - Synthesis of externally-doxorubicin-loaded silica nanoparticles (Outer SNPs)



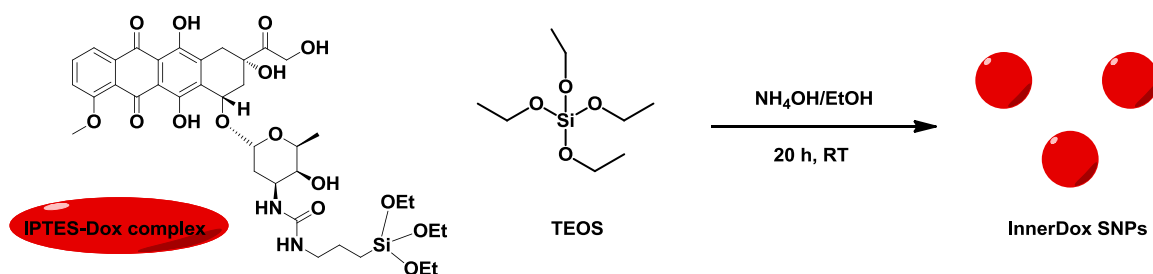
#### 2.11.1.1 – Synthesis of silica nanoparticles (SNPs)

Monodispersed 50 nm silica nanospheres (SNPs) were obtained by the Stöber synthesis [5]. Briefly, to an aqueous solution of  $\text{NH}_4\text{OH}$  28 wt.% (1.827 mg, 0.58 M) dry ethanol was added to reach a total volume of 50 mL and the mixture was rapidly stirred with a teflon bar. TEOS (1.99 mL, 0.17 M) was then added to this mixture and the reaction was stirred overnight at RT. The resultant SNPs suspension was transferred to water, washed by the excess of reagents and resuspended in water at a final particle concentration of  $10 \text{ mg mL}^{-1}$  for further functionalizations (concentration measured by drying 1 mL of NP suspension at  $100 \text{ }^\circ\text{C}$ , 3 h).

#### 2.11.1.2 – Doxorubicin grafting on external surface of SNPs (OuterDox SNPs)

Firstly IPTES-Dox complex was prepared by the addition of IPTES (4  $\mu\text{L}$ , 10.2  $\mu\text{mol}$ ) to water soluble doxorubicin hydrochloride (1 mL, 3.68  $\mu\text{mol}$ ). The reaction was left under stirring 1 h at RT and the complex was used immediately without further purification. SNPs (50 mg) were equilibrated twice in  $\text{Na}_2\text{HPO}_4$  (5 mL, 0.2 M, pH 9) and resuspended in the same buffer ( $10 \text{ mg mL}^{-1}$ ), then the IPTES-Dox complex was added and the reaction was stirred overnight at RT. Doxorubicin-loaded SNPs (OuterDox) were washed by the excess of reagents with high speed centrifugation (20000 rcf, 30 min,  $15 \text{ }^\circ\text{C}$ ) and resuspension in ultrapure water until the wasted volumes appeared clear (no unreacted doxorubicin left). Finally NPs were resuspended in ultrapure water to reach a final concentration of  $10 \text{ mg mL}^{-1}$ .

### 2.11.2 - Synthesis of SNPs internally loaded with doxorubicin (InnerDox SNPs)



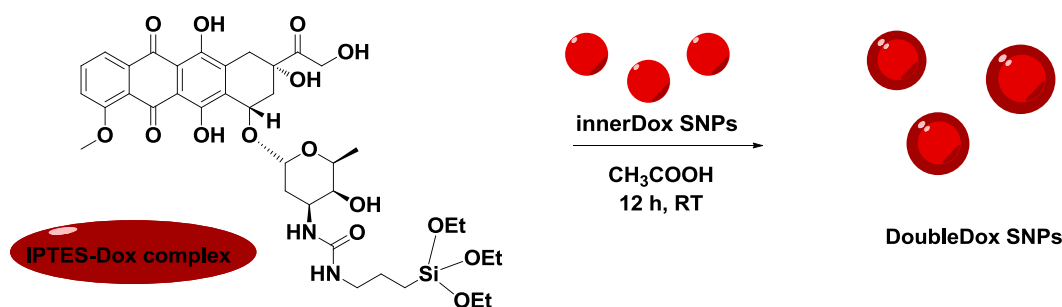
#### 2.11.2.1 – Doxorubicin transfer to organic phase

For synthetic purposes the commercially available doxorubicin hydrochloride was transferred to organic solvents. Triethylamine (12  $\mu\text{mol}$ , 2  $\mu\text{L}$ ) was added to doxorubicin hydrochloride in water (4  $\mu\text{mol}$ , 1 mL) and the hydrophobic doxorubicin was then extracted with chloroform (3  $\times$  3 mL). The resulting organic solution was dried on anhydrous  $\text{Na}_2\text{SO}_4$  and then evaporated under reduced pressure. The solid was redissolved in dry ethanol (2 mg  $\text{mL}^{-1}$ ) for further steps.

#### 2.11.2.2 – Synthesis of innerDox SNPs

A modified Stöber synthesis was used to prepare SNPs internally conjugated with Doxorubicin. Firstly the IPTES-Dox complex was prepared with a similar procedure presented in section 2.11.1.2, with the only modification being the dry ethanol as solvent instead of water. The as prepared complex was added in the Stöber reaction immediately before the TEOS, as a second condensating silane. Then the protocol was followed as before.

### 2.11.3 - Synthesis SNPs externally and internally functionalized with doxorubicin (doubleDox SNPs)



InnerDox SNPs, prepared as explained in paragraph 2.11.2, were used as starting point for the production of doubleDox SNPs. IPTES (2  $\mu\text{L}$ , 8.09  $\mu\text{mol}$ ) was added to 2 mg  $\text{mL}^{-1}$

doxorubicin hydrochloride (400  $\mu\text{L}$ , 1.47  $\mu\text{mol}$ ) in water and the reaction was performed as explained in paragraph 2.11.1.2. To an innerDox suspension 10  $\text{mg mL}^{-1}$  in ultrapure water (20  $\text{mg}$ ), glacial acetic acid (4.41  $\mu\text{mol}$ ) was added and the mixture sonicated for 2 min. After that, the previously synthesized IPTES-Dox complex in water (400  $\mu\text{L}$ ) was added and the reaction left under stirring overnight at RT. DoubleDox SNPs were washed by the excess of reagents with high speed centrifugation (20000 rcf, 30 min, 15  $^{\circ}\text{C}$ ) and resuspension in ultrapure water until the washed volumes appeared clear (no unreacted doxorubicin left). Finally nanoparticles were resuspended in ultrapure water to reach a NP concentration of 10  $\text{mg mL}^{-1}$ .

#### **2.11.4 - Stabilization of OuterDox, InnerDox and DoubleDox SNPs**

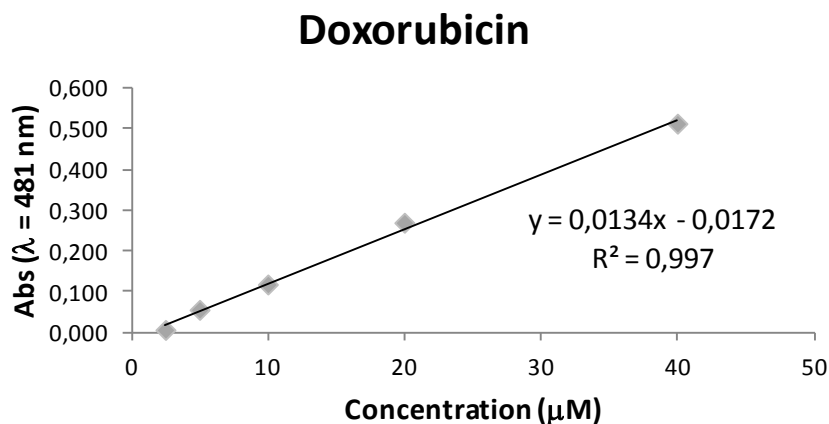
To improve the colloidal stability and the biocompatibility of the doxorubicin-loaded SNPs, we added a short PEG shell on the surface. Firstly, high density of amino groups was prepared with the procedure presented in paragraph 2.7.2.3. Then, all the amino functionalities, quantified by the Ninhydrin test, were saturated with MS(PEG)<sub>4</sub>, added in the reaction in a 2-fold molar excess. The reaction was left under stirring 2 h, after which SNPs were washed (20000 rcf, 20 min, 15  $^{\circ}\text{C}$ ) three times with water and redispersed in ultrapure water.

#### **2.11.5 – SNP characterization**

DLS measurements were performed with Zetasizer Nano ZS ZEN3600 (Malvern Instruments Ltd, Worcestershire, UK), equipped with a He-Ne laser ( $\lambda = 632.8 \text{ nm}$ ) working at 4 mW. A disposable cuvette with an optical length of 1 cm was used and scattered light was collected at 173 $^{\circ}$ . The samples were prepared with an average concentration of 100  $\mu\text{g mL}^{-1}$  in ultrapure water, and they were allowed to equilibrate at 25  $^{\circ}\text{C}$  for 30 s before the analysis. The Hd was derived using Stokes-Einstein equation, considering a viscosity of the medium of 0.8872 cP.  $\zeta$ -potential measurements were performed with the same instrument.  $\zeta$ -potential values were calculated by the Zetasizer Software basing on electrophoretic mobility and considering a viscosity of 0.8872 cP, dielectric constant of 78.5 and a Henry's function of 1.5. Samples were prepared with an average concentration of 100  $\mu\text{g mL}^{-1}$  in 1 mM NaCl (pH 7) and they were allowed to equilibrate at 25  $^{\circ}\text{C}$  for 30 s before the analysis. TEM images of NPs were obtained on a "FEI Tecnai G" Spirit BioTWIN microscope (Hillsboro, OR) operating at 120 kV. The samples were prepared by evaporating 2  $\mu\text{L}$  of NPs (generally 50  $\mu\text{g mL}^{-1}$ ) onto carbon-coated copper grid (200 mesh) and allowing it to dry on the air. The average particle diameter were obtained by measuring at least 100 particles by using imageJ software (National Institute of Health,

USA).

### 2.11.6 – Doxorubicin loading quantification



Doxorubicin loading in SNPs were derived exploiting the absorption properties of the drug and the optical transparency of silica in the same wavelength range, when keeping NP concentration below 3 mg mL<sup>-1</sup>. Specifically, a proper dilution of SNPs was prepared and analyzed with UV-Vis spectroscopy. The corresponding absorption value was taken at λ = 481 nm and molar Doxorubicin concentration was derived from a calibration curve previously prepared using known amount of doxorubicin in solution. Drug loading was calculated as presented in the equation below.

$$\frac{mol_{Doxo}}{mass_{SNPs}} \left( \frac{nmol}{mg} \right) = \frac{molar\ concentration_{Doxo} (\mu M)}{mass\ concentration_{SNPs} \left( \frac{mg}{mL} \right)}$$

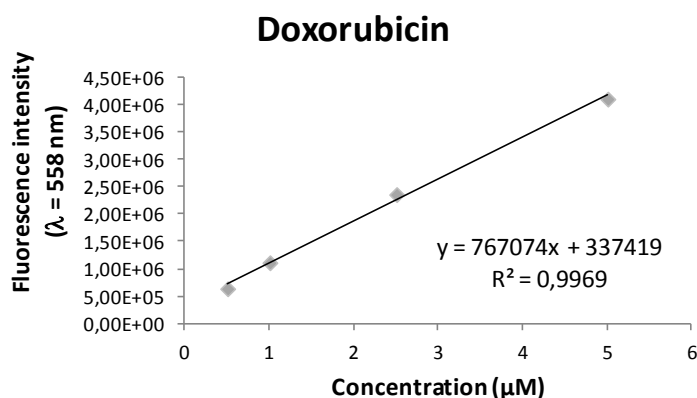
### 2.11.7 – Molybdenum colorimetric test for SNP degradation

SNPs (0.5 mg mL<sup>-1</sup>) were incubated in a high saline buffer (20 mM HEPES, 150 mM NaCl, 1 mM CaCl<sub>2</sub>, pH 7.4) at 37 °C with mild agitation. The Molybdenum Blue assay was used to calculate the amount of soluble silicates released corresponding to NP degradation [49]. Briefly, at different time points SNPs were separated from the supernatant by centrifugation (20000 rcf, 20 min) and redispersed in a fresh volume of the degradation buffer. 100 µL of the collected supernatant was transferred to a plastic tube. To this volume 50 µL each of 1 M HCl, 0.27 M Na<sub>2</sub>EDTA and 0.265 M (NH<sub>4</sub>)<sub>2</sub>MoO<sub>4</sub> were added rapidly. After 10 minutes 50 µL of

0.67 M tartaric acid were added. After 10 minutes more 100  $\mu\text{L}$  of 1.35 M sodium sulfite were added and the solution was left 1 h to fully develop the blue color. The samples were then analyzed with UV-vis spectrophotometer taking absorbance values at  $\lambda = 700 \text{ nm}$ ; blank sample was prepared exposing 100  $\mu\text{L}$  of NP-free degradation buffer to the same test conditions. Standard calibration curve was created using soluble silicate solution in a concentration range between 5–200  $\mu\text{g mL}^{-1}$  subjected to the same procedure. Results of SNP degradation at each time point were the average of three replicates for three different batches and were presented as:

$$\text{degradation (\%)} = \frac{\text{total soluble silicates } (\mu\text{g})}{\text{initial SNPs mass } (\mu\text{g})}$$

### 2.11.8 – Fluorescence spectroscopy for drug release profile



For the drug release profile SNPs were incubated with a doxorubicin concentration of 12  $\mu\text{M}$  in the same conditions of the degradation test. At the same time points SNPs were separated from the supernatant by centrifugation (20000 rcf, 20 min, 15  $^{\circ}\text{C}$ ) and redispersed in a fresh volume of the degradation buffer. The collected supernatant were directly analyzed by spectrofluorometer, with excitation at  $\lambda_{\text{exc}} = 485 \text{ nm}$  and fluorescence intensity value taken at the maximum of emission ( $\lambda_{\text{em}} = 558 \text{ nm}$ ). The doxorubicin quantity was derived at each time point from a previously prepared calibration curve. The results at each time point were the average of three replicates for three different batches and were presented both as time-by-time drug released (nmol) and cumulative drug released (nmol).

### 2.11.9 – Cell proliferation assay

*In vitro* cytotoxicity of SNPs was tested on HeLa cell line through MTT assay (CellTiter 96 Non-Radioactive cell proliferation assay – Promega). Cells were seeded in 96-well plates at a density of  $5 \times 10^3$  cells per well and incubated for 24 h at 37 °C in a humidified atmosphere, 5% CO<sub>2</sub> air. Then, cells were treated with different quantities of SNPs (50, 100, 200 and 300  $\mu\text{g mL}^{-1}$ ) for 24, 48 and 72 h. At the indicated time points, 10  $\mu\text{L}$  of MTT stock solution was added to each well. After 4 h of incubation, MTT solubilizing solution (0.1 mL) was added to each well to dissolve the formazan crystals and then plates were analyzed using EnSight™ Multimode Plate Reader (Perkin Elmer®), reading the absorbance at 570 nm and subtracting the absorbance of background at 650 nm. The results are expressed as means  $\pm$  standard error (s.e.) of five replicates.

#### **2.11.10 – Cell viability by ATP assay**

HeLa cells ( $5 \times 10^3$  cell/well) were seeded in a 96-well black culture plate (Perkin Elmer) and treated with different quantities of SNPs ~~diluted in cell culture medium~~ (50, 100, 200 and 300  $\mu\text{g mL}^{-1}$ ) for 24, 48 and 72 h. Cell viability was determined with a luminescent ATP detection kit, “ATPLite 1step” (Perkin Elmer), according to the manufacturer’s directions. Briefly, the substrate vial and the buffer solution were equilibrated at room temperature, then the lyophilized substrate solution was reconstituted by adding the appropriate volume of buffer. 0.1 mL of the reconstituted reagent were added to each well and after 2 minutes of vigorous shaking the luminescence was measured. Light generated by ATP in each sample were detected by an EnSight multimode plate reader (Perkin Elmer). Average light units were normalized to control and expressed as the relative ATP level.

#### **2.11.11 – Cellular uptake by flow cytometry**

HeLa cells ( $3 \times 10^5$  cells per well) were seeded in a 12-well plate and after 24 h incubated with different quantities of OuterDox and DoubleDox SNPs, corresponding to 1  $\mu\text{M}$  and 3  $\mu\text{M}$  doxorubicin concentrations. After different incubation times (1 h, 4 h, 24 h), cells were washed twice with PBS and harvested in FACS tubes, washed again and resuspended in 0.5 mL of PBS, 1 mM EDTA.  $10^5$  events were acquired for each analysis on Gallios™ Flow Cytometer (Beckman Coulter Inc.) exploiting doxorubicin emission (green fluorescence). Both the percentage of the fluorescent cells relative to the control (untreated cells) and the mean fluorescent intensity of the fluorescence-positive cells were taken into account. The results were analyzed using FlowJo software.

## References

1. Tang, L.; Cheng, J. Nonporous silica nanoparticles for nanomedicine application. *Nano Today* **2013**, *8*, 290–312.
2. Wang, Y.; Zhao, Q.; Han, N.; Bai, L.; Li, J.; Liu, J.; Che, E.; Hu, L.; Zhang, Q.; Jiang, T.; Wang, S. Mesoporous silica nanoparticles in drug delivery and biomedical applications. *Nanomedicine Nanotechnol. Biol. Med.* **2015**, *11*, 313–327.
3. Stöber, W.; Fink, A.; Bohn, E. Controlled growth of monodisperse silica spheres in the micron size range. *J. Colloid Interface Sci.* **1968**, *26*, 62–69.
4. Van Blaaderen, A.; Van Geest, J.; Vrij, A. Monodisperse colloidal silica spheres from tetraalkoxysilanes: Particle formation and growth mechanism. *J. Colloid Interface Sci.* **1992**, *154*, 481–501.
5. Mahon, E.; Hristov, D. R.; Dawson, K. A. Stabilising fluorescent silica nanoparticles against dissolution effects for biological studies. *Chem. Commun.* **2012**, *48*, 7970–7972.
6. Nozawa, K.; Gailhanou, H.; Raison, L.; Panizza, P.; Ushiki, H.; Sellier, E.; Delville, J. P.; Delville, M. H. Smart control of monodisperse Stöber silica particles: effect of reactant addition rate on growth process. *Langmuir ACS J. Surf. Colloids* **2005**, *21*, 1516–1523.
7. Taylor-Pashow, K. M. L.; Della Rocca, J.; Huxford, R. C.; Lin, W. Hybrid nanomaterials for biomedical applications. *Chem. Commun.* **2010**, *46*, 5832.
8. Finnie, K. S.; Bartlett, J. R.; Barbé, C. J. A.; Kong, L. Formation of Silica Nanoparticles in Microemulsions. *Langmuir* **2007**, *23*, 3017–3024.
9. Bagwe, R. P.; Yang, C.; Hilliard, L. R.; Tan, W. Optimization of dye-doped silica nanoparticles prepared using a reverse microemulsion method. *Langmuir ACS J. Surf. Colloids* **2004**, *20*, 8336–8342.
10. Guerrero-Martínez, A.; Pérez-Juste, J.; Liz-Marzán, L. M. Recent progress on silica coating of nanoparticles and related nanomaterials. *Adv. Mater. Deerfield Beach Fla* **2010**, *22*, 1182–1195.
11. Kuijk, A.; van Blaaderen, A.; Imhof, A. Synthesis of Monodisperse, Rodlike Silica Colloids with Tunable Aspect Ratio. *J. Am. Chem. Soc.* **2011**, *133*, 2346–2349.
12. Fu, C.; He, C.; Tan, L.; Wang, S.; Shang, L.; Li, L.; Meng, X.; Liu, H. High-yield preparation of robust gold nanoshells on silica nanorattles with good biocompatibility. *Sci. Bull.* **2016**, *61*, 282–291.
13. Nakashima, Y.; Takai, C.; Razavi-Khosroshahi, H.; Shirai, T.; Fuji, M. Effects of primary- and secondary-amines on the formation of hollow silica nanoparticles by using emulsion template method. *Colloids Surf. -Physicochem. Eng. Asp.* **2016**, *506*, 849–854.
14. Kim, B.; Han, G.; Toley, B. J.; Kim, C.-K.; Rotello, V. M.; Forbes, N. S. Tuning payload delivery in tumour cylindroids using gold nanoparticles. *Nat. Nanotechnol.* **2010**, *5*, 465–472.
15. GRAS Notices <http://www.accessdata.fda.gov/scripts/fdcc/index.cfm?set=GRASNotices> (accessed Oct 7, 2016).
16. Friedman, R. Nano Dot Technology Enters Clinical Trials. *J. Natl. Cancer Inst.* **2011**, *103*, 1428–1429.
17. Bradbury, M. S.; Phillips, E.; Montero, P. H.; Cheal, S. M.; Stambuk, H.; Durack, J. C.; Sofocleous, C. T.; Meester, R. J. C.; Wiesner, U.; Patel, S. Clinically-translated silica nanoparticles as dual-modality cancer-targeted probes for image-guided surgery and interventions. *Integr. Biol. Quant. Biosci. Nano Macro* **2013**, *5*, 74–86.

18. Burns, A. A.; Vider, J.; Ow, H.; Herz, E.; Penate-Medina, O.; Baumgart, M.; Larson, S. M.; Wiesner, U.; Bradbury, M. Fluorescent Silica Nanoparticles with Efficient Urinary Excretion for Nanomedicine. *Nano Lett.* **2009**, *9*, 442–448.
19. Phillips, E.; Penate-Medina, O.; Zanzonico, P. B.; Carvajal, R. D.; Mohan, P.; Ye, Y.; Humm, J.; Gönen, M.; Kalaigian, H.; Schöder, H.; Strauss, H. W.; Larson, S. M.; Wiesner, U.; Bradbury, M. S. Clinical translation of an ultras-small inorganic optical-PET imaging nanoparticle probe. *Sci. Transl. Med.* **2014**, *6*, 260ra149–260ra149.
20. Siegel, R. L.; Miller, K. D.; Jemal, A. Cancer statistics, 2015. *CA. Cancer J. Clin.* **2015**, *65*, 5–29.
21. Engel, R. H.; Kaklamani, V. G. HER2-Positive Breast Cancer. *Drugs* **2012**, *67*, 1329–1341.
22. Colombo, M.; Corsi, F.; Foschi, D.; Mazzantini, E.; Mazzucchelli, S.; Morasso, C.; Occhipinti, E.; Polito, L.; Prosperi, D.; Ronchi, S.; Verderio, P. HER2 targeting as a two-sided strategy for breast cancer diagnosis and treatment: Outlook and recent implications in nanomedical approaches. *Pharmacol. Res.* **2010**, *62*, 150–165.
23. Chang, H. R. Trastuzumab-based neoadjuvant therapy in patients with HER2-positive breast cancer. *Cancer* **2010**, *116*, 2856–2867.
24. Hudis, C. A. Trastuzumab--mechanism of action and use in clinical practice. *N. Engl. J. Med.* **2007**, *357*, 39–51.
25. Slamon, D. J.; Leyland-Jones, B.; Shak, S.; Fuchs, H.; Paton, V.; Bajamonde, A.; Fleming, T.; Eiermann, W.; Wolter, J.; Pegram, M.; Baselga, J.; Norton, L. Use of chemotherapy plus a monoclonal antibody against HER2 for metastatic breast cancer that overexpresses HER2. *N. Engl. J. Med.* **2001**, *344*, 783–792.
26. Zardavas, D.; Fouad, T. M.; Piccart, M. Optimal adjuvant treatment for patients with HER2-positive breast cancer in 2015. *The Breast* **2015**, *24*, Supplement 2, S143–S148.
27. Pohlmann, P. R.; Mayer, I. A.; Mernaugh, R. Resistance to Trastuzumab in Breast Cancer. *Clin. Cancer Res.* **2009**, *15*, 7479–7491.
28. Tchrakian, N.; Flanagan, L.; Harford, J.; Gannon, J. M.; Quinn, C. M. New ASCO/CAP guideline recommendations for HER2 testing increase the proportion of reflex in situ hybridization tests and of HER2 positive breast cancers. *Virchows Arch.* **2015**, *468*, 207–211.
29. Wolff, A. C.; Hammond, M. E. H.; Schwartz, J. N.; Hagerty, K. L.; Allred, D. C.; Cote, R. J.; Dowsett, M.; Fitzgibbons, P. L.; Hanna, W. M.; Langer, A.; McShane, L. M.; Paik, S.; Pegram, M. D.; Perez, E. A.; Press, M. F.; Rhodes, A.; Sturgeon, C.; Taube, S. E.; Tubbs, R.; Vance, G. H.; van de Vijver, M.; Wheeler, T. M.; Hayes, D. F.; American Society of Clinical Oncology; College of American Pathologists American Society of Clinical Oncology/College of American Pathologists guideline recommendations for human epidermal growth factor receptor 2 testing in breast cancer. *J. Clin. Oncol. Off. J. Am. Soc. Clin. Oncol.* **2007**, *25*, 118–145.
30. Wolff, A. C.; Hammond, M. E. H.; Hicks, D. G.; Dowsett, M.; McShane, L. M.; Allison, K. H.; Allred, D. C.; Bartlett, J. M. S.; Bilous, M.; Fitzgibbons, P.; Hanna, W.; Jenkins, R. B.; Mangu, P. B.; Paik, S.; Perez, E. A.; Press, M. F.; Spears, P. A.; Vance, G. H.; Viale, G.; Hayes, D. F.; American Society of Clinical Oncology; College of American Pathologists Recommendations for human epidermal growth factor receptor 2 testing in breast cancer: American Society of Clinical Oncology/College of American Pathologists clinical practice guideline update. *J. Clin. Oncol. Off. J. Am. Soc. Clin. Oncol.* **2013**, *31*, 3997–4013.



31. Kulhari, H.; Pooja, D.; Rompicharla, S. V. K.; Sistla, R.; Adams, D. J. Biomedical Applications of Trastuzumab: As a Therapeutic Agent and a Targeting Ligand. *Med. Res. Rev.* **2015**, *35*, 849–876.
32. Fiandra, L.; Mazzucchelli, S.; De Palma, C.; Colombo, M.; Allevi, R.; Sommaruga, S.; Clementi, E.; Bellini, M.; Prospero, D.; Corsi, F. Assessing the In Vivo Targeting Efficiency of Multifunctional Nanoconstructs Bearing Antibody-Derived Ligands. *ACS Nano* **2013**, *7*, 6092–6102.
33. Gambhir, S. S. Molecular imaging of cancer with positron emission tomography. *Nat. Rev. Cancer* **2002**, *2*, 683–693.
34. Ahlgren, S.; Wällberg, H.; Tran, T. A.; Widström, C.; Hjertman, M.; Abrahmsén, L.; Berndorff, D.; Dinkelborg, L. M.; Cyr, J. E.; Feldwisch, J.; Orlova, A.; Tolmachev, V. Targeting of HER2-expressing tumors with a site-specifically <sup>99m</sup>Tc-labeled recombinant affibody molecule, ZHER2:2395, with C-terminally engineered cysteine. *J. Nucl. Med. Off. Publ. Soc. Nucl. Med.* **2009**, *50*, 781–789.
35. Meszaros, L. K.; Dose, A.; Biagini, S. C. G.; Blower, P. J. Hydrazinonicotinic acid (HYNIC) – Coordination chemistry and applications in radiopharmaceutical chemistry. *Inorganica Chim. Acta* **2010**, *363*, 1059–1069.
36. Lipowska, M.; Marzilli, L. G.; Taylor, A. T. <sup>99m</sup>Tc(CO)<sub>3</sub>-nitrilotriacetic acid: a new renal radiopharmaceutical showing pharmacokinetic properties in rats comparable to those of <sup>131</sup>I-OIH. *J. Nucl. Med. Off. Publ. Soc. Nucl. Med.* **2009**, *50*, 454–460.
37. Egli, A.; Alberto, R.; Tannahill, L.; Schibli, R.; Abram, U.; Schaffland, A.; Waibel, R.; Tourwé, D.; Jeannin, L.; Iterbeke, K.; Schubiger, P. A. Organometallic <sup>99m</sup>Tc-aquaion labels peptide to an unprecedented high specific activity. *J. Nucl. Med.* **1999**, *40*, 1913–1917.
38. Minotti, G.; Ronchi, R.; Salvatorelli, E.; Menna, P.; Cairo, G. Doxorubicin Irreversibly Inactivates Iron Regulatory Proteins 1 and 2 in Cardiomyocytes Evidence for Distinct Metabolic Pathways and Implications for Iron-mediated Cardiotoxicity of Antitumor Therapy. *Cancer Res.* **2001**, *61*, 8422–8428.
39. Yokoi, T.; Sakamoto, Y.; Terasaki, O.; Kubota, Y.; Okubo, T.; Tatsumi, T. Periodic arrangement of silica nanospheres assisted by amino acids. *J. Am. Chem. Soc.* **2006**, *128*, 13664–13665.
40. Blanco, E.; Shen, H.; Ferrari, M. Principles of nanoparticle design for overcoming biological barriers to drug delivery. *Nat. Biotechnol.* **2015**, *33*, 941–951.
41. Waibel, R.; Alberto, R.; Willuda, J.; Finnern, R.; Schibli, R.; Stichelberger, A.; Egli, A.; Abram, U.; Mach, J. P.; Plückthun, A.; Schubiger, P. A. Stable one-step technetium-<sup>99m</sup> labeling of His-tagged recombinant proteins with a novel Tc(I)-carbonyl complex. *Nat. Biotechnol.* **1999**, *17*, 897–901.
42. Almutary, A.; Sanderson, B. J. S. The MTT and Crystal Violet Assays: Potential Confounders in Nanoparticle Toxicity Testing. *Int. J. Toxicol.* **2016**, *35*, 454–462.
43. Li, C.; Zhang, Y.; Wang, L.; Feng, H.; Xia, X.; Ma, J.; Yuan, H.; Gao, B.; Lan, X. A novel multivalent (<sup>99m</sup>Tc)-labeled EG2-C4bpα antibody for targeting the epidermal growth factor receptor in tumor xenografts. *Nucl. Med. Biol.* **2015**, *42*, 547–554.
44. Soto-Cantu, E.; Cueto, R.; Koch, J.; Russo, P. S. Synthesis and Rapid Characterization of Amine-Functionalized Silica. *Langmuir* **2012**, *28*, 5562–5569.
45. Tang, L.; Fan, T. M.; Borst, L. B.; Cheng, J. Synthesis and Biological Response of Size-Specific, Monodisperse Drug–Silica Nanoconjugates. *ACS Nano* **2012**, *6*, 3954–3966.

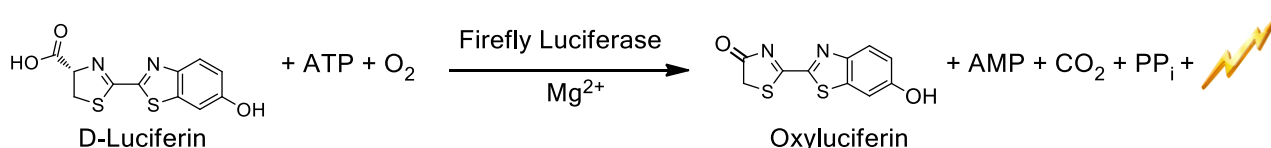
46. Tang, L.; Gabrielson, N. P.; Uckun, F. M.; Fan, T. M.; Cheng, J. Size-Dependent Tumor Penetration and in Vivo Efficacy of Monodisperse Drug–Silica Nanoconjugates. *Mol. Pharm.* **2013**, *10*, 883–892.
47. Xu, Z.; Liu, S.; Kang, Y.; Wang, M. Glutathione- and pH-responsive nonporous silica prodrug nanoparticles for controlled release and cancer therapy. *Nanoscale* **2015**, *7*, 5859–5868.
48. Zhang, S.; Chu, Z.; Yin, C.; Zhang, C.; Lin, G.; Li, Q. Controllable Drug Release and Simultaneously Carrier Decomposition of SiO<sub>2</sub>-Drug Composite Nanoparticles. *J. Am. Chem. Soc.* **2013**, *135*, 5709–5716.
49. Coradin, T.; Eglin, D.; Livage, J. The silicomolybdic acid spectrophotometric method and its application to silicate/biopolymer interaction studies. *J. Spectrosc.* **2004**, *18*, 567–576.
50. Park, S.-J.; Kim, Y.-J.; Park, S.-J. Size-dependent shape evolution of silica nanoparticles into hollow structures. *Langmuir ACS J. Surf. Colloids* **2008**, *24*, 12134–12137.
51. Bogush, G. H.; Tracy, M. A.; Zukoski IV, C. F. Preparation of monodisperse silica particles: Control of size and mass fraction. *J. Non-Cryst. Solids* **1988**, *104*, 95–106.
52. ATPlite Luminescence Assay <http://www.perkinelmer.com/lab-solutions/resources/docs/MAN-ATPlite.pdf> (accessed Dec 22, 2016).
53. Wijdeven, R. H.; Pang, B.; Assaraf, Y. G.; Neefjes, J. Old drugs, novel ways out: Drug resistance toward cytotoxic chemotherapeutics. *Drug Resist. Updat.* **2016**, *28*, 65–81.

# **CHAPTER 3**

## **ANALYTICAL TOOLS**

### 3.1 – Bioluminescence imaging

In recent years, a set of imaging technologies has emerged to non-invasively visualize biological features in organs, tissues, cells, or at the molecular level within animal models. These methods are providing unprecedented insight into the cell and organism biology, and revealing previously unknown mechanisms of disease development [1,2]. Among these techniques, bioluminescence imaging represents a cost-effective method that enables real-time analysis of biological processes in intact organisms. Bioluminescence is defined as the emission of light via an enzymatic reaction, in which a chemical substrate (luciferin) is oxidized by an enzyme (luciferase). The phenomenon of bioluminescence has been observed in many different organisms including bacteria, fungi, algae, fishes, squid, shrimp and insects, among which the most extensively studied is the firefly [3]. Firefly luciferase catalyzes the emission of yellow-green light from the substrate D-luciferin,  $Mg^{2+}$ -ATP, and oxygen (Scheme 3.1), following a multistep process: first, the enzyme catalyzes the formation of its complex with adenylated luciferin in the presence of  $Mg^{2+}$  and ATP, by the release of inorganic pyrophosphate (PPi); then, the adenylated luciferin is converted by molecular oxygen to oxyluciferin in the excited state, together with the production of adenosine monophosphate (AMP) and carbon dioxide ( $CO_2$ ); finally, the relaxation of oxyluciferin to the corresponding ground state results in the emission of light.



**Scheme 3.1** Bioluminescent reaction between luciferin and luciferase.

Bioluminescence imaging is based on the introduction and expression of a specific gene to produce luciferase and on the subsequent administration of the luciferin substrate: as soon as the partners interact, light is detected by specialized charge coupled device (CCD) cameras that convert photons into electrons after striking silicon wafers. The technique relying on bioluminescence reaction possesses various advantages over other imaging technologies, including fluorescence. First of all, the luminous signal is produced without any excitation light source, implying the elimination of photobleaching and phototoxicity. Besides, the light emission persists as long as the substrate is present, so that it can be recorded for long

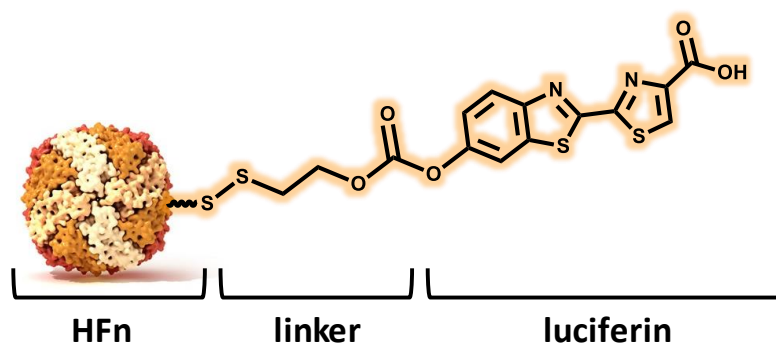
timescale without damaging reporter molecules or cells. The luciferase/luciferin system proved to be well suited for *in vivo* imaging also because there are almost no endogenous light emitting processes in cells and tissues, so that the background signal is negligible. Such high signal-to-noise ratio appears particularly attractive for sensitive imaging applications within the complex biological environment. Lastly, the technology is widely compatible with rodent and other animal models, as the strong emission at red wavelengths (550-600 nm) can be usually detected at depths of few centimeters through blood and tissues. The versatility and user-friendly features of bioluminescence have paved the way to its application in numerous biomedical researches [4,5]. The traditional applications include cell tracking, with the intensity of the bioluminescent signal correlating with the number of cells in a given area, and gene expression visualization, in which luciferase is produced only when the promoter sequence of a gene of interest have been actively transcribed. More recent advances have led to the employment of bioluminescence imaging for individual biomolecule investigations, such as protein abundance and function monitoring, measurements of enzymatic activities in complex environments, metabolites detection *etc* [6].

### 3.1.1 – Bioluminescence imaging of tumors

One of the most explored application of bioluminescence imaging is represented by the molecular imaging of cancer models. Deciphering the complex interactions between tumor cells and their microenvironment is of paramount importance to understand cancer behavior and to guide new anticancer therapies. Tumor imaging, and specifically bioluminescence imaging, offers the opportunity to noninvasively monitor various types of cell mechanisms *in vivo* in real time. In fact, mouse models can be genetically engineered not only to spontaneously develop cancers, but also to express bioluminescent reporters (*id est* luciferases), which permit to monitor transcriptional regulation, posttranscriptional and posttranslational events in tumor cells. Moreover, genetically encoded reporters can be coupled to oncogenic proteins so to provide even more information about chemoresistance, inflammation, angiogenesis, DNA maintenance, apoptosis *etc* [7]. What is more, the presence of luciferase permits the detection of small non-palpable tumors [8], tumor burdens [9] and metastasis [10]. Bioluminescence imaging is also exploited for preclinical studies of new anticancer therapies, offering the ability to assess cytotoxic, antimetastatic or antiangiogenic activities of novel drugs [11]. The broad spectrum of possibilities opened up by this technique explains the increasing interest of the scientific community for tumor bioluminescence imaging.

### 3.2 – Development of glutathione-sensitive apoferritin nanoparticles for the controlled delivery of luciferin

Although bioluminescence imaging has been successfully used in a variety of applications to obtain information regarding biological processes *in vivo*, the detection of photon emission is limited by the short half-life of luciferin (less than 30 minutes), its modest cell penetration and inhomogeneous diffusion into different tissues [12–14]. Efforts to overcome the limitation of the method have focused mainly on luciferase modifications, including either the increase of expression levels of the enzyme [15] or the mutation that can lead to a redshift of the emitted light and the consequent augmented tissue penetration [16]. Only a few works, however, present strategies that aim at modulating the luciferin properties. Some research groups tried to synthesize luciferin derivatives or analogues to obtain prolonged half-lives or a red-shifted bioluminescent emission [17]; others employed nanoparticles to encapsulate luciferin for prolonged bioluminescence [18]. The latest advancement in this direction combines the rational design of a luciferin derivative with the use of nanodelivery, resulting in a prolongation of bioluminescent detectable signal up to 2.5 days *in vivo* [19]. In this context, we developed a glutathione-sensitive nanoparticle for stimuli-responsive release of luciferin within cancer cells (Figure 3.1). The nanoconjugate bears luciferin by means of a disulfide-containing linker, which, in the presence of a reducing agent, undergoes an intramolecular cyclization reaction that results in the release of free luciferin. Apoferritin (HF<sub>n</sub>), a human protein composed of 24 subunits that self-assemble in a spherical nanoparticle, was chosen as the pilot nanoparticle for its high biocompatibility and great cancer cell selectivity.



**Figure 3.1** Schematic representation of luciferin-loaded apoferritin nanoparticles

The nanodevice designed in Figure 3.1 was thought to be a useful analytical tool at least for four concurrent reasons:

- i) the nanoconjugate is specifically addressed to cancer cells for the use of HF<sub>n</sub> that is recognized by the transferrin receptor, which results overexpressed in 98% of human tumors;
- ii) thanks to the high concentration of glutathione in tumor cell cytoplasm, free luciferin will be released only after nanoparticle internalization, making bioluminescence reaction a specific event within the tumor. These features give the nanoconjugate a potential to become a bioluminescent probe even for a single cancer cell detection, due to the target selectivity and to the signal sensitivity;
- iii) studies of nanoparticle biodistribution *in vivo* could be performed using totally transgenic animal models, avoiding the use of fluorophores that experience problems of photobleaching and background noise, or radionuclides that are usually accompanied by toxicity risks;
- iv) once the release mechanism of the nanoconstruct has been elucidated, it is possible to design similar objects with the employment of a variety of both nanoparticles and cargo molecules.

### **3.3 – Aim of the project**

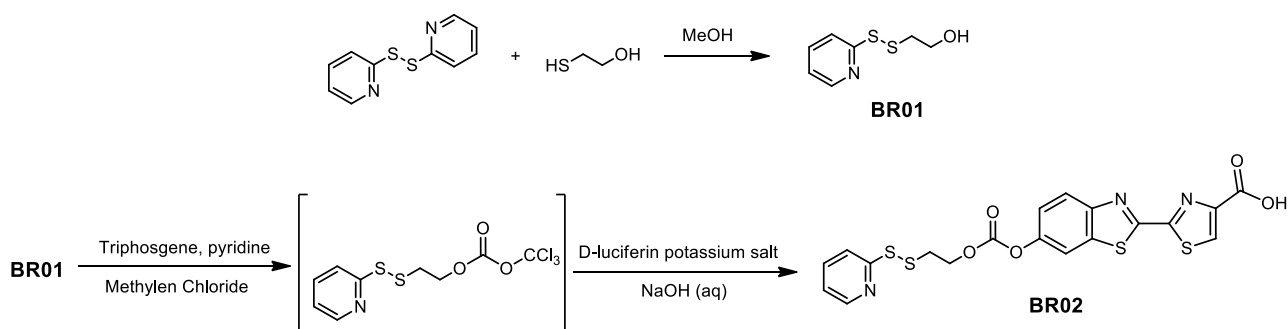
In the present PhD thesis, the aim of the project was the optimization of the synthesis of the luciferin linker and its conjugation to HF<sub>n</sub> nanoparticles (Luc-linker@HF<sub>n</sub>), with particular attention given to the determination of the conjugation efficiency and cargo loading. The Luc-linker@HF<sub>n</sub> was then tested *in vitro* to initially elucidate the bioluminescent kinetics and compare the luminous signal to the one of nanoparticle-free luciferin.

### **3.4 – Results and discussion**

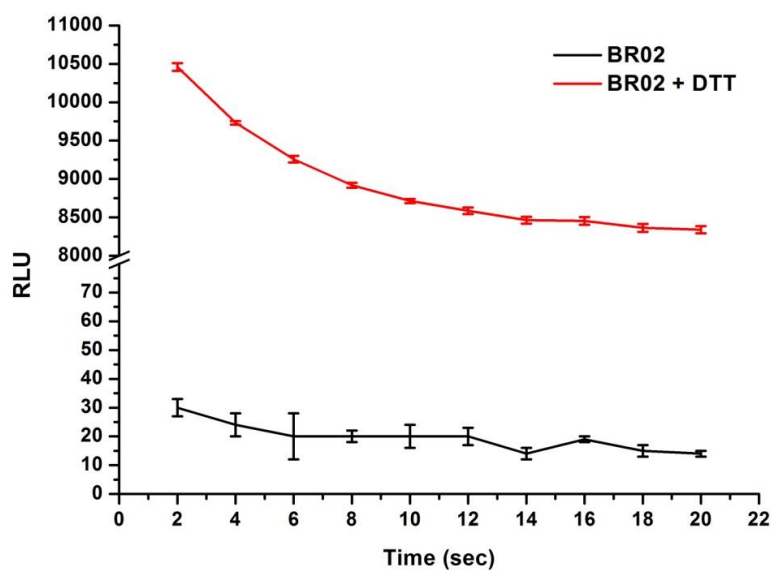
#### 3.4.1 – Synthesis of luciferin linker and conjugation to HF<sub>n</sub> nanoparticles

In order to load, transport and selectively release luciferin, a stimuli-sensitive self-immolative linker was selected. Self-immolative spacers are defined as chemical moieties undergoing rapid and spontaneous intramolecular reactions in response to cleavage of a capping or triggering unit, which, in our case, is driven by a change in glutathione concentration. For this purpose, we prepared the target luciferin derivative **BR02** [20,21], containing a disulfide bridge and a reactive carbonate, in a two-step reaction (Scheme 3.2). In the first step,

mercaptoethanol was activated by 2,2'-dithiopyridine to give compound **BR01**; afterwards, a reactive carbonate was introduced by reaction with triphosgene in the presence of pyridine and, after a phase transfer in alkaline water, D-luciferin was coupled by nucleophilic substitution, leading to the final product **BR02**.



**Scheme 3.2** Synthetic route to prepare luciferin-bearing self-immolative linker.

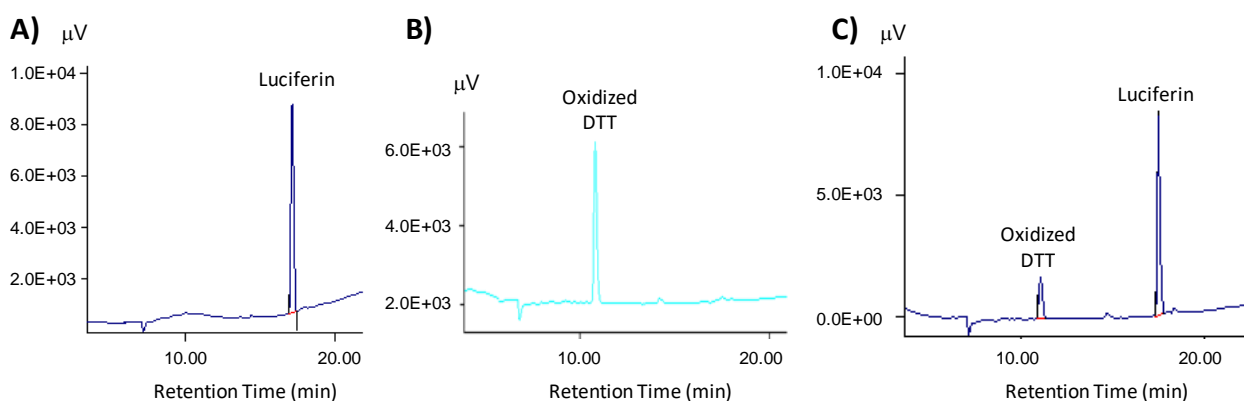


**Figure 3.2** Luminescent pattern of compound **BR02** (black) and **BR02** pretreated with DTT (red) in presence of luciferase. RLU: relative light units.

The proposed mechanism of release consists in the reduction of the disulfide bridge in the presence of a reducing agent, such as glutathione or dithiothreitol (DTT); the resulting thiolate anion would attack the proximal carbonate on the carbonyl center, leading to free luciferin and cyclic ethylene monothiol carbonate. In order to verify the mechanism, cell-free *in vitro* tests were performed (Figure 3.2). Compound **BR02** was dissolved in a saline buffer containing



ATP, a  $Mg^{2+}$  ion source and DTT as reducing agent; when the solution was incubated with luciferase, bioluminescence was detected, confirming the successful interaction between luciferin and the enzyme. To further confirm that the luminous signal was produced by the released substrate and not by native **BR02**, the same experiment was conducted without DTT. In this case, bioluminescence was not observed, even if using higher amount of the tested product. Taken together, these data highlight the capacity of our system to release luciferin in response to a specific stimulus and to provide high luminous signal in the presence of luciferase.



**Figure 3.3** RP-HPLC chromatograms of A) free luciferin, B) oxidized DTT (obtained by leaving DTT in aqueous solution for 1 month) and C) washing volumes after treatment of Luc-linker@HF<sub>n</sub> with 1 mM DTT and subsequent filtration.

After the assessment of **BR02** integrity and functioning, the luciferin linker was conjugated to HF<sub>n</sub> nanoparticles by means of free thiol groups of the cysteine residues, leading to the nanoconstruct Luc-linker@HF<sub>n</sub>. The reaction was conducted in physiological buffer without further reagents and unreacted species were simply removed by size-exclusion chromatography. Spectrophotometric analysis at 280 nm highlighted a quantitative recovery of HF<sub>n</sub> nanoparticles post-synthesis. In order to determine the conjugation efficiency and a quantification of the loaded linker, we developed a protocol based on a prior luciferin release in reductive environment, and a subsequent quantification by RP-HPLC. Hence, Luc-linker@HF<sub>n</sub> nanoparticles were first incubated with DTT to trigger luciferin release; afterwards, the products deriving from the intramolecular cyclization of the linker were separated from free HF<sub>n</sub> nanoparticles by centrifugal filtration cycles. Spectrophotometric analyses confirmed the separation of the species, giving the classical absorbance peak at 280 nm for the filtered volume and no UV absorption for the washings. The RP-HPLC

chromatogram of the latter volumes showed a peak corresponding to oxidized DTT at a retention time of 11 min, while the presence of luciferin was detected at a retention time of 17 min (Figure 3.3). Table 3.1 shows the conjugation efficiency and luciferin content corresponding to different reagent ratios used in the synthesis. Increasing the excess of **BR02** from 3 equivalents to 100, the conjugation efficiency drops dramatically but it is compensated by a remarkable gain in cargo loading, that appears 3-fold higher. The Luc-linker@HF<sub>n</sub> with the highest luciferin content was carried forward in the subsequent experiments.

**Table 3.1** Conjugation efficiency and luciferin content on Luc-linker@HF<sub>n</sub> obtained with different reagent ratios. Values were derived from the integration of chromatogram peaks at retention time of 17 min and using as reference known amounts of free luciferin eluted with the same procedure.

Reagent ratio HF <sub>n</sub> :BR02	Loading Luc/HF <sub>n</sub>		Conjugation efficiency (%) <sup>b</sup>
	nmol/mg <sup>a</sup>	molecule/molecule <sup>a</sup>	
1:3	2.19 ± 0.02	1.10 ± 0.02	35.3 ± 0.3
1:10	3.91 ± 0.43	2.00 ± 0.23	19.6 ± 2.2
1:100	5.78 ± 0.28	2.90 ± 0.01	3.0 ± 0.9

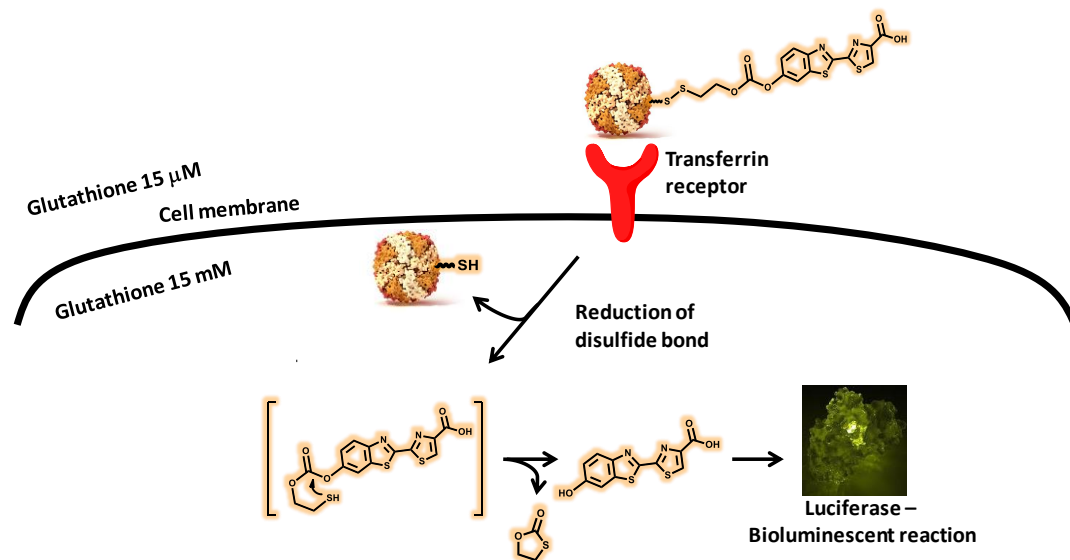
<sup>a</sup> luciferin eluted in RP-HPLC (nmol or molecule)/HF<sub>n</sub> quantity used for the test (mg or molecule)

<sup>b</sup> luciferin eluted in RP-HPLC/ luciferin in the conjugation reaction × 100

### 3.4.2 – Bioluminescence kinetic of Luc-linker@HF<sub>n</sub> *in vitro*

As aforementioned, HF<sub>n</sub> is known to be recognized by transferrin receptor (Tfr1) overexpressed in the majority of cancer cells. Thus, we hypotise that Luc-linker@HF<sub>n</sub> will be internalized in luciferase-expressing cells by a receptor-mediated endocytosis, guided by the molecular recognition between HF<sub>n</sub> and Tfr1. Once inside the cytoplasm, the glutathione - present in high concentrations - will trigger the intramolecular cyclization of the linker and the consequent luciferin release, making the bioluminescent event possible (Figure 3.4). In order to have a first confirmation of our hypotesis, the nanoformulated luciferin was tested for its bioluminescence (BLI) efficacy towards a human breast cancer cell-line (MDA-MB-231) that is known to overexpress Tfr1 (Tfr1<sup>+</sup>) and that is commercially available in its luciferase-transfected form (luciferase<sup>+</sup>). Previously experiments were conducted at the Nanomedicine Laboratory of “Luigi Sacco” Hospital (Milan): binding efficiency of fluorescent-labelled HF<sub>n</sub> towards MDA-MB-231 was demonstrated by flow cytometry, while confocal microscopy images showed a slight NP internalization at 15 min and NP abundance at 1 h. Both experiments permitted to designate 100 µg mL<sup>-1</sup> as the suitable HF<sub>n</sub> concentration to have good binding and internalization inside tested cells (unpublished data). As the internalization

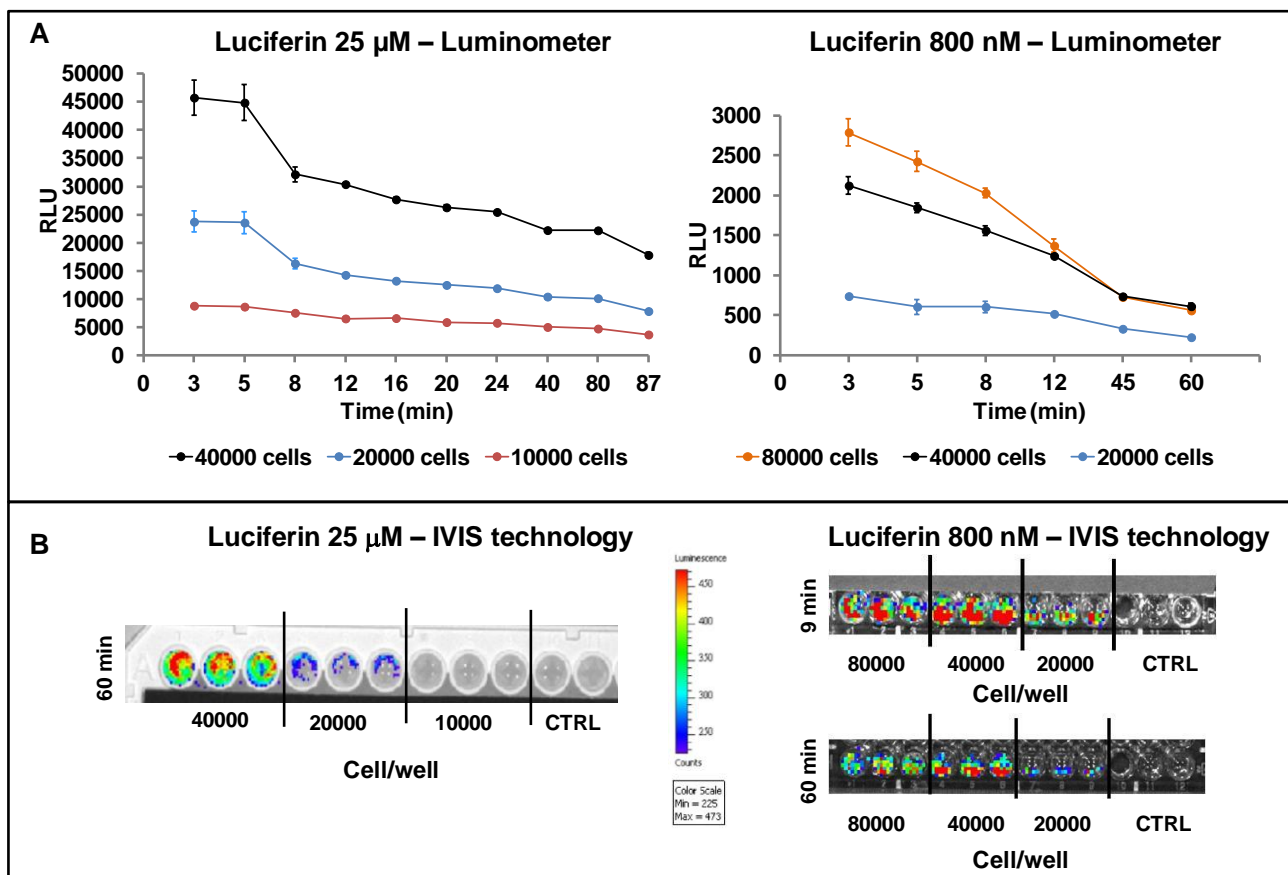
kinetic of Luc-linker@HF<sub>n</sub> is expected to be different and slower than the diffusion rate of free luciferin, a comparison between the BLI time-course of free and nanoformulated luciferin was outlined using two different analytical techniques.



**Figure 3.4** Graphical representation of the hypothesized mechanism of action: Luc-linker@HF<sub>n</sub> is recognized by transferrin receptor and internalized in cell. The glutathione reduces the disulfide bridge between HF<sub>n</sub> and the linker, triggering luciferin release. Free luciferin is now allowed to react with luciferase, producing a luminous signal.

First of all, Tfr1<sup>+</sup> and luciferase<sup>+</sup> MDA-MB-231 were seeded in two different 96-well plates at various dilutions (from 10000 to 80000 cell/well) and incubated with two diverse concentrations of free luciferin: 25 μM, that is the lowest concentration found in the literature to be used for such experiments, and 800 nM, that simulates the concentration that we should have using 100 μg mL<sup>-1</sup> of Luc-linker@HF<sub>n</sub>, considering the maximum cargo loading. Immediately after the addition of the substrate, one well-plate was monitored by luminometer, to outline a proper correlation between time and luminous signal; the other well-plate was observed by an optical imaging technique usually exploited for *in vivo* experiments, so to have a preliminary information about the possibility to detect our system with such technology. Panel A of Figure 3.5 clearly shows the sensitivity of luminometer, which permits the detection of photons produced even in presence of the lower concentration of luciferin, at least for cells seeded at 40000 cells/well. Bioluminescent signal was followed up to 85 min in case of 25 μM of substrate, while the kinetic stopped earlier (ca. 60 min) for luciferin 800 nM. IVIS technology possesses a lower sensitivity, enabling the last detection of light produced in the most populated wells (40000 cell/well) incubated with 25 μM luciferin at 60 min of incubation (Figure 3.5, B). As expectable, the analysis was more difficult with the lower substrate dose,

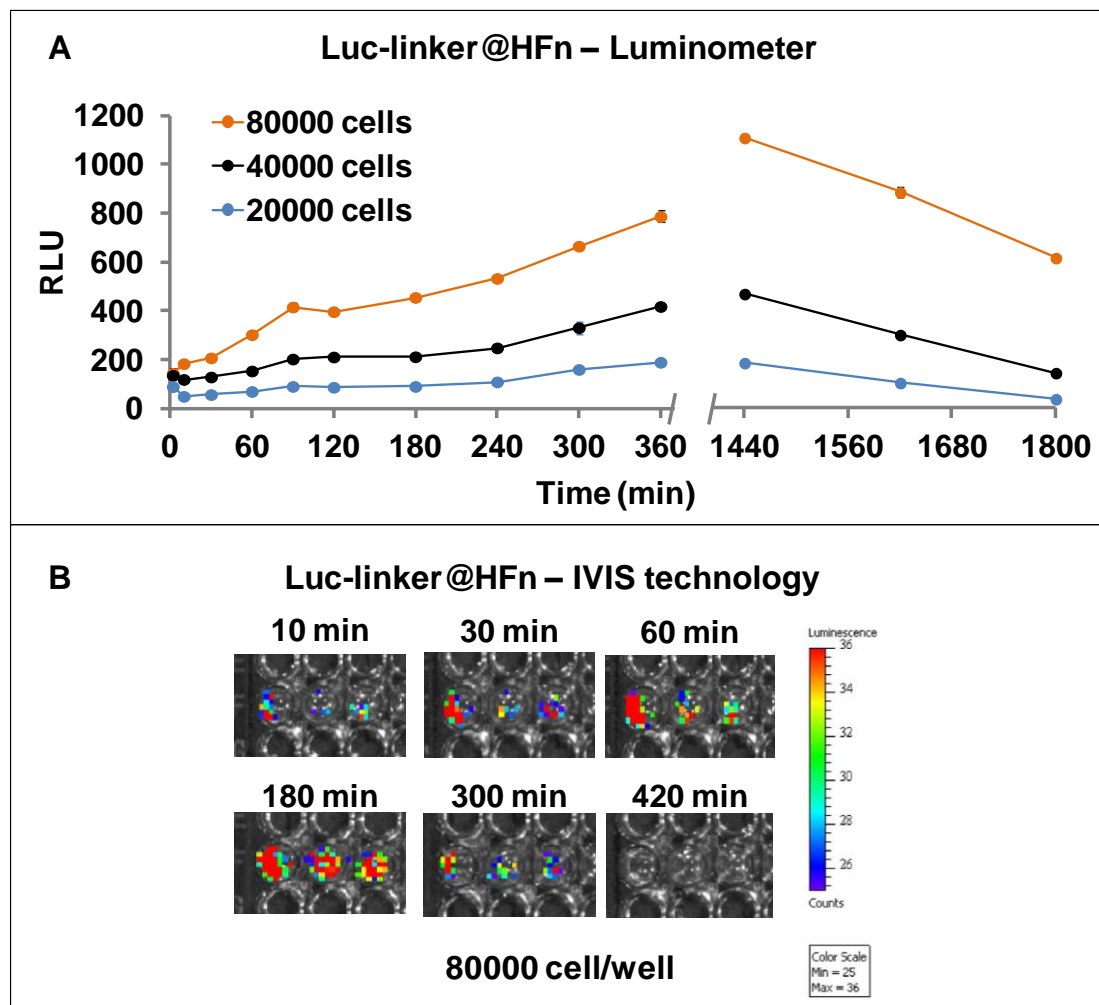
that was not able to originate a detectable BLI with the same acquisition parameters used with 25  $\mu\text{M}$  luciferin, even with higher density of seeded cells. Nevertheless, once the parameters of the acquisition system were set to amplify the detected bioluminescence, a good signal was recorded from the first minutes up to 1 h of incubation also with 800 nM luciferin (see Experimental section). 40000 cell/well proved to be the ideal cell concentration to have the best signal with IVIS camera, while in the presence of 80000 cell/well the signal got worse, suggesting an overcrowding, not amenable to luciferin diffusion.



**Figure 3.5** Bioluminescence of different amounts of Tfr1<sup>+</sup> luciferase<sup>+</sup> MDA-MB-231 cells incubated with 800 nM and 25  $\mu\text{M}$  free luciferin. A) Time-course outlined using luminometer; B) Spot analysis by IVIS technology at 60 min of incubation with luciferin 25  $\mu\text{M}$  and at 9 and 60 min of incubation with luciferin 800 nM.

Afterwards, the same experiments were performed incubating Tfr1<sup>+</sup> luciferase<sup>+</sup> MDA-MB-231 cells with 100  $\mu\text{g mL}^{-1}$  of Luc-linker@HF<sub>n</sub> (Figure 3.6). The production of light was detected with both luminometer and IVIS techniques, indicating the successful internalization of the particles inside the cells and an effective luciferin release. Nevertheless, as expected, the BLI kinetic was completely different from that observed with free luciferin, since the receptor-

mediated entrance mechanism and endosomal trafficking of the NPs delayed the interaction between luciferin and luciferase. The data collected with the luminometer show a detectable BLI over 20000 cells/well and a good correlation between the bioluminescence and the number of plated cells. Photon production increased up to 24 h and then decreased, with a signal still detectable until 30 h only in the wells containing over 40000 cells (Figure 3.6, A).



**Figure 3.6** Bioluminescence of different amounts of Tfr1<sup>+</sup> luciferase<sup>+</sup> MDA-MB-231 cells incubated with 100 µg mL<sup>-1</sup> of Luc-linker@HF<sub>n</sub> (corresponding to 580 nM luciferin). A) Time-course outlined using luminometer; B) Spot analysis by IVIS technology at different time points, using only the highest cell concentration (80000 cell/well).

Using the IVIS camera, the light was visible only for the most populated wells, employing the high detection parameter setting needed for the free luciferin 800 nM. Also this method revealed an increase of signal over time, with a maximum observed at 3 h. Then the bioluminescent events declined, with no light revealed at 7 h. These findings demonstrate the

potentiality of Luc-linker@HF<sub>n</sub> to act as a bioluminescent probe, as indicated by the successful photon detection in the exposed tumor cells. Moreover, information about the delivery system was collected: the bioluminescent kinetic of nanoformulated luciferin confirmed the receptor-mediated internalization of HF<sub>n</sub> NPs, which were able to release their cargo into the cell cytoplasm only after the period of time necessary to overcome the endocytotic pathway. Despite of these potentialities, much work can be done to improve the sensitivity of the method, mainly trying to increase the density of luciferin linker on HF<sub>n</sub> NPs.

### 3.5 – Conclusion

In the present project we aimed at developing a smart nanoformulated bioluminescent probe for the combined detection of cells or cellular mechanism and the control of the corresponding nanodelivery system fate. As a result, for their biocompatibility and cancer selectivity, HF<sub>n</sub> NPs were selected to be engineered with a self-immolative linker bearing luciferin (Luc-linker). The linker was prepared by optimizing procedures reported in the literature [20,21], leading to a stimuli-responsive molecule with a reducible disulfide bridge and a reactive carbonate moiety. In order to verify the correct luciferin release in reducing environment, cell-free *in vitro* bioluminescence tests were performed, demonstrating an abundant photon production when Luc-linker was preincubated with DTT and then reacted with luciferase, while no light emission without DTT pretreatment. Luc-linker was then attached to HF<sub>n</sub> surface, exploiting the free thiol groups of cysteine residues, with a quantitative recovery of the protein. An HPLC method was developed for the quantification of conjugation efficiency and drug loading, requiring a preliminary separation of the linker from the hosting HF<sub>n</sub> NPs. The analyses revealed that increasing HF<sub>n</sub>:Luc-linker ratio during the conjugation step resulted in a decreasing conjugation efficiency, but in a definitely augmented cargo loading. The bioluminescence kinetic of Luc-linker@HF<sub>n</sub> was then outlined *in vitro*, incubating the nanoconjugate in Tfr1<sup>+</sup> and luciferase<sup>+</sup> MDA-MB-231 breast cancer cells. Bioluminescent events were detected both by luminometer and by IVIS technology, suggesting a successful interaction between delivered luciferin and cytosolic luciferase. The profiled kinetic resulted delayed with respect to free luciferin one, confirming the receptor-mediated internalization of Luc-linker@HF<sub>n</sub> and the subsequent release of luciferin, triggered by intracellular glutathione. Taken together, these results confirm the promising utility of the nanoformulated luciferin as bioluminescent probe and encourage further synthetic optimizations to enhance the sensitivity – hence the potentiality – of the developed analytical tool.

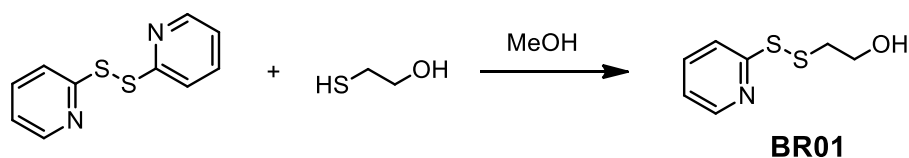
## 3.6 – Experimental section

### 3.6.1 – Solutions and buffers

- Buffer C: 5 mM MgSO<sub>4</sub>, 200 mM NaCl, 20 mM HEPES, 1 mM EDTA, pH 7.4
- Buffer D: 5 mM MgSO<sub>4</sub>, 200 mM NaCl, 20 mM HEPES, 1 mM EDTA, 2 mM ATP, pH 7.4
- Buffer E: 5 mM MgSO<sub>4</sub>, 200 mM NaCl, 20 mM HEPES, 1 mM EDTA, 2 mM ATP, 1 mM DTT, pH 7.4
- Eluent A: 0.1% TFA in water
- Eluent B: 0.1% TFA in CH<sub>3</sub>CN
- Phosphate buffered saline (PBS): 137 mM NaCl, 2.7 mM KCl, 10 mM Na<sub>2</sub>HPO<sub>4</sub>, 1.8 mM KH<sub>2</sub>PO<sub>4</sub>, pH 7.4
- PBS-EDTA: 137 mM NaCl, 2.7 mM KCl, 10 mM Na<sub>2</sub>HPO<sub>4</sub>, 1.8 mM KH<sub>2</sub>PO<sub>4</sub>, 5 mM EDTA, pH 7.4

### 3.6.2 – Synthesis of D-Luciferin linker

#### 3.6.2.1 – Synthesis of compound **BR01**

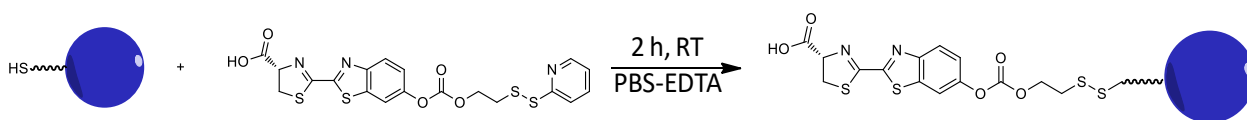


2,2'-dithiopyridine (925 mg, 4.2 mmol) was loaded into an oven dried three-necked round flask under nitrogen and dissolved in methanol (5 mL), previously purged with nitrogen. To this mixture under magnetic stirring, 2-mercaptoethanol (400  $\mu$ L, 5.6 mmol) was added dropwise. The solution turned yellow and was allowed to stir for 5 h at RT. The solvent was then removed under reduced pressure and flash chromatography was performed using 20% ethyl acetate and 80 % methylene chloride. The product was a yellow oil (80% yield) and was characterized by <sup>1</sup>H-NMR (400 MHz, CDCl<sub>3</sub>):  $\delta_{\text{H}}$  (ppm) 8.53-8.52 (doublet, 1H), 7.60-7.52 (multiplet, 1H), 7.41-7.35 (doublet, 1H), 7.18-7.15 (multiplet, 1H), 3.82-3.71 (triplet, 2H), 2.97-2.94 (triplet, 2H).





### 3.6.4 – Conjugation of D-luciferin linker to HFn nanoparticles



#### 3.6.4.1 – HFn nanoparticles preparation

HFn nanoparticles were obtained in our lab as recombinant proteins in *E. Coli* as described in Bellini et al. [22].

#### 3.6.4.2 – Conjugation of **BR02** to HFn nanoparticles (Luc-linker@HFn)

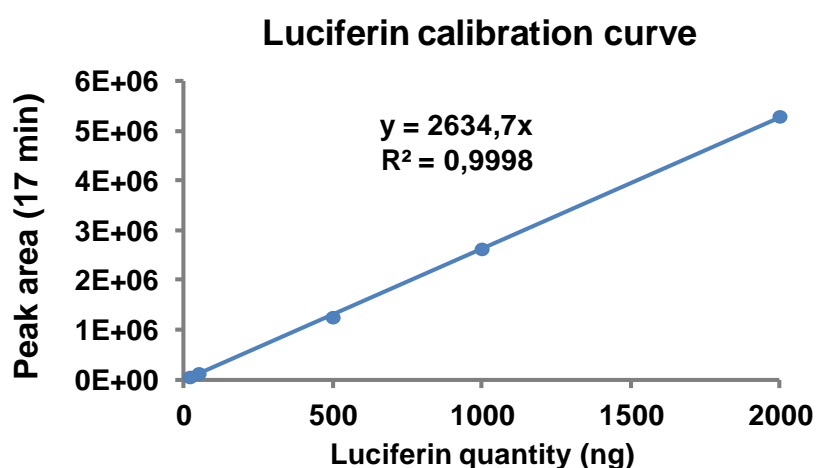
The synthesis was performed multiple times in order to set the best reagent ratio: HFn nanoparticles were kept at a concentration of  $1 \text{ mg mL}^{-1}$ , while **BR02** content was changed. HFn nanoparticles (1 mg) and the desired quantity of **BR02** were mixed in PBS-EDTA buffer (1 mL) and left under stirring 2 h at RT in darkness. The unreacted species were removed by size exclusion chromatography using a 5 mL ZEBRA spin desalting column (Thermo Fisher). The reaction crude was loaded in the column and eluted by centrifugation at 1000 rcf for 2 min. The purified Luc-linker@HFn was collected in a total volume of PBS of 1 mL. The protein recovery after purification was checked by spectrophotometric analysis at  $\lambda=280 \text{ nm}$ , using as setting parameters HFn molecular weight (509 KDa) and molar extinction coefficient at the same wavelength ( $\epsilon/1000 = 458.34 \text{ M}^{-1} \text{ cm}^{-1}$ ).

#### 3.6.4.3 – Determination of conjugation efficiency and cargo loading

Luc-linker@HFn ( $\approx 200\text{-}250 \text{ }\mu\text{g}$ ) in PBS-EDTA buffer ( $\approx 1 \text{ mg mL}^{-1}$ ) was incubated with DTT 1 mM under mild agitation (100 rpm) for 30 min in darkness. The suspension was then loaded into a centrifuge filter (Amicon ultra, Millipore) with a 100 kDa cut-off and washed thrice with ultrapure water (1700 rpm, 5 min, 4 °C), collecting both the excluded volumes and the final resuspended filtered nanoparticles. Both the filtered and the excluded volumes were analyzed by UV-visible spectroscopy using HFn setting parameters (MW=509 KDa,  $\epsilon/1000=458.34 \text{ M}^{-1} \text{ cm}^{-1}$ ) in order to check the presence of the protein. The excluded volumes were then analyzed by RP-HPLC using the following elution conditions: injected volume 20  $\mu\text{L}$ ; eluent gradient from solvent A 100% to solvent B 85% in 30 min; flow rate  $1 \text{ mL min}^{-1}$ ; UV detection at  $\lambda = 326 \text{ nm}$ . Free luciferin was eluted at about 17 min and quantified exploiting the calibration

curve previously constructed by correlating known amounts of free luciferin to the area of the peak at 17 min (Table and figure below).

Luciferin (ng)	Luciferin (pmol)	Retention time (min)	Peak area
2000	6616	17,49	5288401
1000	3308	17,35	2627160
500	1654	17,325	1257053
50	165	17,167	128489
20	66	17,117	55956



### 3.6.5 – *In vitro* tests

Tfr1<sup>+</sup> and Luciferase<sup>+</sup> MDA-MB-231 cells (purchased by PerkinElmer, Italy) were cultured in Minimum Essential Medium (MEM) supplemented with 10% fetal bovine serum, 2 mM L-glutamine, penicillin (50 UI mL<sup>-1</sup>) and streptomycin (50 mg mL<sup>-1</sup>) at 37 °C in humidified atmosphere containing 5% CO<sub>2</sub> and sub-cultured prior to confluence using trypsin/EDTA. Cell culture medium and chemicals were purchased from EuroClone. To assess bioluminescence by luminometer (GloMax multi detection system – Promega), cells were cultured on a black 96 multi-well dish (Brand) at the density of 10000-80000 cells/well and then incubated between 3 and 87 min in the presence of 800 nM or 25 μM luciferin (XenoLight D-Luciferin Potassium Salt – PerkinElmer), or between 2 and 1800 min in the presence of 100 μg mL<sup>-1</sup> Luc-linker@HF<sub>n</sub>, (580 nM D-Luciferin). To assess BLI by optical imaging (IVIS Lumina II Imaging System – Calipers Life Sciences, UK), cells were cultured on a transparent 96 multi-well dish (EuroClone) at the density of 10000-80000 cells/well. Cells incubated in the presence of 25 μM luciferin were analyzed after 60 min, using the following acquisition parameters: pixel

binning (CCD resolution) = medium, f/stop (lens aperture) = 4, exposure time = 10 sec. Cells incubated in the presence of 800 nM luciferin for 9 and 60 min, or in the presence of  $100 \mu\text{g mL}^{-1}$  Luc-linker@HF<sub>n</sub>, (580 nM D-Luciferin) between 10 and 420 min, were analyzed using the following acquisition parameters: pixel binning = large, f/stop = 1, exposure time = 15 sec.

## References

1. Contag, C. H.; Ross, B. D. It's not just about anatomy: in vivo bioluminescence imaging as an eyepiece into biology. *J. Magn. Reson. Imaging JMRI* **2002**, *16*, 378–387.
2. Cho, H.; Ackerstaff, E.; Carlin, S.; Lupu, M. E.; Wang, Y.; Rizwan, A.; O'Donoghue, J.; Ling, C. C.; Humm, J. L.; Zanzonico, P. B.; Koutcher, J. A. Noninvasive multimodality imaging of the tumor microenvironment: registered dynamic magnetic resonance imaging and positron emission tomography studies of a preclinical tumor model of tumor hypoxia. *Neoplasia N. Y. N* **2009**, *11*, 247–259, 2p following 259.
3. Hirano, T. Molecular Origin of Color Variation in Firefly (Beetle) Bioluminescence: A Chemical Basis for Biological Imaging. *Curr. Top. Med. Chem.* **2016**, *16*, 2638–2647.
4. Sadikot, R. T.; Blackwell, T. S. Bioluminescence Imaging. *Proc. Am. Thorac. Soc.* **2005**, *2*, 537–540.
5. England, C. G.; Ehlerding, E. B.; Cai, W. NanoLuc: A Small Luciferase Is Brightening Up the Field of Bioluminescence. *Bioconjug. Chem.* **2016**, *27*, 1175–1187.
6. Paley, M. A.; Prescher, J. A. Bioluminescence: a versatile technique for imaging cellular and molecular features. *Med. Chem. Commun.* **2014**, *5*, 255–267.
7. Kocher, B.; Piwnica-Worms, D. Illuminating Cancer Systems with Genetically Engineered Mouse Models and Coupled Luciferase Reporters In Vivo. *Cancer Discov.* **2013**, *3*, 616–629.
8. Chaudhuri, T. R.; Cao, Z.; Ponnazhagan, S.; Stargel, A.; Simhadri, P. L.; Zhou, T.; Lobuglio, A. F.; Buchsbaum, D. J.; Zinn, K. R. Bioluminescence imaging of non-palpable breast cancer xenografts during treatment with TRA-8, an anti-DR5 antibody and chemotherapy. *Cancer Res.* **2004**, *64*, 481–481.
9. Contero, A.; Richer, E.; Gondim, A.; Mason, R. P. High throughput quantitative bioluminescence imaging for assessing tumor burden. *Methods Mol. Biol. Clifton NJ* **2009**, *574*, 37–45.
10. Mollard, S.; Fanciullino, R.; Giacometti, S.; Serdjebi, C.; Benzekry, S.; Ciccolini, J. In Vivo Bioluminescence Tomography for Monitoring Breast Tumor Growth and Metastatic Spreading: Comparative Study and Mathematical Modeling. *Sci. Rep.* **2016**, *6*, 36173.
11. O'Farrell, A.; Shnyder, S.; Marston, G.; Coletta, P.; Gill, J. Non-invasive molecular imaging for preclinical cancer therapeutic development. *Br. J. Pharmacol.* **2013**, *169*, 719–735.
12. Shinde, R.; Perkins, J.; Contag, C. H. Luciferin Derivatives for Enhanced in Vitro and in Vivo Bioluminescence Assays†. *Biochemistry (Mosc.)* **2006**, *45*, 11103–11112.

13. Berger, F.; Paulmurugan, R.; Bhaumik, S.; Gambhir, S. S. Uptake kinetics and biodistribution of <sup>14</sup>C-d-luciferin—a radiolabeled substrate for the firefly luciferase catalyzed bioluminescence reaction: impact on bioluminescence based reporter gene imaging. *Eur. J. Nucl. Med. Mol. Imaging* **2008**, *35*, 2275–2285.
14. Harwood, K. R.; Mofford, D. M.; Reddy, G. R.; Miller, S. C. Identification of Mutant Firefly Luciferases that Efficiently Utilize Aminoluciferins. *Chem. Biol.* **2011**, *18*, 1649–1657.
15. Kim, J.-B.; Urban, K.; Cochran, E.; Lee, S.; Ang, A.; Rice, B.; Bata, A.; Campbell, K.; Coffee, R.; Gorodinsky, A.; Lu, Z.; Zhou, H.; Kishimoto, T. K.; Lassota, P. Non-Invasive Detection of a Small Number of Bioluminescent Cancer Cells In Vivo. *PLOS ONE* **2010**, *5*, e9364.
16. Mezzanotte, L.; Fazzina, R.; Michelini, E.; Tonelli, R.; Pession, A.; Branchini, B.; Roda, A. In Vivo Bioluminescence Imaging of Murine Xenograft Cancer Models with a Red-shifted Thermostable Luciferase. *Mol. Imaging Biol.* **2010**, *12*, 406–414.
17. Evans, M. S.; Chaurette, J. P.; Adams Jr, S. T.; Reddy, G. R.; Paley, M. A.; Aronin, N.; Prescher, J. A.; Miller, S. C. A synthetic luciferin improves bioluminescence imaging in live mice. *Nat. Methods* **2014**, *11*, 393–395.
18. Sun, X.; Zhao, Y.; Lin, V. S.-Y.; Slowing, I. I.; Trewyn, B. G. Luciferase and luciferin co-immobilized mesoporous silica nanoparticle materials for intracellular biocatalysis. *J. Am. Chem. Soc.* **2011**, *133*, 18554–18557.
19. Yuan, Y.; Wang, F.; Tang, W.; Ding, Z.; Wang, L.; Liang, L.; Zheng, Z.; Zhang, H.; Liang, G. Intracellular Self-Assembly of Cyclic d-Luciferin Nanoparticles for Persistent Bioluminescence Imaging of Fatty Acid Amide Hydrolase. *ACS Nano* **2016**, *10*, 7147–7153.
20. Jones, L. R.; Goun, E. A.; Shinde, R.; Rothbard, J. B.; Contag, C. H.; Wender, P. A. Releasable luciferin-transporter conjugates: tools for the real-time analysis of cellular uptake and release. *J. Am. Chem. Soc.* **2006**, *128*, 6526–6527.
21. Eiríksdóttir, E.; Langel, Ü.; Rosenthal-Aizman, K. An improved synthesis of releasable luciferin–CPP conjugates. *Tetrahedron Lett.* **2009**, *50*, 4731–4733.
22. Bellini, M.; Mazzucchelli, S.; Galbiati, E.; Sommaruga, S.; Fiandra, L.; Truffi, M.; Rizzuto, M. A.; Colombo, M.; Tortora, P.; Corsi, F.; Prosperi, D. Protein nanocages for self-triggered nuclear delivery of DNA-targeted chemotherapeutics in Cancer Cells. *J. Controlled Release* **2014**, *196*, 184–196.

# **APPENDED PAPERS**

ORIGINAL RESEARCH

Radiolabeled nanosilica for breast cancer imaging

P. Rainone<sup>‡</sup>, B.Riva<sup>‡</sup> et al

## Development of <sup>99m</sup>Tc-Radiolabeled Nanosilica for Targeted Detection of HER2-Positive Breast Cancer

Paolo Rainone,<sup>1,‡</sup> Benedetta Riva,<sup>2,‡</sup> Sara Belloli,<sup>1,\*</sup> Francesco Sudati,<sup>3</sup> Marilena Ripamonti,<sup>1</sup> Paolo Verderio,<sup>2</sup> Miriam Colombo,<sup>2</sup> Maria Carla Gilardi,<sup>1</sup> Rosa Maria Moresco,<sup>4</sup> Davide Prospero<sup>2,\*</sup>

<sup>1</sup> Institute of Molecular Bioimaging and Physiology of CNR, Via Fratelli Cervi 93, 20090 Segrate, Italy

<sup>2</sup> NanoBioLab, Dipartimento di Biotecnologie e Bioscienze, Università di Milano-Bicocca, Piazza della Scienza 2, 20126 Milano, Italy

<sup>3</sup> PET and Nuclear Medicine Unit, San Raffaele Scientific Institute, Via Olgettina 60, 20132 Milan, Italy.

<sup>4</sup> Department of Medicine and Surgery, University of Milano-Bicocca, Via Cadore 48, 20900 Monza, Italy.

\*Sara Belloli, Institute of Molecular Bioimaging and Physiology of CNR, Via Fratelli Cervi 93, 20090 Segrate, Italy; Phone: +39 02 26433640, Fax: +39 0226432717, Email: [belloli.sara@hsr.it](mailto:belloli.sara@hsr.it)

\*Davide Prospero, NanoBioLab, Dipartimento di Biotecnologie e Bioscienze, Università di Milano-Bicocca, Piazza della Scienza 2, 20126 Milano, Italy. Phone: +39 02 64483302, Fax: +39 02 64483565, Email [davide.prosperi@unimib.it](mailto:davide.prosperi@unimib.it)

**Abstract:** The human epidermal growth factor receptor 2 (HER2) is normally associated to a highly aggressive and infiltrating phenotype in breast cancer lesions with propensity to spread into metastases. In clinic, the detection of HER2 in primary tumors and in their metastases is currently based on invasive methods. Recently, nuclear molecular imaging techniques, including PET and SPECT, allowed the detection of HER2 lesions *in vivo*. We have developed a <sup>99m</sup>Tc-radiolabeled nanosilica system, functionalized with a trastuzumab half-chain, able to act as drug carrier and SPECT radiotracer for the identification of HER2-positive breast cancer cells. To this aim, nanoparticles functionalized or not with trastuzumab half-chain, were radiolabeled using the <sup>99m</sup>Tc-tricarbonyl approach and evaluated in HER2 positive and negative breast cancer models. Cell uptake experiments, combined with flow cytometry and fluorescence imaging, suggested that active targeting provides higher efficiency and selectivity in tumor detection compared to passive diffusion, indicating that our radiolabeling strategy did not affect the nanoconjugate binding efficiency. *Ex vivo* biodistribution of <sup>99m</sup>Tc-nanosilica in a SK-BR-3 (HER2<sup>+</sup>) tumor xenograft at 4 h post-injection was higher in targeted compared to non-targeted nanosilica, confirming the *in vitro* data. In addition, viability and toxicity tests provided evidence on nanoparticle safety in cell cultures. Our results encourage

further assessment of silica  $^{99m}\text{Tc}$ -nanoconjugates to validate a safe and versatile nanoreporter system for both diagnosis and treatment of aggressive breast cancer.

**Keywords:** SPECT; targeted radionuclide imaging; silica nanoparticles; TZ-half chain conjugation;  $^{99m}\text{Tc}$ -Tricarbonyl radiolabeling

## Introduction

Breast cancer (BC) is the most common tumor in women, being the second cause of death due to cancer.<sup>1</sup> BCs overexpressing the human-epidermal-growth-factor-receptor-2 (HER2) account for 30% of invasive breast tumors and are associated with an aggressive biological behavior translating to poorer clinical outcomes.<sup>2</sup> The development of trastuzumab (TZ), a recombinant humanized monoclonal antibody that recognizes the extracellular domain of the HER2 protein, has dramatically altered the natural history of HER2-positive (HER2<sup>+</sup>) BC and ranks among the most significant advances in cancer therapeutics.<sup>3,4</sup> Nevertheless, in order to have a benefit from TZ or related therapies, the detection of HER2 expression remains a fundamental issue. Nowadays, HER2 expression is evaluated in post-surgery or bioptic specimen by immunohistochemistry (IHC) or fluorescence in-situ hybridization (FISH)<sup>5</sup> on primary lesion. Molecular imaging techniques as positron emission tomography (PET) and single photon emission computed tomography (SPECT) allow the *in vivo* detection of molecular targets during tumor progression and diffusion.<sup>6</sup> These radionuclide-based imaging techniques can be exploited to visualize and quantify the presence/absence of biological markers by means of specific radiolabeled probes, administered at tracer dose.<sup>7</sup> Hence, these techniques may allow the assessment of HER2 expression both in primary and secondary lesions not amenable to biopsy.<sup>8</sup> Among the radionuclides currently used in nuclear medicine for radiolabeling,  $^{99m}\text{Tc}$  offers the advantage of safety and easy availability thanks to the presence of clinical grade generators. In addition, due to its chemical properties, it can be coordinated in a stable oxidation state by bi- and tridentate ligands represented either by small functional linkers, such as hydrazinonicotinic acid<sup>9</sup> and nitrilotriacetic acid,<sup>10</sup> or by aminoacidic residues, such as histidine and cysteine.<sup>11</sup> Recent advances in nanobiotechnology have led to the development of nanoparticles (NPs) that are able to host various functionalities and to be loaded with therapeutic molecules, hence making it possible to have simultaneous diagnosis and treatment of human cancers (theranostics).<sup>12</sup> Significant advantages are offered by the use of NP systems compared to direct treatment administration. First, the delivery of cytotoxic agents to cancer cells allows to decouple the side effects of systemic chemotherapy from the therapeutic effects, getting high drug bioavailability at the tumor site,<sup>13</sup> improved therapeutic efficiency and minimal influence on normal cells.<sup>14</sup> Moreover, it is possible to label the NPs with radioactive and/or fluorescent probes for imaging detection, without affecting the therapeutic activity, while gaining high signal-to-background ratio.<sup>15</sup> NPs can easily permeate the tumor vasculature and remain in tumors owing to the enhanced permeability and retention (EPR) effect,<sup>16</sup> but this passive diffusion is not enough to improve the selectivity in the NPs interaction with cancer cells.<sup>17</sup> Recently, various ligands that can specifically bind to receptors overexpressed in cancer cells, including peptides and antibodies, have been co-engineered with smart nanomaterials for the design and construction of novel drug delivery systems and targeted diagnostic probes.<sup>18,19</sup> Silica NPs (SiNPs) possess high biocompatibility and their functionalization with monoclonal antibodies (e.g., TZ for



HER2<sup>+</sup> BC) can be a useful tool for both tumor imaging and targeted chemotherapy.<sup>20</sup> In addition, these NPs are intrinsically hydrophilic, easy and inexpensive to prepare and can be chemically modified in a straightforward manner. SiNPs are optically transparent in the near-infrared (NIR), visible and ultraviolet regions,<sup>21</sup> which is particularly favorable for *in vivo* imaging. For all these reasons, SiNPs have been recently employed as detection probes in imaging studies, including PET/SPECT, MRI and/or fluorescence (mostly NIRF) imaging, and as nanocarriers for the treatment of several types of cancer in animal models. SiNPs have been differently synthesized and functionalized to target specific tumor phenotypes (*e.g.*, colon, breast, gut) or associated features (*e.g.*, neoangiogenesis).<sup>22-24</sup> In the present study, we explored the use of multifunctional <sup>99m</sup>Tc SiNPs for early detection of HER2<sup>+</sup> BC lesions using a novel radiolabeling approach. Spherical SiNPs (hydrodynamic size ≈ 100 nm) were engineered with anti-HER2 monoclonal antibody in the form of a TZ half-chain (Hc-TZ) and radiolabeled employing <sup>99m</sup>Tc for SPECT imaging. SiNPs were also filled in with the fluoresceine isothiocyanate (FITC) dye to allow for NP detection by fluorescence microscopy. The aim of this work was to investigate the contribution offered by active targeting to the distribution of NPs in solid BC lesion and in cell internalization, in comparison to nonspecifically targeted SiNPs. Moreover, we set up and tested a radiolabeling procedure that allow us to follow *in vivo* tumor uptake and organ kinetics distribution of nanosilica, using nuclear medicine techniques. This SiNPs system could be potentially used to develop a theranostic nanosystem combining noninvasive detection with an effective treatment for HER2<sup>+</sup> mammary cancer.

## Material and methods

### Chemicals

All reagents and solvents were purchased from Sigma-Aldrich (St. Louis, MO), Rapp Polymere (Tuebingen, Germany), Riedel-de Haën (Seelze, Germany) and Fluka (St. Gallen, Germany) and used as received without further purification. Trastuzumab antibody was purchased by Genentech (Herceptin®, Genentech, USA) and used after dialysis in PBS at 4 °C on a Slyde-A-Lyzer dialysis cassette (Thermo Fisher Scientific, USA) with a 7 kDa cut-off. Ultrasounds were generated by S15H Elmasonic Apparatus (Elma, Singen, Germany).

### Synthesis of IPTES-NTA complex

IPTES (2 μL) was mixed with a solution of NTA (2 mg) in 200 μL of deionized water:ethanol 9:1. The reaction was left under stirring for 2 h at room temperature (RT) and the complex was used immediately after preparation.

### Preparation of trastuzumab half-chain

Cysteamine (28 mM) was dissolved in a reaction buffer (20 mM HEPES, 5 mM EDTA, pH 7.2, 1 mL) and dialyzed trastuzumab (1 mg) in PBS, pH 7.2, was added. The solution was incubated under gentle stirring at 37 °C for 90 min. The reaction was cooled to RT and purified using a Sephadex PD10 column. Trastuzumab half-chain was used immediately after purification.

## **Synthesis of fluorescent core-shell silica NPs**

Monodisperse fluorescent silica nanospheres were obtained by Stöber synthesis. Briefly, to a  $\text{NH}_4\text{OH}$  solution in water (1.827 g, 0.58 M), dry ethanol was added to reach a total volume of 50 mL and the mixture was mixed under magnetic stirring. To the above solution, TEOS (1.990 mL, 0.17 M) and APTMS-FITC complex (1 mL)<sup>25</sup> were rapidly added and the reaction was stirred for 20 h at RT in the darkness. The solvent was then evaporated under reduced pressure and deionized water was added to give a final particle concentration of 10 mg/mL (concentration determined by drying 1 mL of NPs suspension at 100 °C). To the SiNPs suspension, L-arginine (0.5 mg/mL) was added and the solution was equilibrated to 70 °C for 10 min. Next, TEOS (765  $\mu\text{L}$ ) was slowly added and the reaction was left under mild stirring at 70 °C overnight in the darkness. The resulting core-shell NPs were washed thrice (20000 rcf, 20 min) and redispersed with deionized water to a final concentration of 10 mg/mL.

## **Synthesis of SiNP-NTA-TZ**

*Step 1. Amination and IPTES-NTA conjugation to core-shell NPs.* To a desired amount of core-shell NPs, glacial acetic acid (5.25  $\mu\text{mol}/\text{mg}$  of NPs), IPTES-NTA (4 nmol/mg of NPs) and APTMS (1.72  $\mu\text{mol}/\text{mg}$  of NPs) were added in sequence. The reaction was left under vigorous stirring for 2 h, after which the aminated NPs were washed thrice with ultrapure water and twice with 20 mM Hepes buffer, pH 9, and redispersed in the same buffer (10 mg/mL) for further functionalization. *Step 2. Introduction of PEG-OMe.* To the NPs suspension in Hepes, MS(PEG)<sub>4</sub> was added in an equimolar amount with respect to the surface amine functionalities assessed by ninhydrin assay. The reaction was left under stirring 2 h, after which the NPs were washed (20000 rcf, 20 min) twice with ultrapure water and twice with 20 mM Hepes buffer, pH 7.4, and redispersed in the same buffer for next steps. *Step 3. Introduction of PEG-Mal.* SM(PEG)<sub>8</sub> was added to the NPs suspension in a 5-fold molar excess with respect to the unreacted surface amine functionalities assessed by ninhydrin assay. The reaction was left under stirring 2 h, after which the NPs were washed once with ultrapure water and then redispersed in 20 mM Hepes buffer, pH 7.4. *Step 4. TZ half-chain coupling.* To the NPs suspension, the previously prepared TZ half-chain was added (10  $\mu\text{g}/\text{mg}$  of NPs) and the reaction was left under gentle stirring for 2 h. After the reaction, the NPs were washed (16000 rcf, 20 min, 4 °C) once with 20 mM Hepes, pH 7.4 and resuspended in the same buffer. *Step 5. Saturation of free maleimido-groups.* To the NPs suspension, MT(PEG)<sub>4</sub>, (0.5  $\mu\text{g}/\text{mg}$  of NPs) was added and the reaction was left under stirring 1 h, after which the NPs were washed (16000 rcf, 20 min, 4 °C) thrice with 20 mM Hepes, pH 7.4 and resuspended in 1 mM  $\text{NiCl}_2$ , pH 8. *Step 6. Nickel chelation to NTA.* The NPs were incubated under stirring in the  $\text{NiCl}_2$  buffer 1 h, and then washed (16000 rcf, 20 min, 4 °C) twice with 20 mM Hepes pH 7.5 and resuspended in the same buffer. Each sample of NPs was analyzed by UV-visible spectroscopy and absorbance values were taken at the maximum absorbance peak of FITC ( $\lambda = 485 \text{ nm}$ ). Those values were used to derive the sample concentration by means of a calibration curve previously set up by known concentrations of core-shell NPs.

## ***Synthesis of SiNP, SiNP-TZ and SiNP-NTA***

The other NPs used in this study were synthesized as described in the previous paragraph, avoiding some steps: in particular, the conjugation of IPTES-NTA, step 4 and step 6 for SiNP, the conjugation of IPTES-NTA and step 6 for SiNP-TZ, step 4 for SiNP-NTA.

## ***Determination of amino groups: ninhydrin assay***

Our protocol was adapted from a standard method described in the literature.<sup>26</sup> Briefly, aminated silica NPs (1 or 2 mg in 400  $\mu$ L of dry ethanol) were incubated with 100  $\mu$ L of ninhydrin stock solution (4 mg/mL in dry ethanol). The reaction was heated at 60 °C for 1 h. After cooling to RT, NPs were separated from the supernatant by centrifugation (20000 rcf) and an aliquot of the particle-free blue supernatant read with UV-Vis spectrophotometer at 570 nm. A standard calibration curve was created using ethanolamine in a concentration range between 0–3 mM in dry ethanol.

## ***NPs characterization***

Dynamic light scattering (DLS) measurements were performed with Zetasizer Nano ZS ZEN3600 (Malvern Instruments Ltd, Worcestershire, UK), equipped with a He-Ne laser ( $\lambda = 632.8$  nm) working at 4 mW. A disposable cuvette with an optical length of 1 cm was used and scattered light was collected at 173°. The samples were prepared with an average concentration of 100  $\mu$ g/mL in ultrapure water, and they were allowed to equilibrate at 25 °C for 30 s before the analysis. The hydrodynamic diameter was derived using Stokes-Einstein equation, considering a viscosity of the medium of 0.8872 cP. The results are reported as z-average.  $\zeta$ -potential measurements were performed with the same instruments, analyzing the electrophoretic light scattering of samples.  $\zeta$ -potential values were calculated by the Zetasizer Software basing on electrophoretic mobility and considering a viscosity of 0.8872 cP and a dielectric constant of 78.5. Samples were prepared with an average concentration of 100  $\mu$ g/mL in 1 mM NaCl and they were allowed to equilibrate at 25 °C for 30 s before the analysis. UV-vis spectra were recorded by Nanodrop 2000C spectrophotometer (Thermo Fisher Scientific, Wilmington, Germany) in a range of wavelengths from 190 to 600 nm. The size and morphology of SiNP, SiNP-TZ, SiNP-NTA and SiNP-NTA-TZ were obtained using a TEM (HT7700; Hitachi). Briefly, 25  $\mu$ M of each sample was prepared in water and then 5.0  $\mu$ L of each sample was dropped onto the copper grids and air-dried at 42 °C.

## ***Cell culture and animal models***

All reagents and solvents were purchased from Sigma-Aldrich (St. Louis, MO) and Invitrogen Corp (Carlsbad, CA). The uptake of silica nanoparticles (SiNP and SiNP-TZ) was studied using SK-BR-3 (HER2<sup>+</sup>) and MDA-MB-468 (HER2<sup>-</sup>) cell lines, obtained from ICLC Animal Cell Lines Database - IST Genova (IT). Toxicity assay was also performed using MCF-10A (non-transformed mammary epithelial cells line) purchased from

American Type Culture Collection (ATCC; USA). MDA-MB-468 and SK-BR-3 cells were maintained in Dulbecco's Modified Eagles Medium (Sigma), high glucose, supplemented with 5% Pen/Strep, 10% heat-inactivated fetal bovine serum (Euroclone) and 2 mM L-glutamine. MCF-10A cells were cultured in Advanced DMEM medium (GIBCO) containing 10% heat-inactivated foetal bovine serum, 2 mM L-glutamine, 100 U/mL penicillin and 100 mg/mL streptomycin, 10 µg/mL Insulin (Sigma), 20 ng/mL epidermal growth factor (EGF; Sigma) and 0.5 µg/mL Hydrocortisol (Sigma). Female Balb/c nude mice were obtained from the ENVIGO RMS S.r.l. Italy. Animal experiments were carried out in compliance with the institutional guidelines for the care and use of experimental animals (IACUC), which have been notified to the Italian Ministry of Health and approved by the Ethics Committee of the San Raffaele Scientific Institute. Balb/c nude mice with the age of 7–8 weeks and weight of 24–26 g were maintained under specific pathogen free condition. To obtain SK-BR-3 tumor models, about  $5 \times 10^6$  cells in 200 µL mixed solution (serum-free RMPI-1640 medium and matrigel at the volume ratio of 1:1) were injected under the right shoulder. Calipers were used to measure tumor volume (mm<sup>3</sup>) 2 times per week and mice weight was recorded. Mice were randomized when tumor volumes reached an average of 100 mm<sup>3</sup>.

### ***In vitro binding efficiency and selectivity of SiNPs by flow cytometry***

SK-BR-3 cells (HER2<sup>+</sup>,  $3 \times 10^5$ ) were incubated with 0.5 µg/mL of either SiNP, SiNP-TZ, SiNP-NTA or SiNP-NTA-TZ dispersed in serum free-DMEM. After different incubation times (20 min, 1 h, 4 h, 24 h), cells were washed twice with PBS and harvested in FACS tubes.  $10^5$  events were acquired for each analysis on FACS Calibur flow cytometer (Becton Dickinson) exploiting FITC emission (green fluorescence). Both the percentage of the fluorescent cells relative to the control (untreated cells) and the mean fluorescent intensity of the fluorescence-positive cells were taken into account. The same experiment was performed with MDA-MB-468 cell line (HER2<sup>-</sup>) as a negative control. The results were analyzed using FlowJo software.

### ***In vitro fluorescence imaging of non-radiolabeled SiNPs***

SK-BR-3 (HER2<sup>+</sup>,  $5 \times 10^4$ ) and MDA-MB-468 (HER2<sup>-</sup>,  $5 \times 10^4$ ) cells were grown on glass coverslip incubated with 0.025 mg of either SiNP, SiNP-TZ, SiNP-NTA or SiNP-NTA-TZ dispersed in cell culture media. After 20 min, 1 h, 4 h and 24 h of incubation at 37 °C (humidified atmosphere, 5% CO<sub>2</sub> air), the medium was removed and cells were washed three times with PBS. The samples were fixed with methanol (at -20 °C for 30 min) before fluorescence analysis; cell nuclei were counterstained by Hoechst (Life Science) 1 µg/mL. The specific uptake of SiNPs in both cell lines was visualized by fluorescence microscopy (Nikon Eclipse 80i).

### ***In vitro toxicity assay***

*In vitro* cytotoxicity of the SiNPs was tested on SK-BR-3 (HER2<sup>+</sup>), MDA-MB-468 (HER<sup>-</sup>) and MCF10A (non-transformed mammary epithelial) lines through MTT assay, and by viable cell counting on HER2 positive and negative cell lines.

During MTT test, both cell lines were seeded in 96-well plates (Corning, USA) at a density of  $5 \times 10^3$  cells per well and incubated for 48 h. The suspensions of SiNP, SiNP-TZ, SiNP-NTA or SiNP-NTA-TZ were diluted in culture medium at 50  $\mu\text{g}/\text{mL}$ . The cell culture medium was then removed and replaced by 100  $\mu\text{L}$  of fresh medium containing NPs. The cells were incubated for 1 h, 4 h, 24 h and 48 h at 37 °C in a humidified atmosphere, 5%  $\text{CO}_2$  air. After the above times, medium was removed and 100  $\mu\text{L}$  of MTT (5 mg/mL in PBS) was added to each well. After 3 h, the culture medium containing MTT solution was removed. 100  $\mu\text{L}$  of SDS in 0.01 M HCl solution was added to each well to dissolve the formazan crystals and then plates were analyzed using a microplate reader (SPECTROstar Omega - BMG LABTECH) at 570 nm.

During the viable cell counting experiments, NPs were incubated as described for MTT test. The medium was removed from the samples and the cells were suspended in PBS 0.1 M ( $5 \times 10^5$  cells/mL). 10  $\mu\text{L}$  of 0.4% Trypan blue was incubated for 3 min with the cell suspension (1:1), and then the mix was loaded on the Thoma chamber BLAUBRAND (Sigma-Aldrich, Italy) for the counting of the unstained (viable) and stained (nonviable) cells.

Cell viability was expressed in both experiments by comparing the treated samples to cells incubated with normal culture medium considered as 100% survival rate [% viability = (treated cells / control cells)  $\times$  100].

## ***Protocol for radiolabeling of SiNPs***

### **Preparation of $[\text{}^{99\text{m}}\text{Tc}(\text{CO})_3]^+$**

The Isolink kit (Paul Scherrer Institute-Switzerland) to prepare the labeling precursor ( $[\text{}^{99\text{m}}\text{Tc}(\text{H}_2\text{O})_3(\text{CO})_3]^+$ ) contained the following lyophilized ingredients: 8.5 mg sodium tartrate, 2.85 mg sodium tetraborate decahydrate, 7.15 mg of sodium carbonate and 4.5 mg sodium boranocarbonate. Freshly eluted  $^{99\text{m}}\text{TcO}_4^-$  from a commercial General Electric generator (approximately 2 GBq) in 1 mL saline buffer was added to the kit vial and incubated at 100 °C for 20 min. The vial was then allowed to cool to RT and the solution neutralized by adding stepwise 1 M HCl to pH approximately 7 and checked on pH paper (Merck). The radiochemical purity (RCP) of the product was analyzed by HPLC and was up 95%.

### **$[\text{}^{99\text{m}}\text{Tc}(\text{CO})_3]^+$ -His-Tag prelabeling**

An hexa-His-Tag peptide was prelabeled with  $[\text{}^{99\text{m}}\text{Tc}(\text{CO})_3]^+$ . Conjugation of the hexa-His-Tag was almost quantitative and was performed by mixing 38  $\mu\text{L}$  of peptide solution (5 mg/mL in HEPES buffer pH 7.4) to the  $[\text{}^{99\text{m}}\text{Tc}(\text{CO})_3(\text{OH}_2)_3]^+$  precursor solution. The solution mixture was incubated at RT under stirring for 60 min and then the %RCP was checked. The labeling yield was assessed by HPLC. Radiochemical purity was up 95%.

### **Conjugation of $[\text{}^{99\text{m}}\text{Tc}(\text{CO})_3]^+$ -His-Tag to SiNP-NTA**

The  $[\text{}^{99\text{m}}\text{Tc}(\text{CO})_3]^+$ -His-Tag solution was added to 500  $\mu\text{L}$  of SiNP-NTA NPs (6.7 mg/mL, 4 nmol NTA/mg SiNPs). The solution mixture was incubated at RT under stirring for 2.5 h and then the % RCP was checked. The solution was shaken for about 1 min over a vortex mixer and then centrifuged for 15 min at 18000 rpm.

Supernatant solution was withdrawn and the corresponding radioactivity was counted. The pellet was washed with Hepes buffer and centrifuged three times. After the measurement of radioactivity of total supernatant and pellet the %RCP was 42%.

## **Conjugation of [<sup>99m</sup>Tc(CO)<sub>3</sub>]<sup>+</sup>-His-Tag to SiNP-NTA-TZ**

The [<sup>99m</sup>Tc(CO)<sub>3</sub>]<sup>+</sup> His-Tag solution was added to 500 μL of SiNP-NTA-TZ NPs (8.6 mg/mL, 4 nmol NTA/mg SiNPs). The solution mixture was incubated at RT under stirring for 2.5 h and then the % RCP was checked as above described and it was 23.8%.

## **Quality control**

The chemical and radiochemical purity of each step of the synthesis was performed using a HPLC Akta system equipped with radiochemical flow counter (Bioscan). For HPLC analysis of the radiolabeled <sup>99m</sup>Tc-tricarbonyl core and <sup>99m</sup>Tc-tricarbonyl-hexa-His peptide a Thermo Scientific BDS reverse-phase column (250 × 4.6) was used with a flow of 1.2 mL/min and a linear triphasic gradient of 2% B (MeOH ) with A (0.1% TFA) from 0 to 10', 2% C (CH<sub>3</sub>CN 50% + 0.1% TFA) with A from 10 to 18'. Absorbance was detected at 220 nm. The radiochemical purity of the [<sup>99m</sup>Tc]-(CO)<sub>3</sub>-SiNPs was determined by ascending instant thin-layer chromatography (ITLC) with silica gel-coated fiberglass sheets (Pall Life Sciences, Pall Corporation) using physiological saline as the mobile phase.

## ***In vitro uptake of radiolabeled SiNPs***

SK-BR-3 (HER2<sup>+</sup>) and MDA-MB-468 (HER2<sup>-</sup>) cells were cultured at a density of 5 × 10<sup>4</sup> cells per well in 24-well plastic dishes (Corning, USA) for 48 h. Cell plates were aspirated and 0.5 ml of DMEM supplemented with 10% FBS solution was added to each plate. Either <sup>99m</sup>Tc-labeled SiNP-NTA and SiNP-NTA-TZ suspensions (1 μCi/mL) were added to the plates in 0.5 mL volumes. The cells were then incubated at 37 °C for 1 h, 4 h and 24 h in a humidified atmosphere, 5% CO<sub>2</sub> air (three wells per conditions). After specific periods, the DMEM NP suspensions were removed and the cells were washed with 300 μL of PBS. The PBS solution was removed and the cells were extracted using 200 μL of 0.05% Trypsin-EDTA (1×) solution for 10 minutes. The radioactivity of the cells and of each removed solution were then measured using a γ-counter (LKB Compugamma CS 1282). The percentage of radioactivity in cells over the total radioactivity for each plate was calculated.

## ***Ex vivo biodistribution and fluorescence imaging of <sup>99m</sup>Tc-SiNPs in tumor***

<sup>99m</sup>Tc-labeled SiNPs were evaluated in two experimental groups of Balb/c nude mice. Mice in both groups were anesthetized with Zoletil (25 mg/kg of body weight) injected intraperitoneal, with additional supplemental anesthetic as needed. Two groups of 12 mice were injected in a tail vein with 100 μL of a solution containing <sup>99m</sup>Tc-labeled SiNP-NTA-TZ or <sup>99m</sup>Tc-labeled SiNP-NTA (1 mCi/mL, pH~7.4). Additional

aliquot (0.1 mL) of both radioactive solution was diluted 1:10, 1:100 and 1:1000 and used to calculate the standards curve. Four animals per experimental point were sacrificed (at 4 h, 6 h and 24 h, post-injection) under general anesthesia. Tumor and a sample of muscle were removed and placed in counting vials for counting and weighing. Tissue samples and standards were placed in a  $\gamma$ -counter (LKB Compugamma CS 1282) and counts corrected for physical decay. The radioactivity concentration in tumor was calculated as percentage of injected dose per gram of tissue (%ID/g) and expressed as tumor to muscle ratio.

After counting, tumors were fixed with 4% paraformaldehyde for 4 h and embedded in OCT mounting medium (Sakura Finetek, Torrance, CA), to prepare frozen sections. For immunofluorescent staining, tumor sections (10  $\mu$ m) were rinsed with PBS and blocked with 5% BSA for 60 min followed by incubation with primary antibody (rabbit anti- $\beta$ -Actin, diluted 1:50; Sigma Aldrich) overnight at 4 °C. The day after, tumor sections were washed for 5 min three times with PBS. Sections were then incubated with secondary antibody (Alexa Fluor488-labeled goat anti-rabbit IgG, diluted 1:200; Sigma Aldrich) for 60 min at RT. After a rinse with PBS, they were incubated with 4-6-diamidino-2-phenylindole (DAPI) for 5 min. Finally, sections were sealed with anti-fluorescence quenching agent (Beyotime) and observed by fluorescence microscopy (Nikon Eclipse 80i).

## Results

### *Synthesis and characterization of SiNPs*

Thanks to their versatility and robust chemistry, SiNPs are promising candidate to be used as nuclear medicine imaging probes.<sup>27</sup> In our study, monodisperse 50 nm spherical SiNPs were chosen as starting material to generate biocompatible multifunctional nanoconjugates. Firstly, in order to have a fluorescent detectable carrier, the dense core of the SiNPs was loaded with a fluorophore, which was protected by an external denser silica shell necessary to prevent the undesired cargo release and limit the dye bleaching that often leads to misleading optical artifacts.<sup>25</sup> The uniform fluorescent core was obtained by a hydrolysis-condensation reaction of a mixture of TEOS and previously prepared APTMS-FITC complex<sup>255</sup> following a Stöber method in an ethanolic ammonia solution. A subsequent phase transfer to ultrapure water was followed by a biosilicification step catalyzed by L-arginine to create a uniform 5 nm-thick shell to further stabilize the fluorescent nanoconjugate (Figure 1).<sup>28</sup> The as-prepared core-shell SiNPs exhibited narrow size distribution and good colloidal stability in aqueous solution for months. After the NP fabrication, we optimized the functionalization steps with two main goals: 1) the introduction of a specific marker for the recognition of the HER2 receptor in HER2<sup>+</sup> cancer; 2) the introduction of a radioisotope for SPECT imaging. The free silica surface was then exploited both to expose a targeting moiety and to host a proper chelating agent for radiolabeling. In particular, four types of silica nanoconjugates were synthesized and compared in order to evaluate the contribution of each functional moiety on the colloidal stability and on the fate of the resulting NPs (Table 1). Among the available radionuclides, we chose to introduce <sup>99m</sup>Tc as its 6 h half-life allowed us to follow the distribution of radiolabeled nanosilica in biodistricts. In addition, <sup>99m</sup>Tc nuclei emits only 140 keV characteristic  $\gamma$ -rays which, unlike  $\beta$ -rays that are usually emitted by other radionuclides, are absorbed far from the examined organ and minimize the danger posed to living matter. This property makes them highly desirable in nuclear medicine applications. In order to attach and retain the radionuclide, we decided to

exploit the nitrilotriacetic acid chelating linker. A silane derivative (IPTES-NTA complex) was synthesized and grafted on the silica surface together with APTMS residues, thus introducing the chelating and amine functionalities in a one pot reaction (Scheme 1, step 1). The NTA carboxylic moieties were then engaged in Ni<sup>2+</sup> chelation before the radiolabeling steps. To achieve an active targeting of nanoconjugates toward HER2<sup>+</sup> BC cells, Hc-TZ was considered an ideal ligand candidate, as it previously demonstrated to provide a prolonged accumulation of nanoconjugates in HER2<sup>+</sup> breast tumors, compared to other molecular targeting agents, such as entire TZ or the relevant scFv fragment.<sup>19</sup> Therefore, a heterobifunctional PEG containing a maleimido group was covalently linked to the amine residues of the SiNPs (Scheme 1, step 2). After the reduction of disulfide bonds bridging the two chains of the antibody, the resulting thiol groups of the Hc-TZ were reacted with the maleimides, leading to the immobilization of the antibody on the shell surface (Scheme 1, step 3). Unreacted functional groups were saturated with a methoxyl terminating PEG. As a result, the whole nanoconjugate consisted of a fluorescent core-shell structure modified with multiple functionalities, including a chelating group, a targeting moiety and a biocompatible PEG coating. As stated before, the impact of each functionalization step was assessed by comparing the four synthetic silica nanoconjugates (SiNP, SiNP-TZ, SiNP-NTA and SiNP-NTA-TZ) differing from each other by the lack of one or more units. All the SiNP conjugates were characterized in terms of hydrodynamic size and  $\zeta$ -potential (Table 1). SiNP and SiNP-TZ showed a hydrodynamic diameter (Hd) < 100 nm with good polydispersity indexes (PDI < 0.120). In contrast, the presence of the NTA linker, especially upon Ni<sup>2+</sup> ion chelation, led to a mild aggregation for SiNP-NTA and SiNP-NTA-TZ (Hd > 100 nm), which however was limited by the radiolabeling procedure. The characteristic negative  $\zeta$ -potential of the SiNPs was maintained for all kinds of nanoconjugates, which is an important prerequisite for low toxicity and systemic diffusion *in vivo*.<sup>29</sup>

### ***In vitro binding efficiency and selectivity of SiNPs by flow cytometry***

Binding selectivity of SiNPs toward HER2<sup>+</sup> BC cells was first evaluated by flow cytometry. To validate this system, SK-BR-3 cells were chosen as HER2<sup>+</sup> breast cancer model, whereas HER2-negative (HER2<sup>-</sup>) MDA-MB-468 cells were used as negative control. To investigate the impact of functionalization on the binding capacity of SiNPs, the study was performed comparing SiNP vs. SiNP-TZ and SiNP-NTA vs. SiNP-NTA-TZ (Figure 2). Each kind of nanoconjugate was separately incubated for different time periods (20 min, 1 h, 4 h, 24 h) in SK-BR-3 cells (Figure S3 in the Supporting Information) and MDA-MB-468 cells (Figure S4 in the Supporting Information). Flow cytometry evidenced a remarkable time-dependent increase of fluorescence signal after incubation of SiNP-TZ/SiNP-NTA-TZ with SK-BR-3 cells (Figure 2, B and D), and a significant difference ( $p < 0.05$ ) compared to MDA-MB-468 cells. This data demonstrated the capability of targeted NPs to selectively recognize HER2 receptors in SK-BR-3 cells. SiNP/SiNP-NTA exhibited a remarkably lower uptake in SK-BR-3 cells compared to Hc-TZ-modified SiNPs and no preferential affinity toward SK-BR-3 or MDA-MB-468 cell lines was recovered (Figure 2, A and C), suggesting that the interaction with cells was essentially attributable to nonspecific uptake in both HER2<sup>-</sup> or HER2<sup>+</sup> cells. However, nonspecific uptake was basically negligible within the first 4 h.



## ***In vitro fluorescence imaging***

To validate the flow cytometry data, the binding specificity of Hc-TZ-modified SiNPs for HER2<sup>+</sup> cells was assessed by fluorescence microscopy (Figure 3). Images of SiNPs (green) were overlaid on the corresponding nuclei image counterstained with Hoechst solution. SiNP, SiNP-TZ, SiNP-NTA and SiNP-NTA-TZ were incubated in parallel in SK-BR-3 and MDA-MB-468 cells for 20 min, 1 h, 4 h, 24 h. Fluorescence microscopy images showed that green fluorescence signal started to increase in HER2<sup>+</sup> cells after 1 h of incubation with SiNP-NTA-TZ. In these cells, fluorescence intensity increased over time and was considerably stronger than that shown in SiNP-NTA images. We didn't observe any differences in the behavior of SiNP-TZ and SiNP-NTA-TZ (Figure S5 in the Supporting Information). In addition, SiNP-NTA fluorescence intensity showed no significant difference in both cell lines, confirming the loss of selectivity for SiNPs in the absence of Hc-TZ conjugation. SK-BR-3 pictures acquired at 4 h and 24 h exhibited a perinuclear localization of green fluorescence signals exclusively after incubation with SiNP-NTA-TZ. In contrast, SiNP-NTA-TZ signal was not found in the cytoplasm of HER2<sup>-</sup> cells and remained localized outside the cells after 4 h and 24 h of incubation. At these time points, it was apparent that a large number of SiNP-NTA-TZ were internalized by HER2<sup>+</sup> SK-BR-3 cells, while they could be hardly taken up by HER2<sup>-</sup> MDA-MB-468 cells, confirming the specific targeting of Hc-TZ-functionalized SiNPs for HER2<sup>+</sup> tumor cells.

## ***NPs toxicity***

Cell toxicity of all SiNPs was assessed in HER2<sup>+</sup> SK-BR-3 and HER2<sup>-</sup> MDA-MB-468 BC cells. First, we evaluated the effects of SiNP, SiNP-TZ, SiNP-NTA and SiNP-NTA-TZ on mitochondrial metabolism through MTT assay performed at 1, 4, 24 and 48 h of incubation with a solution of SiNPs (100 µg/mL). The analysis revealed no significant modification of succinate dehydrogenase activity over time (MTT test)<sup>30</sup> in both cell lines (Figure 4, A) compared to untreated samples ( $p < 0.05$ ). Viability of SK-BR-3 and MDA-MB-468 cells exposed to the NPs was also investigated. Cell proliferation in both cells lines was not significantly affected after 1, 4, 24 and 48 h of exposure with all sets of NPs (Figure 4, B). In addition, MTT test was replicated at 4 and 24 h in non-transformed mammary epithelial MCF-10A cell line (HER2<sup>-</sup>) and confirmed the absence of cytotoxic effect caused by the NPs (see supplementary Figure S6). Taken together, these results indicated a good profile of safety for all nanoconstructs in cultures of both tumor and healthy mammary cells.

## ***SiNPs radiolabeling with <sup>99m</sup>Tc***

The tricarbonyl method developed by Waibel et al.<sup>31</sup> offers a convenient solution to label proteins with <sup>99m</sup>Tc radionuclide, enabling labeling without prior modification with bifunctional chelators. The [<sup>99m</sup>Tc(CO)<sub>3</sub>(OH<sub>2</sub>)<sub>3</sub>]<sup>+</sup> is an excellent precursor for <sup>99m</sup>Tc labeling of biomolecules, being stable and substitution-reactive.<sup>32</sup> This precursor is highly water-soluble and reveals good stability in aqueous solution over a broad pH range (pH 2-12) for several hours. The three coordinated water molecules are promptly substituted by a variety of functional groups, including amines, thioethers, thiols, and phosphines. The radiochemical purity of <sup>99m</sup>Tc(I) tricarbonyl ion solution could be easily checked by TLC and HPLC. The <sup>99m</sup>Tc(I) tricarbonyl ion was then introduced using a new approach, involving three steps: 1) prelabeling of

<sup>99m</sup>Tc–tricarbonyl core, II) reaction with poly-His peptide, III) conjugation to NTA groups of SiNP-NTA and SiNP-NTA-TZ.<sup>33</sup> With this approach, SiNPs were functionalized with 4 nmol NTA per mg of NPs, while the molar ratio between NTA and poly-His was 1:3. The reaction between tricarbonyl precursor and hexa-His-Tag peptide was almost quantitative (Figure S1 in the Supporting Information). The stability of [<sup>99m</sup>Tc(CO)<sub>3</sub>]<sup>+</sup>-His was checked after 24 h (Figure S2 in the Supporting Information).

### ***In vitro uptake of radiolabeled <sup>99m</sup>Tc-SiNPs***

To assess the selectivity of <sup>99m</sup>Tc-labeled NPs toward HER2<sup>+</sup> cells, we tested NTA-nanoconstructs with or without Hc-TZ in a kinetic binding assay on HER2<sup>+</sup> SK-BR-3 in comparison to HER2<sup>-</sup> MDA-MB-468 cells. <sup>99m</sup>Tc-labeled SiNP-NTA and SiNP-NTA-TZ were incubated in both cell lines at 1, 4 and 24 h. At these time points, media were removed and counted using a  $\gamma$ -counter and cells washed, removed and counted to calculate NPs uptake as % of total radioactivity administered. Specific binding curves were generated as shown in Figure 5. SiNP-NTA were bounded weakly and nonspecifically to both the MDA-MB-468 and the SK-BR-3 cells, giving a maximum value of 1.4% uptake 24 h after incubation (Figure 5A). In contrast, SiNP-NTA-TZ showed an uptake value of 1.6% in SK-BR-3 cells already after 1 h of incubation, reaching 2.3% at 4 h, compared to 1.1% of uptake observed in MDA-MB-468 cells ( $p < 0.05$ ). It is apparent that the specific uptake ratio [SK-BR-3/MDA-MB-468] for SiNP-NTA-TZ was maximum at this time point. The uptake of SiNP-NTA-TZ continued to increase up to 24 h showing a slight increase in both cell lines, following a similar nonspecific trend, and reaching an uptake value of 3.7% in HER2<sup>+</sup> cells and 2.1% in HER2<sup>-</sup> cells (Figure 5, B).

### ***Ex vivo biodistribution and fluorescence imaging of <sup>99m</sup>Tc-SiNPs in tumor***

Biodistribution pattern of <sup>99m</sup>Tc-labeled NPs (SiNP-NTA and SiNP-NTA-TZ) was assessed in a SK-BR-3 tumor mouse model at 4, 6 and 24 h. Results are summarized in Figure 6. At 4 h after injection of radiolabeled SiNP-NTA-TZ or SiNP-NTA, radioactivity accumulation in SK-BR-3 tumor was higher for TZ-conjugated NPs compared to nonconjugated NPs. At this time mean tumor uptake (expressed as %ID/g) was  $0.52 \pm 0.08$  for SiNP-NTA and  $0.67 \pm 0.03$  for SiNP-NTA-TZ, and tumor-to-muscle ratios of %ID/g were  $1.69 \pm 0.18$  and  $3.45 \pm 1.02$  for SiNP-NTA and SiNP-NTA-TZ, respectively. At longer times of exposure, we observed a reduction in tumor radioactivity concentration for animals injected with SiNP-NTA-TZ but not in those injected with SiNP-NTA. The decline of SiNP-NTA-TZ uptake value, observed from 6 h post-injection, could be explained by an active targeting followed by lysosomal degradation and consequent clearance of NP shell labeled with <sup>99m</sup>Tc. The higher radioactivity uptake observed in animals injected with SiNP-NTA suggests passive targeting promoted by tumor EPR effect. Considering the other organs, high levels of radioactivity were observed for both NPs in liver, kidney and spleen, even with different kinetics (supplementary data in Table S1). To better understand the *ex vivo* tumor uptake data obtained by radioactivity counting, the targeting specificity of <sup>99m</sup>Tc-labeled NPs (SiNP-NTA-TZ vs. SiNP-NTA) in SK-BR-3 lesions was assessed by post-mortem fluorescence microscopy. Immunofluorescence staining of tumor

cryosections collected at 4 h post-injection allowed us to establish the distribution of the two nanotracers (Figure 7). Images of SiNPs (green) and  $\beta$ -actin (red) were overlaid on the corresponding images reporting nuclei (blue). Fluorescence intensity in SiNP-NTA-TZ images was significantly higher than that from SiNP-NTA and it was mainly colocalized in the perinuclear area. In contrast, green fluorescence distribution in SiNP-NTA images was barely detectable on the surface of SK-BR-3 tumor cell membrane.

## Discussion

Human epidermal growth factor receptor 2 (HER2) is the product of a proto-oncogene and its overexpression was firstly observed in BC and is associated with malignant tumor phenotype, with poorer prognosis related to the degree of expression.<sup>34</sup> At present, the detection of HER2 in BC and in its metastases is based on invasive methods as biopsy, to obtain representative tissue for immunohistochemistry phenotyping.<sup>35</sup> Recently, new approaches were developed to determine soluble markers as HER2 extracellular domain and circulating miRNA for patients stratification, but these strategies have not been standardized yet.<sup>36,37</sup> To overcome the current limitation, a series of radiopharmaceuticals assembled with antibodies, nanobodies or affibodies have been developed and some of these are already under clinical evaluation for use as PET or SPECT nuclear imaging agents for *in vivo* molecular detection of HER2 receptor.<sup>38,39</sup> The present paper describes the use of a multifunctional NP system, able to act as a SPECT radiotracer for tumor detection and opening the opportunity to develop a new generation of theranostic nanoagents to be used for noninvasive detection of HER2<sup>+</sup> cells and targeted drug delivery.<sup>40,41</sup> In fact, although chemotherapy in combination with TZ administration has been reported to play an important role in the treatment of HER2<sup>+</sup> BC, about 70% of patients demonstrated resistance.<sup>42</sup> The use of non-targeted chemotherapeutic drugs significantly limits the drug accumulation within cancer cells and induces undesired toxic side effects toward normal tissues.<sup>43</sup> In this context, radiolabeled silica nanocarriers could represent a significant advance in the identification and treatment of HER2<sup>+</sup> BC lesions. To this aim, we designed and tested <sup>99m</sup>Tc-radiolabeled silica NPs for the selective detection of HER2 receptor in malignant BC cells, capitalizing on Hc-TZ functionalization. Our results suggest that receptor-mediated active targeting provided the best efficiency in BC detection, compared to simple EPR passive accumulation. We evaluated the behavior and the targeting efficiency of SiNPs functionalized or not with Hc-TZ, in BCs models in *in vitro* and *ex vivo* experiments, before and after radiolabeling. Well established protocols to radiolabel antibodies are reported in the literature.<sup>44</sup> However, we preferred to develop a new approach based on immobilization of radioligand to the NP surface obtaining a radiolabeled nanoscaffold common to the different nanoconstructs synthesized within this study, independent from the functionalization with the antibody chain. Radiolabeling of both SiNP-NTA and SiNP-NTA-TZ was achieved by formation of radioligand-NTA complex. *In vitro*, flow cytometry data showed a remarkable increase in uptake over time after incubation of SiNP-TZ/SiNP-NTA-TZ with HER2<sup>+</sup> SK-BR-3 cells, compared to SiNP/SiNP-NTA. As expected, the uptake of all silica NPs tested remained low in HER2<sup>-</sup> MDA-MB-468 cells. These results were confirmed by fluorescence microscopy, which exhibited a considerable perinuclear localization in SK-BR-3 cells exclusively upon incubation with SiNP-TZ/SiNP-NTA-TZ, while an external localization of fluorescence signal was observed in MDA-MB-468 cells with both SiNP-TZ/SiNP-NTA-TZ and SiNP/SiNP-NTA. *In vitro* toxicity assay of each SiNP set did not reveal significant impact on mitochondrial metabolism and cell viability in HER2<sup>+</sup>/HER<sup>-</sup> malignant cells and in

non-transformed mammary epithelial cells. The high efficiency and selectivity of Hc-TZ-modified SiNPs in the recognition of HER2<sup>+</sup> cells were also assessed after radiolabeling. The *in vitro* uptake of <sup>99m</sup>Tc-NPs in HER2<sup>+</sup>/HER<sup>-</sup> cells confirmed the results from flow cytometry, suggesting that our radiolabeling strategy did not affect the nanoconjugate binding capability. Next, the radiolabeled SiNPs efficiency in detecting HER2<sup>+</sup> cells was also evaluated in a SK-BR-3 xenograft animal model. *Ex vivo* biodistribution of <sup>99m</sup>Tc-SiNP-NTA-TZ showed a preferential intracellular distribution at 4 h post-injection compared to <sup>99m</sup>Tc-SiNP-NTA, confirming the involvement of Hc-TZ moiety in the targeting efficiency of the nanoconstruct compared to EPR passive accumulation. The drop of SiNP-NTA-TZ uptake value at late time points may represent a further potential confirmation of an active targeting mechanism, involving receptor-mediated endocytosis, which leads to lysosomal degradation of radiolabeled nanocomplex with time, as previously described with different colloidal NPs.<sup>45</sup> In a recent study by Chen *et al.*, mesoporous silica NPs were functionalized with the murine/human antibody TRC105 and used to target 4T1 BC lesion in mice.<sup>46</sup> Tumor uptake of TRC105-conjugated NPs reached the maximum signal intensity at 5 h post-injection and was twofold higher compared to muscle (background) and to non-conjugated NPs used as controls. Those data were comparable with the results of our *ex vivo* uptake studies, in which we assessed the targeting efficiency of radiolabeled antibody-functionalized SiNP-NTA-TZ and non-functionalized SiNP-NTA. In addition, <sup>99m</sup>Tc-SiNP-NTA-TZ cell selectivity observed at 4 h was confirmed by post-mortem fluorescence imaging of tumor cryosections, showing a specific intracellular localization compared to <sup>99m</sup>Tc-SiNP-NTA. This mechanism was already described in SK-BR-3 cells using different NPs functionalized with TZ.<sup>47,48</sup> A similar strategy of <sup>99m</sup>Tc-labeling was described by Yamaguchi *et al.* in 2016.<sup>40</sup> In this case, silica nanoparticles were targeted with double chain anti-HER2 antibody, and at four hours after injection, the authors observed higher levels of radioactivity uptake in SKBR3 tumor in comparison to HER2 negative one. However, despite the lower diameter of the nanoparticles used in their study, tumor uptake values were inferior to that observed using our method of radiolabeling and particles platform, functionalized with trastuzumab half-chain. The experimental data collected and the versatility of this NP-based system could be the basis for exploring new functionalization/radiolabeling strategies and for the possibility to load different dyes, for combined multimodal imaging. In addition, taking advantage of the easy and straightforward chemical functionalization of their surface with a plethora of functional ligands, several different kinds of therapeutics can be loaded to increase the efficiency and selectivity of nanoconjugates in order to improve patient stratification. In future studies, we will explore the possibility to directly introduce a radioisotope on the antibody chain (Hc-TZ) of SiNP-TZ NPs, in order to follow the fate of the nanoconjugate components separately.

## Conclusion

In summary, we have reported here a SiNP-based system for non-invasive detection, staging and potential treatment of HER2<sup>+</sup> BC. Our radiolabeled system not only exhibited an enhanced targeting for the tumor, compared to EPR passive diffusion, but also significantly increased the selective accumulation of SiNPs within the HER2<sup>+</sup> SK-BR-3 cells, taking advantage of an optimized conjugation to the half-chain fragment of the humanized antibody trastuzumab, already in use in the clinical practice. Our results are encouraging, suggesting further assessment of silica-radionuclide nanoconjugates with the aim to develop a new

generation of versatile nanoreporters for enhanced-resolution nuclear medicine and to promote this system as a theranostic agent of highly aggressive HER2<sup>+</sup> BC detection and treatment.

## Acknowledgments

We thank R. Allevi (CMENA, University of Milan) for TEM images. This work was supported by a grant from the MIUR, NanoBreastImaging “Progetto Bandiera NanoMAX” (to RMM). MC and DP received support by the Fondazione Regionale per la Ricerca Biomedica (FRRB).

## Author contributions

‡ These authors contributed equally. RMM and DP, joint senior authors.

The manuscript was written through contributions of all authors. All authors have given approval to the final version of the manuscript.

## Disclosure

The authors report no conflicts of interest in this work.

## References

1. Siegel RL, Miller KD, Jemal A. Cancer statistics, 2015. *CA Cancer J Clin.* 2015;65(1):5-29.
2. Slamon DJ, Clark GM, Wong SG, Levin WJ, Ullrich A, McGuire WL. Human breast cancer: correlation of relapse and survival with amplification of the HER-2/neu oncogene. *Science.* 1987;235(4785):177-182.
3. Chang HR. Trastuzumab-based neoadjuvant therapy in patients with HER2-positive breast cancer. *Cancer.* 2010;116(12):2856-2867.
4. Slamon DJ, Leyland-Jones B, Shak S, et al. Use of chemotherapy plus a monoclonal antibody against HER2 for metastatic breast cancer that overexpresses HER2. *New Engl J Med.* 2001;344(11):783-792.
5. Di Leo A, Dowsett M, Horten B, Penault-Llorca F. Current status of HER2 testing. *Oncology.* 2002;63 Suppl 1:25-32.
6. Gaijkel LO, Huang L, Caveliers V, et al. Comparison of the biodistribution and tumor targeting of two <sup>99m</sup>Tc-labeled anti-EGFR nanobodies in mice, using pinhole SPECT/micro-CT. *J Nucl Med.* 2008;49(5):788-795.
7. Gambhir SS. Molecular imaging of cancer with positron emission tomography. *Nat Rev Cancer.* 2002;2(9):683-693.

8. Ahlgren S, Wallberg H, Tran TA, et al. Targeting of HER2-expressing tumors with a site-specifically <sup>99m</sup>Tc-labeled recombinant affibody molecule, ZHER2:2395, with C-terminally engineered cysteine. *Journal of nuclear medicine : official publication, Society of Nuclear Medicine*. 2009;50(5):781-789.
9. Meszaros LK, Dose A, Biagini SCG, Blower PJ. Hydrazinonicotinic acid (HYNIC) - Coordination chemistry and applications in radiopharmaceutical chemistry. *Inorg Chim Acta*. 2010;363(6):1059-1069.
10. Lipowska M, Marzilli LG, Taylor AT. Tc-<sup>99m</sup>(CO)(3)-Nitrilotriacetic Acid: A New Renal Radiopharmaceutical Showing Pharmacokinetic Properties in Rats Comparable to Those of I-131-OIH. *Journal of Nuclear Medicine*. 2009;50(3):454-460.
11. Egli A, Alberto R, Tannahill L, et al. Organometallic <sup>99m</sup>Tc-aquaion labels peptide to an unprecedented high specific activity. *Journal of nuclear medicine : official publication, Society of Nuclear Medicine*. 1999;40(11):1913-1917.
12. Yezhelyev MV, Gao X, Xing Y, Al-Hajj A, Nie SM, O'Regan RM. Emerging use of nanoparticles in diagnosis and treatment of breast cancer. *Lancet Oncology*. 2006;7(8):657-667.
13. Orza A, Casciano D, Biris A. Nanomaterials for targeted drug delivery to cancer stem cells. *Drug Metab Rev*. 2014;46(2):191-206.
14. Bourzac K. Nanotechnology Carrying Drugs. *Nature*. 2012;491(7425):S58-S60.
15. Choi HS, Frangioni JV. Nanoparticles for Biomedical Imaging: Fundamentals of Clinical Translation. *Mol Imaging*. 2010;9(6):291-310.
16. Maeda H, Wu J, Sawa T, Matsumura Y, Hori K. Tumor vascular permeability and the EPR effect in macromolecular therapeutics: a review. *Journal of Controlled Release*. 2000;65(1-2):271-284.
17. Bertrand N, Wu J, Xu XY, Kamaly N, Farokhzad OC. Cancer nanotechnology: The impact of passive and active targeting in the era of modern cancer biology. *Adv Drug Deliver Rev*. 2014;66:2-25.
18. Baselga J, Swain SM. Novel anticancer targets: revisiting ERBB2 and discovering ERBB3. *Nature Reviews Cancer*. 2009;9(7):463-475.
19. Fiandra L, Mazzucchelli S, De Palma C, et al. Assessing the In Vivo Targeting Efficiency of Multifunctional Nanoconstructs Bearing Antibody-Derived Ligands. *ACS nano*. 2013;7(7):6092-6102.
20. Chow EKH, Ho D. Cancer Nanomedicine: From Drug Delivery to Imaging. *Science Translational Medicine*. 2013;5(216).

21. Vivero-Escoto JL, Huxford-Phillips RC, Lin WB. Silica-based nanoprobe for biomedical imaging and theranostic applications. *Chem Soc Rev.* 2012;41(7):2673-2685.
22. Benezra M, Penate-Medina O, Zanzonico PB, et al. Multimodal silica nanoparticles are effective cancer-targeted probes in a model of human melanoma. *J Clin Invest.* 2011;121(7):2768-2780.
23. Kempen PJ, Greasley S, Parker KA, et al. Theranostic Mesoporous Silica Nanoparticles Biodegrade after Pro-Survival Drug Delivery and Ultrasound/Magnetic Resonance Imaging of Stem Cells. *Theranostics.* 2015;5(6):631-642.
24. Veerananarayanan S, Poulouse AC, Mohamed MS, et al. Synergistic targeting of cancer and associated angiogenesis using triple-targeted dual-drug silica nanoformulations for theragnostics. *Small.* 2012;8(22):3476-3489.
25. Mahon E, Hristov DR, Dawson KA. Stabilising fluorescent silica nanoparticles against dissolution effects for biological studies. *Chem Commun (Camb).* 2012;48(64):7970-7972.
26. Soto-Cantu E, Cueto R, Koch J, Russo PS. Synthesis and Rapid Characterization of Amine-Functionalized Silica. *Langmuir.* 2012;28(13):5562-5569.
27. Bae SW, Tan WH, Hong JI. Fluorescent dye-doped silica nanoparticles: new tools for bioapplications. *Chem Commun (Camb).* 2012;48(17):2270-2282.
28. Yokoi T, Sakamoto Y, Terasaki O, Kubota Y, Okubo T, Tatsumi T. Periodic arrangement of silica nanospheres assisted by amino acids. *J Am Chem Soc.* 2006;128(42):13664-13665.
29. Blanco E, Shen H, Ferrari M. Principles of nanoparticle design for overcoming biological barriers to drug delivery. *Nat Biotechnol.* 2015;33(9):941-951.
30. Almutary A, Sanderson BJS. The MTT and Crystal Violet Assays: Potential Confounders in Nanoparticle Toxicity Testing. *Int J Toxicol.* 2016;35(4):454-462.
31. Waibel R, Alberto R, Willuda J, et al. Stable one-step technetium-99m labeling of His-tagged recombinant proteins with a novel Tc(I)-carbonyl complex. *Nat Biotechnol.* 1999;17(9):897-901.
32. Alberto R, Schibli R, Egli A, Schubiger AP, Abram U, Kaden TA. A novel organometallic aqua complex of technetium for the labeling of biomolecules: Synthesis of [Tc-99m(OH<sub>2</sub>)(3)(CO)(3)](+) from [(TcO<sub>4</sub>)-Tc-99m](-) in aqueous solution and its reaction with a bifunctional ligand. *J Am Chem Soc.* 1998;120(31):7987-7988.
33. Badar A, Williams J, de Rosales RTM, et al. Optimising the radiolabelling properties of technetium tricarbonyl and His-tagged proteins. *Ejnmri Res.* 2014;4.

34. Allred DC, Clark GM, Molina R, et al. Overexpression of HER-2/neu and its relationship with other prognostic factors change during the progression of in situ to invasive breast cancer. *Hum Pathol.* 1992;23(9):974-979.
35. Gutierrez C, Schiff R. HER2: biology, detection, and clinical implications. *Arch Pathol Lab Med.* 2011;135(1):55-62.
36. Leyland-Jones B, Smith BR. Serum HER2 testing in patients with HER2-positive breast cancer: the death knell tolls. *Lancet Oncol.* 2011;12(3):286-295.
37. Graveel CR, Calderone HM, Westerhuis JJ, Winn ME, Sempere LF. Critical analysis of the potential for microRNA biomarkers in breast cancer management. *Breast cancer.* 2015;7:59-79.
38. Vaidyanathan G, McDougald D, Choi J, et al. Preclinical Evaluation of 18F-Labeled Anti-HER2 Nanobody Conjugates for Imaging HER2 Receptor Expression by Immuno-PET. *Journal of nuclear medicine : official publication, Society of Nuclear Medicine.* 2016;57(6):967-973.
39. Xavier C, Blykers A, Vaneycken I, et al. (18)F-nanobody for PET imaging of HER2 overexpressing tumors. *Nucl Med Biol.* 2016;43(4):247-252.
40. Yamaguchi H, Tsuchimochi M, Hayama K, Kawase T, Tsubokawa N. Dual-Labeled Near-Infrared/(99m)Tc Imaging Probes Using PAMAM-Coated Silica Nanoparticles for the Imaging of HER2-Expressing Cancer Cells. *Int J Mol Sci.* 2016;17(7).
41. Geng J, Liu J, Liang J, Shi H, Liu B. A general approach to prepare conjugated polymer dot embedded silica nanoparticles with a SiO<sub>2</sub>@CP@SiO<sub>2</sub> structure for targeted HER2-positive cellular imaging. *Nanoscale.* 2013;5(18):8593-8601.
42. Romond EH, Perez EA, Bryant J, et al. Trastuzumab plus adjuvant chemotherapy for operable HER2-positive breast cancer. *New Engl J Med.* 2005;353(16):1673-1684.
43. Ma B, Ma QQ, Wang HQ, Zhang GL, Zhang HY, Wang XH. Clinical efficacy and safety of T-DM1 for patients with HER2-positive breast cancer. *Oncotargets Ther.* 2016;9:959-976.
44. Li C, Zhang Y, Wang L, et al. A novel multivalent (99m)Tc-labeled EG2-C4bpalpha antibody for targeting the epidermal growth factor receptor in tumor xenografts. *Nucl Med Biol.* 2015;42(6):547-554.
45. Corsi F, Fiandra L, De Palma C, et al. HER2 Expression in Breast Cancer Cells Is Downregulated Upon Active Targeting by Antibody-Engineered Multifunctional Nanoparticles in Mice. *ACS nano.* 2011;5(8):6383-6393.
46. Chen F, Nayak TR, Goel S, et al. In Vivo Tumor Vasculature Targeted PET/NIRF Imaging with TRC105(Fab)-Conjugated, Dual-Labeled Mesoporous Silica Nanoparticles. *Mol Pharmaceut.* 2014;11(11):4007-4014.



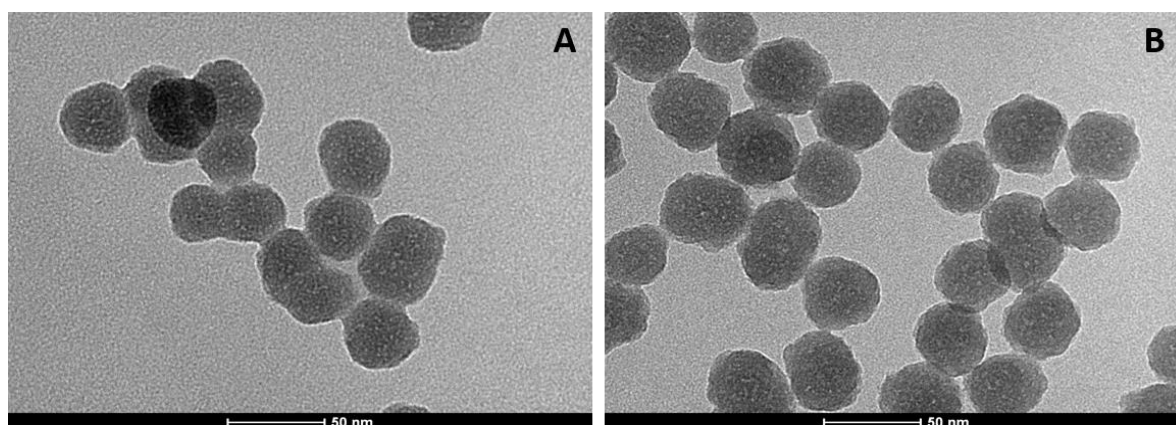
47. Sun B, Ranganathan B, Feng SS. Multifunctional poly(D,L-lactide-co-glycolide)/montmorillonite (PLGA/MMT) nanoparticles decorated by Trastuzumab for targeted chemotherapy of breast cancer. *Biomaterials*. 2008;29(4):475-486.
48. Milgroom A, Intrator M, Madhavan K, et al. Mesoporous silica nanoparticles as a breast-cancer targeting ultrasound contrast agent. *Colloid Surface B*. 2014;116:652-657.

## Figures

**Table 1.** Properties of nanoconjugates evaluated in this study. Data are the mean  $\pm$  standard deviation of three different NP batches

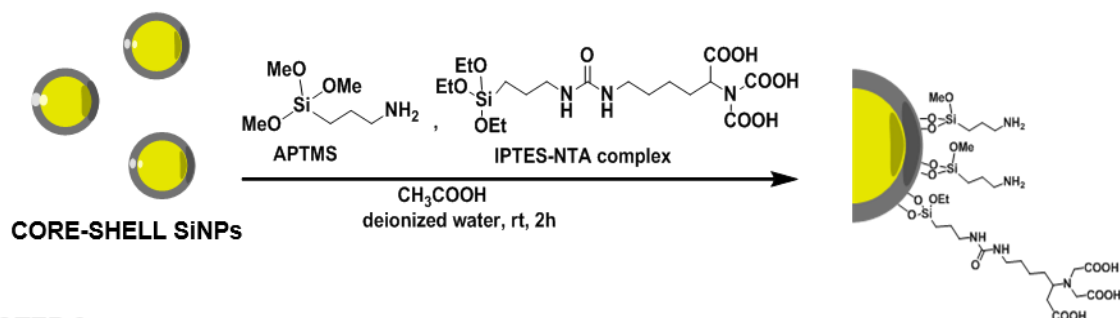
Nanoconjugate	Functionalization	Hydrodynamic size (nm)	PDI	$\zeta$ -potential (mV)
SiNP	Only PEG	85.59 $\pm$ 9.49	0.119 $\pm$ 0.091	- 30.2 $\pm$ 0.30
SiNP-TZ	PEG + TZ	93.61 $\pm$ 6.22	0.095 $\pm$ 0.027	- 31.6 $\pm$ 0.30
SiNP-NTA	PEG + NTA	123.9 $\pm$ 29.77	0.114 $\pm$ 0.024	- 33.5 $\pm$ 6.55
SiNP-NTA-TZ	PEG + NTA + TZ	114.3 $\pm$ 0.70	0.084 $\pm$ 0.001	- 33.6 $\pm$ 6.00

**Abbreviations:** PDI, polydispersity index

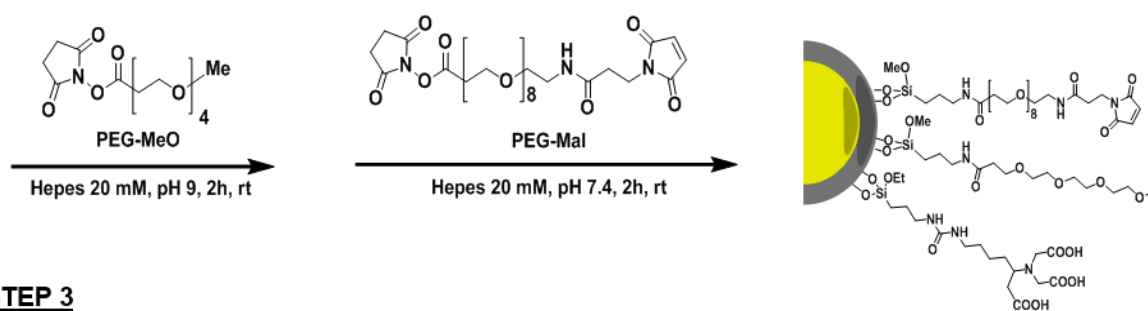


**Figure 1.** TEM images showing silica NPs before (A) and after (B) the shell synthesis.

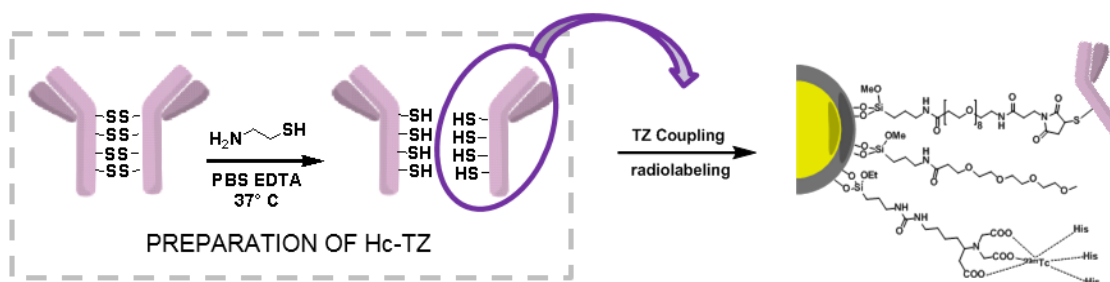
### STEP 1



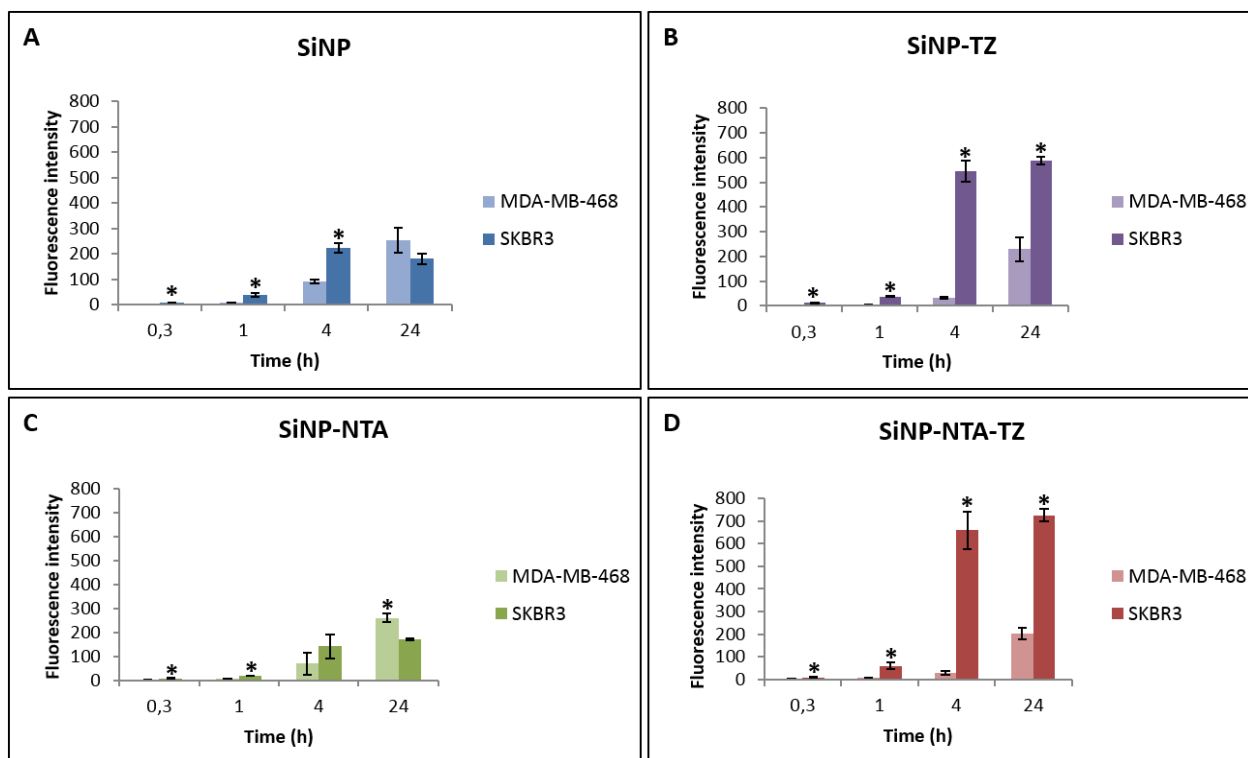
### STEP 2



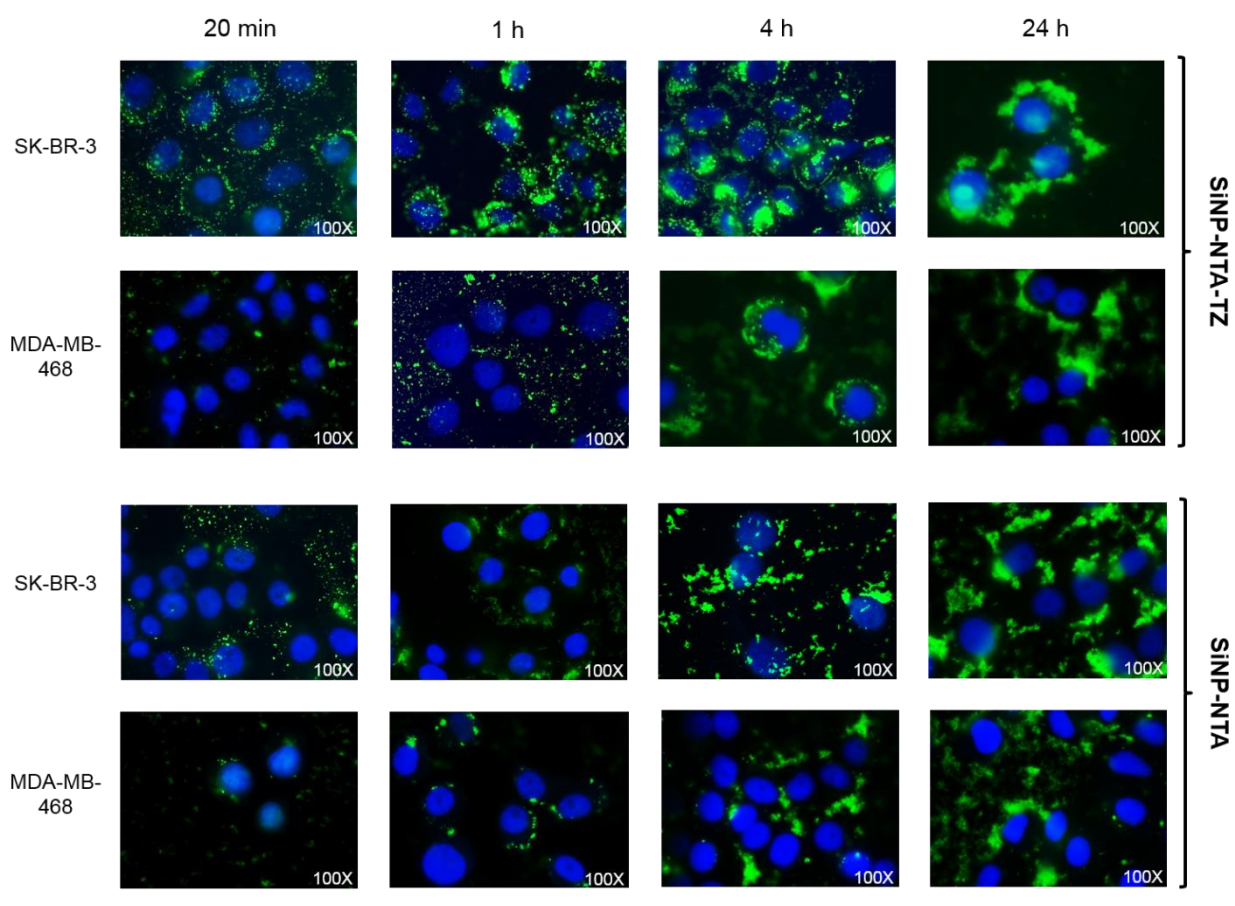
### STEP 3



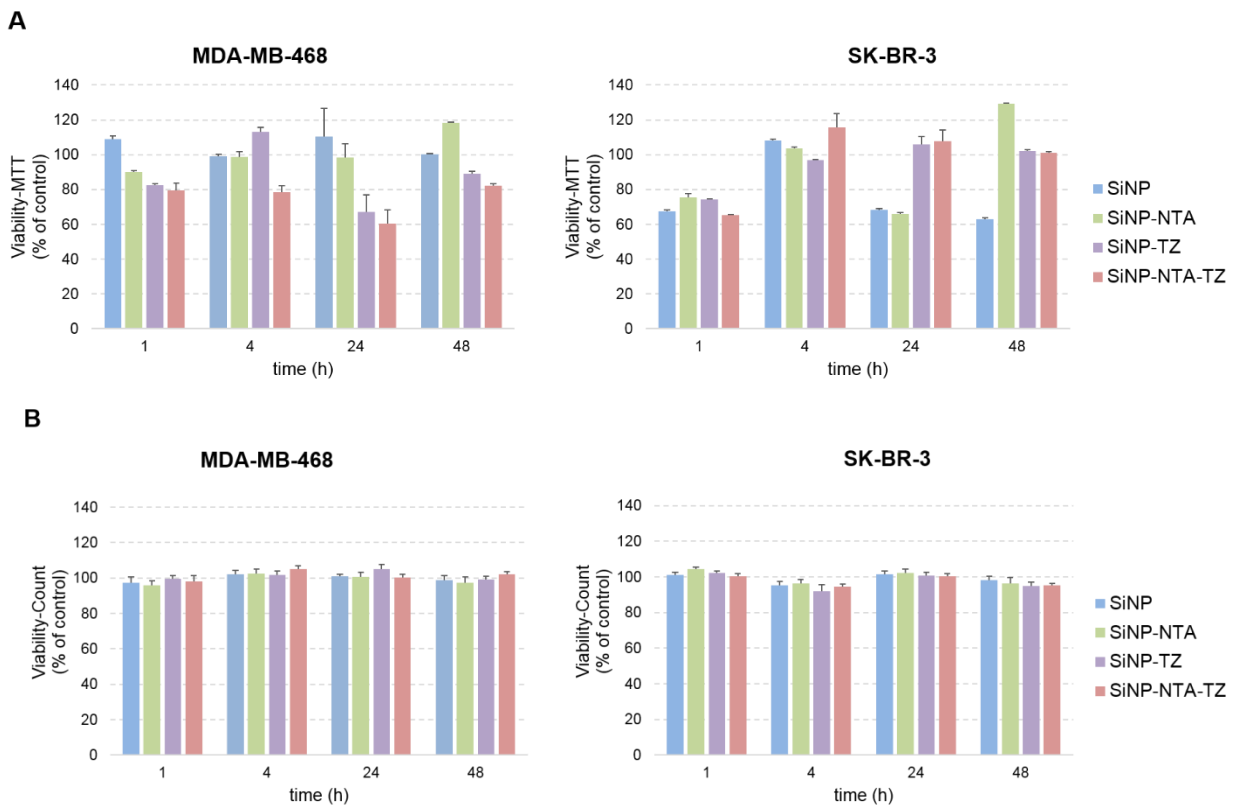
**Scheme 1.** Schematic representation of the synthetic steps for the preparation of SiNP-NTA-TZ.



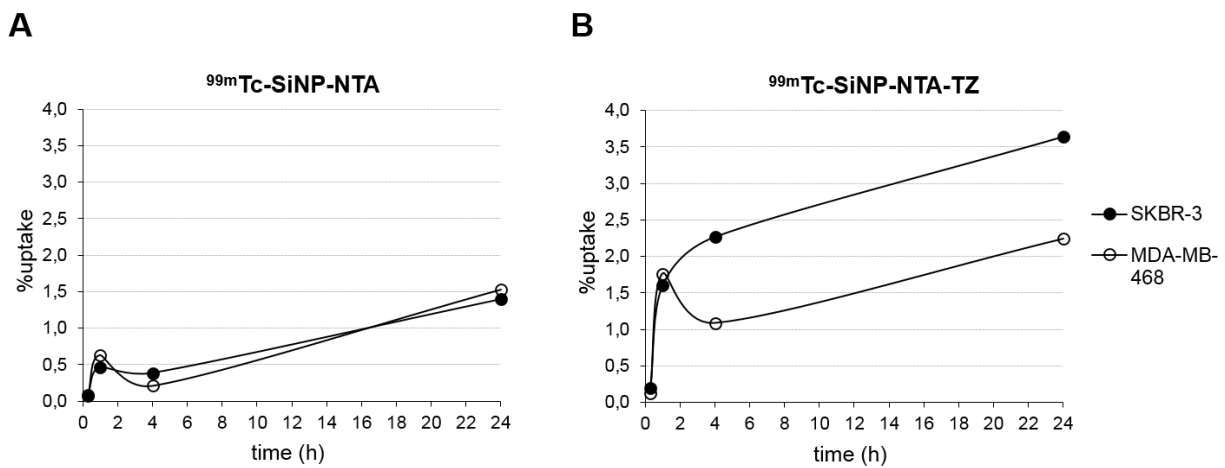
**Figure 2.** Assessment of binding efficiency by flow cytometry. Panels A-D represent the distribution of cell fluorescence intensity, normalized over untreated cells (control), in MDA-MB-468 and SK-BR-3 cell lines after exposure to A) SiNP, B) SiNP-TZ, C) SiNP-NTA and D) SiNP-NTA-TZ at 20 min, 1 h, 4 h and 24 h at a concentration of 50 mg/mL (Student's *t*-test; \**p* < 0.05 vs. MDA-MB-468).



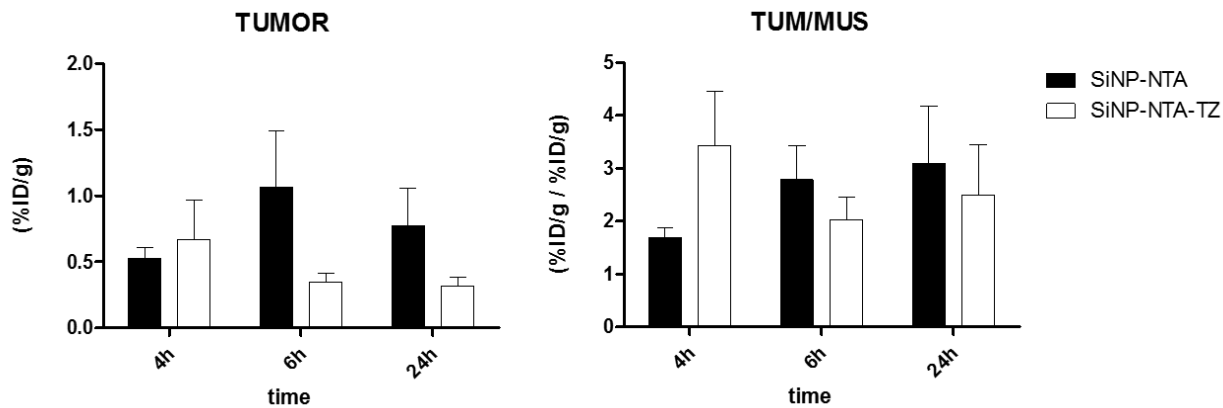
**Figure 3.** Specificity binding by fluorescence microscopy. SK-BR-3 and MDA-MB-468 cells were grown on coverslips for 24 h and then exposed for 1, 4, 24, 48 h to 50  $\mu\text{g/ml}$  of FITC-labeled (green) SiNPs functionalized with (SiNP-NTA-TZ) or without (SiNP-NTA) Hc-TZ. Nuclei were stained with Hoechst (blue). Scale bar: 50  $\mu\text{m}$ .



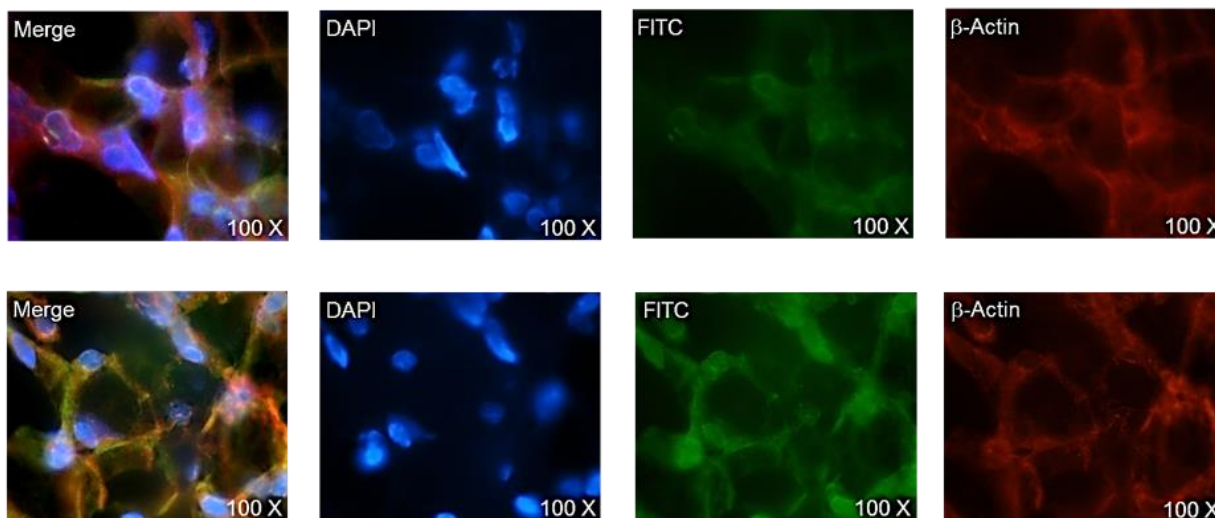
**Figure 4.** SiNPs toxicity was investigated both by A) MTT and B) cell viability tests. SK-BR-3, MDA-MB-468 cells were incubated with SiNPs (100  $\mu\text{g}/\text{mL}$ ) for 1, 4, 24 and 48 h.



**Figure 5.** *In vitro* uptake of  $^{99\text{m}}\text{Tc}$ -radiolabeled A) SiNP-NTA and B) SiNP-NTA-TZ NPs. SK-BR-3 and MDA-MB-468 cells were incubated with SiNPs (1  $\mu\text{Ci}/\text{mL}$ ) for 1, 4, 24 h. Cell uptake was expressed as % of total radioactivity administered. (Student's *t*-test; \**p* < 0.05 vs. MDA-MB-468).



**Figure 6.** *Ex vivo* biodistribution of <sup>99m</sup>Tc-labeled SiNP-NTA and SiNP-NTA-TZ nanoparticles. SK-BR-3 tumor bearing mice were sacrificed at 4, 6h (n = 3) and 24 h (n = 4) post-injection. Samples were dissected and analyzed by  $\gamma$ -counter to obtain tumor-to-muscle ratio of %ID/g (on the right) and the tumor absolute values (on the left).



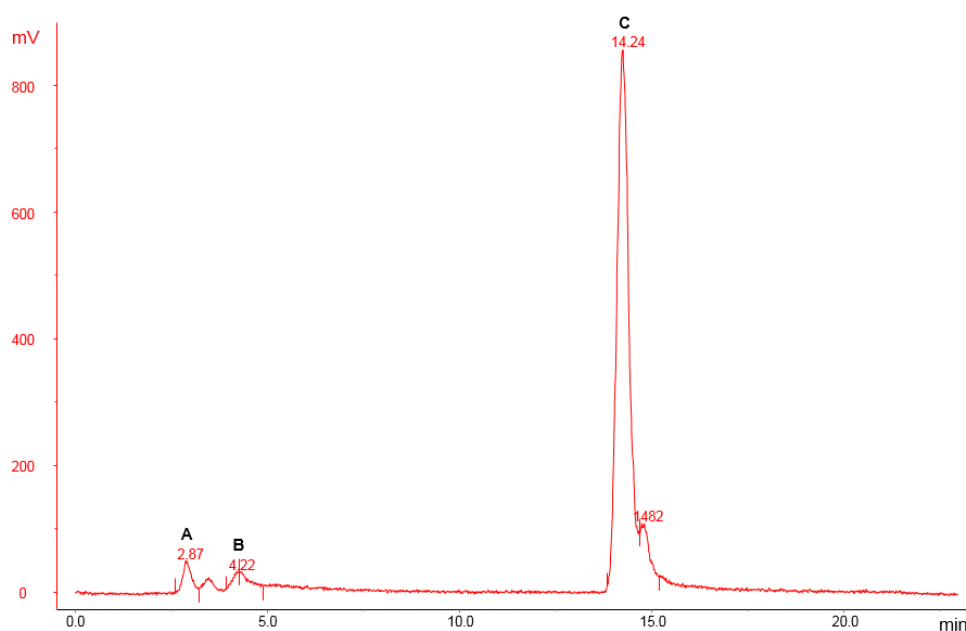
**Figure 7.** *Ex vivo* immunofluorescence of SK-BR-3 tumor cryosections collected at 4 h post-injection of SiNP-NTA (top) and SiNP-NTA-TZ (bottom). Merge images represent the colocalization of SiNPs (green),  $\beta$ -actin (red) and reporting nuclei (blue). Scale bar: 50  $\mu$ m.

# Supporting Information

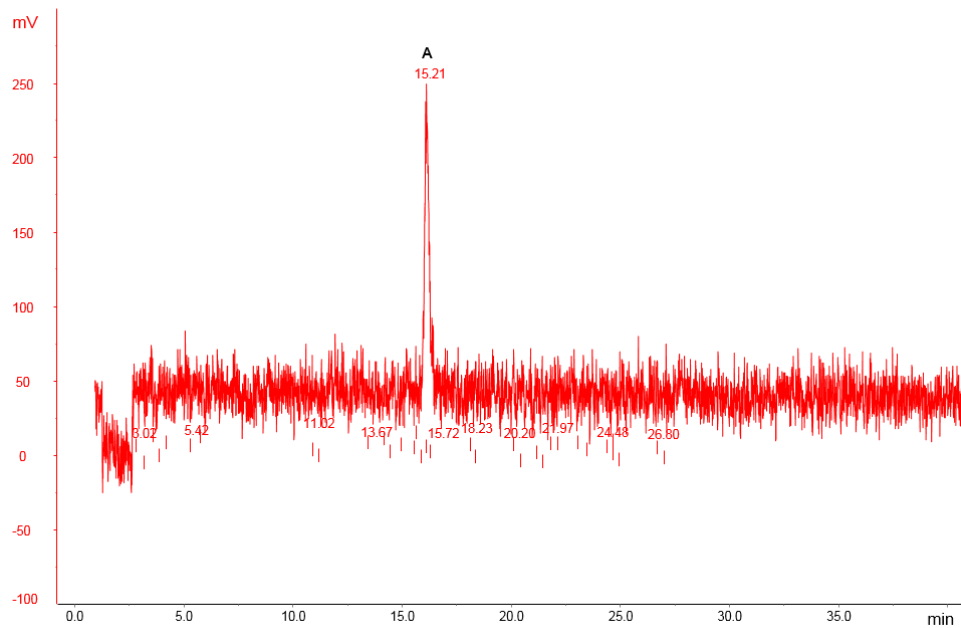
## Development of $^{99m}\text{Tc}$ -Radiolabeled Nanosilica for Targeted Detection of HER2-Positive Breast Cancer

*Paolo Rainone,1,‡ Benedetta Riva,2,‡ Sara Belloli,1,\* Francesco Sudati,3 Marilena Ripamonti,1 Paolo Verderio,2 Miriam Colombo,2 Maria Carla Gilardi,1 Rosa Maria Moresco,4 Davide Prospero,2,\**

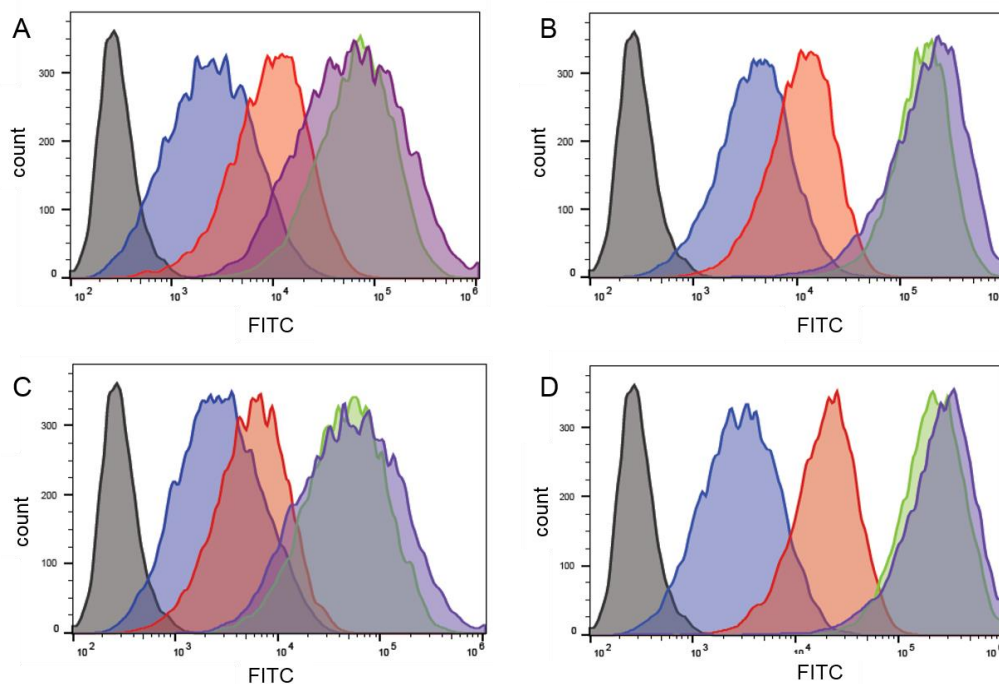
1 Institute of Molecular Bioimaging and Physiology of CNR, Via Fratelli Cervi 93, 20090 Segrate, Italy. 2 NanoBioLab, Dipartimento di Biotecnologie e Bioscienze, Università di Milano-Bicocca, Piazza della Scienza 2, 20126 Milano, Italy. 3 PET and Nuclear Medicine Unit, San Raffaele Scientific Institute, Via Olgettina 60, 20132 Milan, Italy. 4 Department of Medicine and Surgery, University of Milano-Bicocca, Via Cadore 48, 20900 Monza, Italy.



**Figure S1.** Radiochemical yield of  $^{99m}\text{Tc}$ -Tricarboxyl core labeling His-Tag, after 50 min incubation: Pertechnetate [ $^{99m}\text{TcO}_4$ ] $^-$  (A);  $^{99m}\text{Tc}$ -Tricarboxyl core [ $^{99m}\text{Tc}(\text{CO})_3$ ] $^+$  (B);  $^{99m}\text{Tc}$ -Tricarboxyl-His-Tag complex (C).

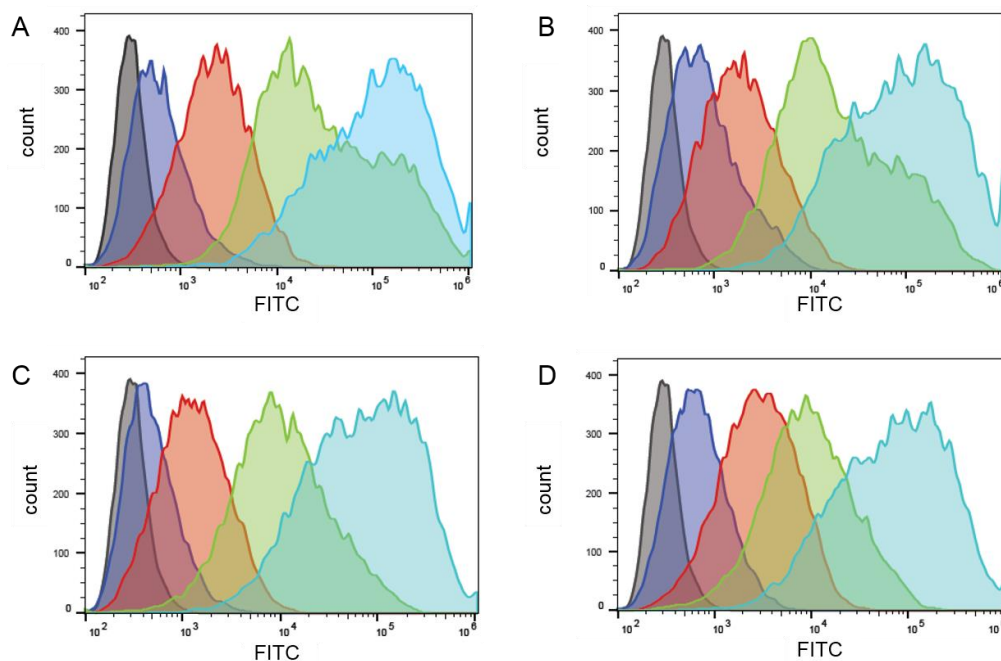


**Figure S2.** Stability of  $^{99m}\text{Tc}$ -Tricarboxyl-His-Tag complex after 24 h EOS, in aqueous solutions over a broad pH range (pH 2-12):  $^{99m}\text{Tc}$ -Tricarboxyl-His-Tag complex (A).

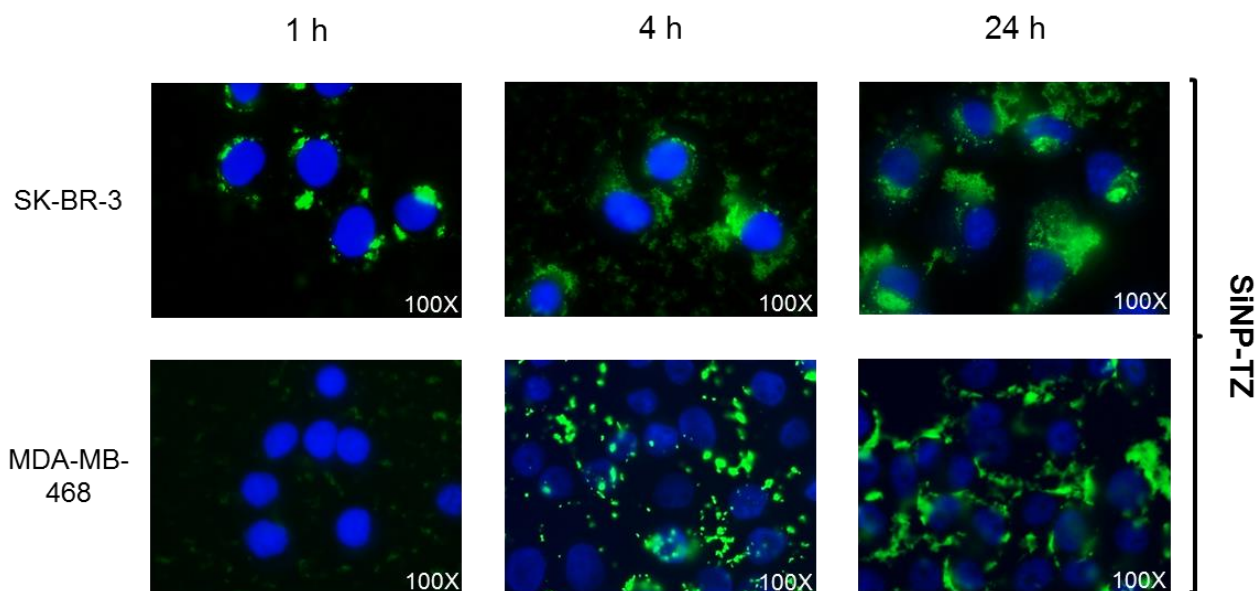


**Figure S3.** Assessment of binding specificity by flow cytometry. HER2+ SK-BR-3 cells were incubated with 50 mg/mL of A) SiNP, B) SiNP-TZ, C) SiNP-NTA and D) SiNP-NTA-TZ for 20 min (blue), 1h (red), 4h (green) and 24 h (violet). Untreated cells were used as negative control (grey) to set the autofluorescence of the cells.

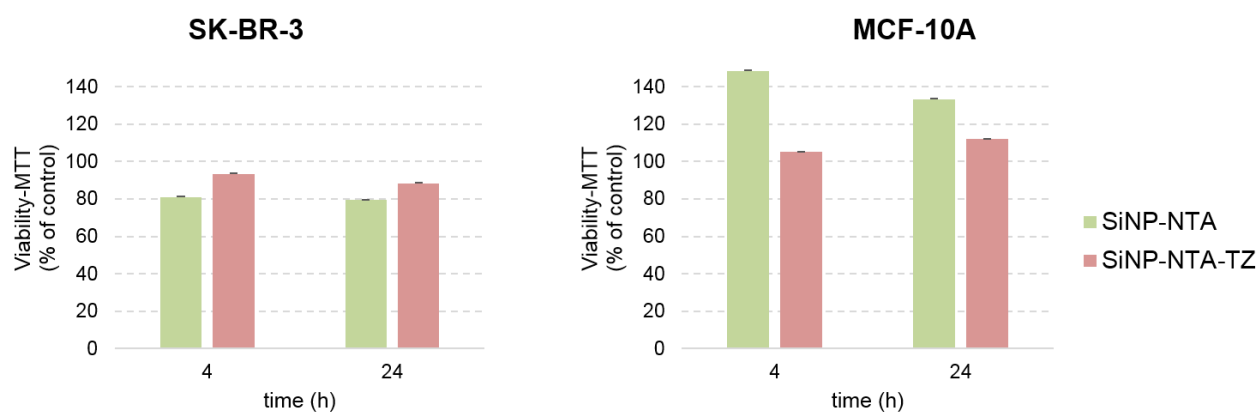




**Figure S4.** Assessment of binding specificity by flow cytometry. HER2- MDA-MB-468 cells were incubated with 50 mg/mL of A) SiNP, B) SiNP-TZ, C) SiNP-NTA and D) SiNP-NTA-TZ for 20 min (dark blue), 1 h (red), 4 h (green) and 24 h (light blue). Untreated cells were used as negative control (grey) to set the autofluorescence of cells.



**Figure S5.** Specificity binding by fluorescence microscopy. SK-BR-3 and MDA-MB-468 cells were grown on coverslips for 24 h and then exposed for 1, 4 and 24 h to 50  $\mu$ g/ml of FITC-labeled (green) SiNPs, functionalized with Hc-TZ. Nanoparticles were engineered without nitrilotriacetic acid chelating linker for evaluate its contribution on targeting capability. Nuclei were stained with DAPI (blue).



**Figure S6.** MTT test was replicated at 4 and 24 h in non-transformed mammary epithelial MCF-10A cell line, (HER2-) in comparison to SK-BR-3 breast cancer cell line (HER2+), incubated with SiNP-NTA and/or SiNP-NTA-TZ.

Tissue	At 4 h (n=3)		At 6 h (n=3)		At 24 h (n=4)	
	SiNP-NTA	SiNP-NTA-TZ	SiNP-NTA	SiNP-NTA-TZ	SiNP-NTA	SiNP-NTA-TZ
(%ID/g)						
Blood	0.84 ± 0.14	1.27 ± 0.24	0.88 ± 0.21	1.05 ± 0.15	0.43 ± 0.06	0.52 ± 0.11
Heart	0.32 ± 0.07	0.44 ± 0.01	0.46 ± 0.13	0.33 ± 0.13	0.22 ± 0.02	0.99 ± 1.53
Lung	0.89 ± 0.13	2.31 ± 0.79	1.09 ± 0.12	1.38 ± 0.64	0.47 ± 0.07	0.35 ± 1.28
Liver	58.6 ± 10.9	36.3 ± 7.13*	44.6 ± 34.9	13.2 ± 11.7	7.83 ± 2.08	9.14 ± 5.34
Spleen	6.48 ± 0.49	6.96 ± 1.00	4.98 ± 4.68	2.62 ± 3.68	0.82 ± 0.20	2.42 ± 1.89
Stomach	0.44 ± 0.17	0.46 ± 0.28	0.52 ± 0.21	0.42 ± 0.16	0.33 ± 0.05	0.25 ± 0.12
Kidney	13.3 ± 1.55	5.52 ± 0.04*	51.6 ± 59.8	6.83 ± 1.36	14.3 ± 2.02	5.19 ± 1.57*
Intestine	0.72 ± 0.18	1.44 ± 0.88	1.99 ± 1.22	0.43 ± 0.17	0.35 ± 0.07	0.26 ± 0.06
Tumor	0.52 ± 0.08	0.67 ± 0.30	1.06 ± 0.43	0.35 ± 0.07	0.77 ± 0.28	0.32 ± 0.07
Tiroyd	0.53 ± 0.11	0.67 ± 0.19	0.54 ± 0.12	0.44 ± 0.08	0.40 ± 0.09	0.35 ± 0.11
Muscle	0.31 ± 0.02	0.19 ± 0.03*	0.38 ± 0.29	0.18 ± 0.05	0.26 ± 0.08	0.13 ± 0.03

**Table S1.** Radioactivity distribution after <sup>99m</sup>Tc-labeled SiNP-NTA or SiNP-NTA-TZ injection. Radioactivity concentration is expressed as percentage of injected dose per gram of tissue (%ID/g). Values are expressed as mean ±S.D. of three rats for each time point. (\*p<0.05 vs. SiNP-NTA)